Cell

Article

# Multiscale integration of tissue and chromatin context converts cell heterogeneity into stable intestinal patterning

## Graphical abstract

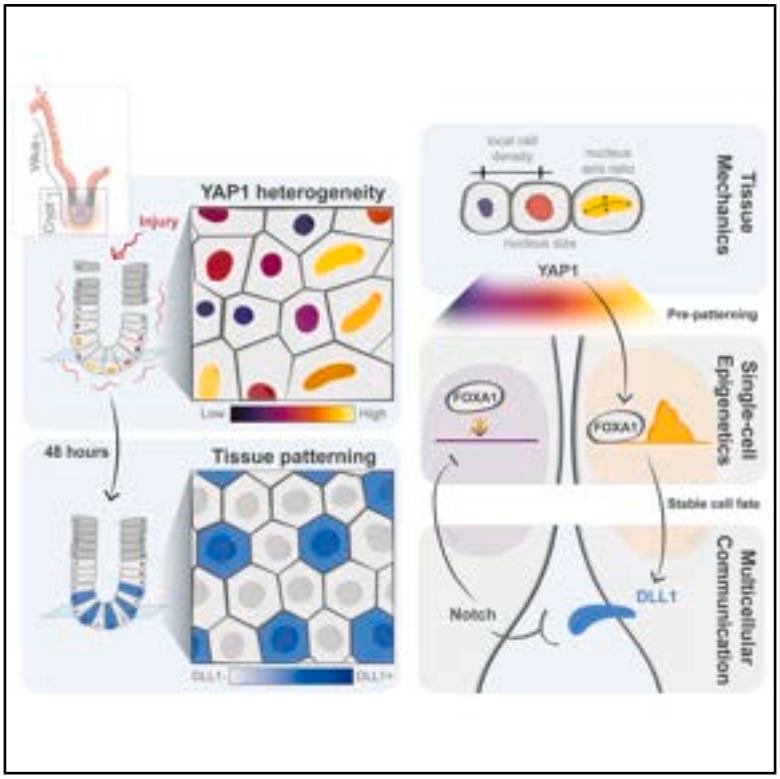


## Highlights

- Tissue density defines a window of YAP1 heterogeneity for regenerative patterning
- YAP1 heterogeneity encodes lineage-biased competence at the chromatin level
- FOXA1 integrates the YAP1 state with Delta-Notch signaling to drive fate bistability
- Fate bistability converts transient heterogeneity into stable regenerative patterning

## Authors

Cornelia Schwayer, Silvia Barbiero, David B. Brückner, ..., Michael B. Stadler, Edouard Hannezo, Prisca Liberali

## Correspondence

edouard.hannezo@ist.ac.at (E.H.), prisca.liberali@fmi.ch (P.L.)

## In brief

During regeneration, tissues must translate transient cellular variability into stable spatial organization. Tissue architecture generates a density-dependent window of heterogeneity in the mechanosensor YAP1 that FOXA1 integrates with Delta-Notch signaling, thereby linking tissue-scale mechanics to bistable cell fate decisions and stable tissue patterning.

Schwayer et al., 2026, Cell *189*, 1–17
August 20, 2026 © 2026 The Authors. Published by Elsevier Inc.
https://doi.org/10.1016/j.cell.2026.06.009

CellPress

Please cite this article in press as: Schwayer et al., Multiscale integration of tissue and chromatin context converts cell heterogeneity into stable intestinal patterning, Cell (2026), https://doi.org/10.1016/j.cell.2026.06.009

Cell

CellPress
OPEN ACCESS

Article

# Multiscale integration of tissue and chromatin context converts cell heterogeneity into stable intestinal patterning

Cornelia Schwayer,[1,2,14] Silvia Barbiero,[1,2,3,14] David B. Brückner,[4,5,6,14] Koen C. Oost,[1] Clara Baader,[1,3] Nicole A. Repina,[1] Jinse Kim,[7] Oscar E. Diaz,[8] Isa Uccelli,[1] Laura Capolupo,[2] Ludivine Challet Meylan,[2] Veronique Kalck,[1] Franziska Moos,[1,13] Simon Suppinger,[1,2,3] Qiutan Yang,[1,11] Jakob Schnabl,[1] Umut Kilik,[5,10,12] Matthieu Bourdon,[1] J. Gray Camp,[5,10] Brigitta Stockinger,[8] Alessandra Ferrari,[7] Marc Bühler,[1,3] Michael B. Stadler,[1,3,9] Edouard Hannezo,[4,*] and Prisca Liberali[1,2,3,15,*]

[1]Friedrich Miescher Institute for Biomedical Research, 4056 Basel, Switzerland
[2]ETH Zürich, Department for Biosystems Science and Engineering (D-BSSE), 4056 Basel, Switzerland
[3]University of Basel, 4001 Basel, Switzerland
[4]Institute of Science and Technology Austria, 3400 Klosterneuburg, Austria
[5]Biozentrum, University of Basel, 4056 Basel, Switzerland
[6]Department of Physics, University of Basel, 4056 Basel, Switzerland
[7]Department of Metabolic Biology and Nutrition, UC Berkeley, Berkeley, CA 94720, USA
[8]The Francis Crick Institute, London NW1 1AT, UK
[9]Swiss Institute of Bioinformatics, 4056 Basel, Switzerland
[10]Institute of Human Biology (IHB), Roche Pharma Research and Early Development, Roche Innovation Center, 4070 Basel, Switzerland
[11]Present address: State Key Laboratory of Stem Cell and Reproductive Biology, Institute of Zoology Chinese Academy of Sciences, 100101 Beijing, P.R. China
[12]Present address: Friedrich Miescher Institute for Biomedical Research, 4056 Basel, Switzerland
[13]Present address: Sartorius Stedim Switzerland AG, 8317 Tagelswangen, Switzerland
[14]These authors contributed equally
[15]Lead contact
*Correspondence: edouard.hannezo@ist.ac.at (E.H.), prisca.liberali@fmi.ch (P.L.)
https://doi.org/10.1016/j.cell.2026.06.009

## SUMMARY

Tissue regeneration requires *de novo* patterning, which has been proposed to be facilitated by cellular heterogeneity. Yet how such heterogeneities are integrated with the mechanochemical state of the tissue and stabilized at the chromatin level into stable, spatially organized fates remains poorly understood. Using *in vivo* mouse intestinal regeneration models and organoids, we identify a critical density regime that produces a permissive window for heterogeneity in the mechanosensor Yes-associated protein 1 (YAP1). We show that YAP1 heterogeneity is coupled to lineage-biased chromatin accessibility and is decoded through FOXA1, which integrates the permissive chromatin state to Delta-Notch supracellular feedback and lineage commitment. This circuit generates fate bistability and preserves a memory of transient YAP1 activity, thereby maintaining spatial patterning as tissues return to homeostasis after injury. Together, our findings establish a multiscale framework in which tissue-scale mechanics tune single-cell competence and, through FOXA1-mediated bistability, convert transient heterogeneity into stable and self-organized tissue architecture.

## INTRODUCTION

The emergence of patterns is fundamental for the spatial organization and function of tissues during development and regeneration.[1–5] Seminal work in developmental biology has shown that initially uniform assemblies of cells become patterned through morphogen gradients[6–14] and direct cell-cell interactions.[15–21] Conversely, during regeneration, cells lose their original fate,[22,23] assuming a fetal-like identity.[24–28] Spatial order and function must then be re-established *de novo*.[3,4] Classical theoretical work has considered patterning as arising from a blank slate, where all cells are initially equivalent,[6–8] and random fluctuations are sufficient to trigger fate asymmetry. Yet, even at the earliest stages of pattern formation, cells exhibit substantial heterogeneity in mechanical, biochemical, and metabolic states.[29–32] Interestingly, such heterogeneity in cellular states can act as pre-patterning cues that initiate fate asymmetry[30,33–40]: in cardiac trabeculation, variability in


This is an open access article under the CC BY-NC license (http://creativecommons.org/licenses/by-nc/4.0/).

Please cite this article in press as: Schwayer et al., Multiscale integration of tissue and chromatin context converts cell heterogeneity into stable intestinal patterning, Cell (2026), https://doi.org/10.1016/j.cell.2026.06.009



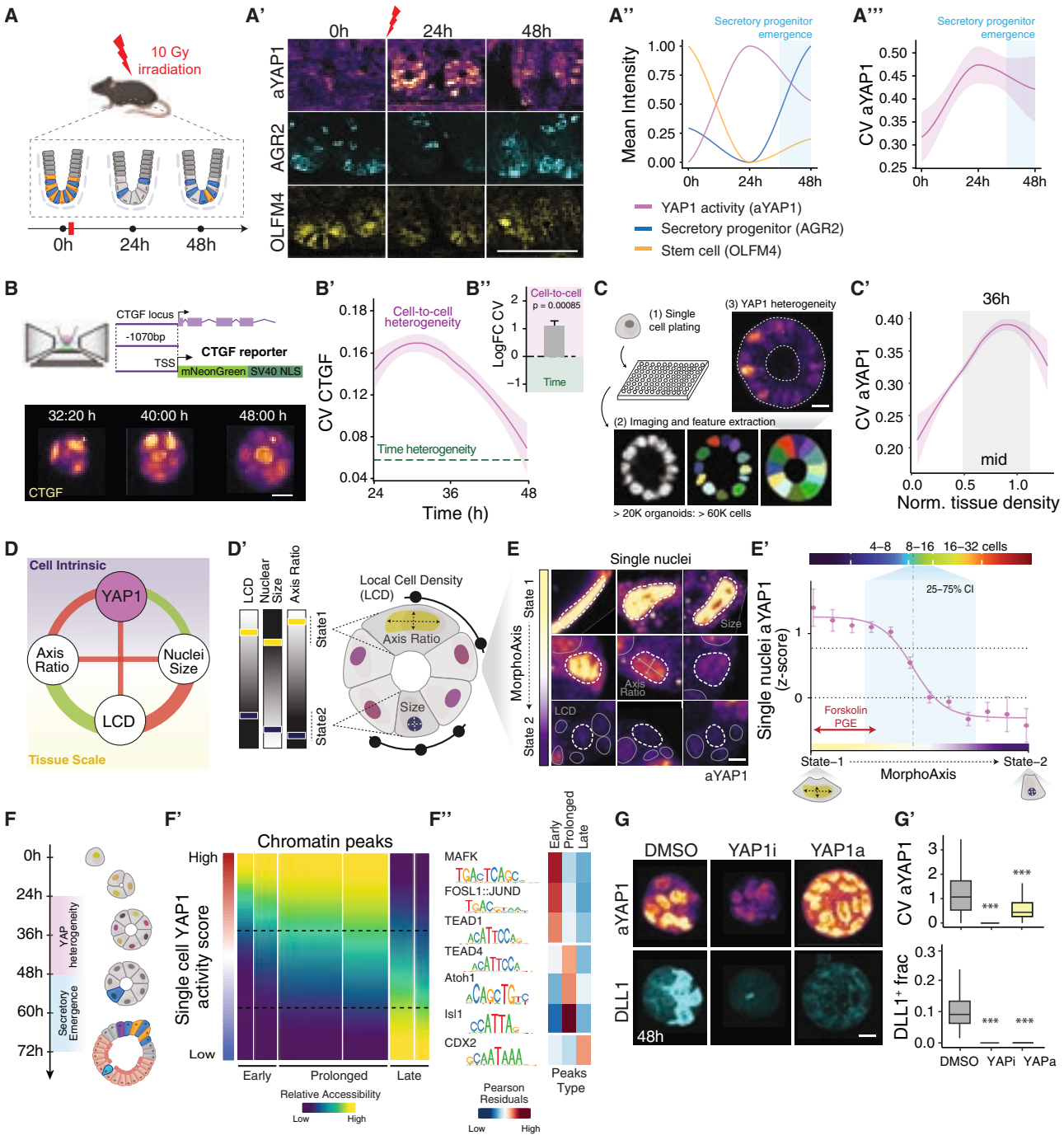


**Figure 1. YAP1 integrates multiscale mechanical cues into lineage-biased chromatin states**

(A) *In vivo* regeneration scheme.

(A′) Representative Z-planes of active YAP1 (aYAP1), AGR2 (secretory progenitor), and OLFM4 (stem cell) immunostaining (scale bars, 100 μm).

(A″ and A‴) Quantification of marker intensities, YAP1 activity, and coefficient of variation (CV) during regeneration ($N$ = 3 mice/time point; $n$ = 170–300 cells/time point from 9–20 crypts).

(B) CTGF reporter design and maximum intensity projections (MIPs) of CTGF-mNeonGreen fused to a nuclear localization signal (NLS) (scale bars, 10 μm).

(B′) Temporal CV of CTGF signal within organoids (dashed line: single-cell temporal heterogeneity; $N$ = 3; $n$ = 96 cells from 6 organoids).

(B″) Relative contributions of cell-to-cell and temporal variability to total CTGF heterogeneity (mean ± standard error of the mean, SEM).

(C) Multi-dimensional organoid workflow (scale bars, 10 μm).

(C′) CV of aYAP1 across normalized tissue density ($N$ = 3; $n$ = 5,065 organoids; gray region: mid-density).

(D) Graphical Gaussian model of YAP1-associated features (edge thickness, partial correlation magnitude; green/red, positive/negative associations).

*(legend continued on next page)*

Please cite this article in press as: Schwayer et al., Multiscale integration of tissue and chromatin context converts cell heterogeneity into stable intestinal patterning, Cell (2026), https://doi.org/10.1016/j.cell.2026.06.009



cortical tension governs selective cell delamination,[29] while variability in cell division timing enhances robustness in embryonic patterning.[41] However, the mechanisms converting tissue-level heterogeneities to stable fate decisions remain elusive, and two key questions remain largely open: first, how are such heterogeneities established, or encoded, at the tissue scale? And second, how are they interpreted, or decoded, by individual cells to form stable, organized patterns in a dynamic multicellular environment?

In intestinal organoids, heterogeneity in the activity of the mechanosensor YAP1 (Yes-associated protein 1) plays a permissive role in initiating Delta-Notch lateral inhibition, giving rise to a subset of secretory cells (Delta-like 1 positive [DLL1$^+$]). This is the first and crucial step in the patterning of the intestinal epithelium during regeneration.[30] Similar roles for YAP1 activation in promoting epithelial progenitor competence and secretory lineage emergence during regeneration have been reported across several epithelial organs.[42–45] YAP1 is therefore recognized as a key mechanosensitive regulator of epithelial plasticity during regeneration. However, how heterogeneity emerges within regenerating multicellular tissues and how such variability is interpreted at the genomic level to drive stable cell fate decisions remain unclear. In particular, a mechanistic link between tissue-scale YAP1 variability and the activation of Delta-Notch signaling has not been established.

Here, we combine high-content single-cell imaging with mathematical modeling to uncover how cell-to-cell variability in YAP1 arises and how it drives pattern formation during intestinal organoid regeneration. We demonstrate that YAP1 heterogeneity emerges at a critical tissue density and can be predicted by a minimal model linking, in a non-linear manner, YAP1 activity to a quantitative morphological-mechanical axis (morphoaxis) that integrates tissue-level features with single-cell morphology. Next, we show that a permissive chromatin landscape links YAP1 activity to fate determination, promoting secretory fate in cells with elevated YAP1 activity. We identify the transcription factor FOXA1 (forkhead box A1) as the central molecular integrator that reads out YAP1-dependent chromatin competence and interacts with Delta-Notch supracellular signaling, enabling transient heterogeneity to resolve into stable fate specification via bistability. Importantly, our mechanistic model—fully constrained by *in vitro* data—faithfully reproduces key features of *in vivo* intestinal regeneration. Together, these findings reveal how tissue-scale architecture can generate transient cellular heterogeneity that is converted into stable and reproducible tissue patterning.

## RESULTS

### Tissue density gates a population-level window of YAP1 heterogeneity during regeneration

To determine how YAP1 heterogeneity emerges and guides patterning, we first asked whether organoids recapitulate the regenerative timeline observed *in vivo*. In irradiated mouse intestine (10 Gy),[46,47] YAP1 activation and loss of lineage markers occurred within 24 h (Figures 1A–1A″ and S1A), followed by reappearance of secretory progenitors at 48 h and delayed recovery of stem cells. Organoids faithfully reproduced this sequence: secretory cells[30] emerged at the 8–16-cell stage (36–48 h) (Figures S1B–S1C), and YAP1 activity became heterogeneous before returning to uniformly low levels at homeostasis (Figures 1A–1A″ and S1B–S1D′). Notably, YAP1 heterogeneity peaked during the 24–48-h window preceding secretory emergence and tissue patterning, both *in vivo* and *in vitro* (Figures 1A‴ and S1D′).

Cell-to-cell variability could arise from pre-existing differences between cells, from intrinsic fluctuations within individual cells over time, or from stable differences between cells at a given time. Because our organoid assay is strictly monoclonal, such that every cell in early (8–16 cell) structures descends from a single founder cell, any heterogeneity is unlikely to reflect pre-existing lineage differences but should arise during regeneration itself. To directly test this, we enriched defined starting populations using established compound treatments[48] and, independently, generated a multi-reporter line marking major intestinal lineages by knocking AGR2 into the STAR stem cell line[49,50] (Figures S1E and S1F). Although starting populations differed in regenerative efficiency (Figures S1E′, S1E″, S1F′, and S1F″), organoids converged by the 8–20 cell stage to similar YAP1 activity and heterogeneity (Figures S1E‴ and S1F‴), excluding cell-of-origin as the source of YAP1 heterogeneity. We next distinguished between the remaining possibilities for the emergence of heterogeneity—temporal fluctuations versus stable intercellular differences—by generating a fluorescent reporter for YAP1 activity based on the target gene *Connective Tissue Growth Factor* (*CTGF*) (Figures 1B, S1G, and S1G′). We found that variability between cells within the same organoid consistently exceeded the fluctuations observed within individual cells over time (Figures 1B–1B″ and S1H–S1J′). Thus, the observed YAP1 heterogeneity primarily reflects population-level differences across cells, rather than dynamic changes within individual cells.

To study how YAP1 heterogeneity arises at the population level, we quantified YAP1 activity at single-cell resolution during

(D′) Morphoaxis gradient schematic defining state-1 and state-2 extremes.
(E) Z-plane images of aYAP1 in nuclei along the morphoaxis (scale bars, 5 μm).
(E′) Quantification of single-nucleus aYAP1 across the morphoaxis (mean ± SEM, sigmoidal fit).
(F) *In vitro* regeneration scheme.
(F′) Chromatin accessibility heatmap of YAP1-associated peaks ordered by single-cell YAP1 activity across early, prolonged, and late states.
(F″) Motif enrichment heatmap of peak groups.
(G) MIPs of DAPI, aYAP1, and DLL1 under DMSO, YAP1 inhibitor (verteporfin), and activator (LATSi [large tumor suppressor kinase inhibitor]) conditions at 48 h (scale bars, 10 μm).
(G′) CV of aYAP1 (top) and fraction of DLL1$^+$ cells per organoid (bottom) under perturbations ($N$ = 3; $n$ = 166 DMSO, 891 YAP1i, 579 YAP1a organoids; boxplots show median, quartiles, and 1.5× interquartile range (IQR) whiskers).
(A‴–C′) Data are mean ± 90% confidence interval (CI).
See also Figures S1–S5.

Please cite this article in press as: Schwayer et al., Multiscale integration of tissue and chromatin context converts cell heterogeneity into stable intestinal patterning, Cell (2026), https://doi.org/10.1016/j.cell.2026.06.009



regeneration. We extended our 3D high-throughput imaging pipeline[26,30] and extracted hundreds of cell-intrinsic (e.g., nuclear shape, cell elongation, or cell volume) and tissue-level features (e.g., number of neighbors, local cell density, and epithelial volume) from thousands of cells and organoids (Figure 1C). YAP1 heterogeneity exhibited a non-monotonic dependence on tissue density: it first increased as organoids reached intermediate cell densities and subsequently collapsed at high densities (Figure 1C′). Although YAP1 activity is known to depend on tissue density,[51,52] it is unclear whether heterogeneity itself is gated by specific density regimes. Global reductions in tissue density, induced by forskolin- or Prostaglandin E2 (PGE2)-driven lumen inflation, suppressed heterogeneity and enforced uniformly high YAP1 activity (Figures S2A–S2A′′′). Restoring tissue density by halting lumen inflation with the cystic fibrosis transmembrane conductance regulator (CFTR) inhibitor or culturing organoids in 2D, where density remains constant, abolished these effects, demonstrating that YAP1 changes reflect mechanosensing rather than second messenger signaling (Figures S2B–S2C′′). Consistently, acute or sustained cell ablation—via laser or DTR-based genetic approaches—similarly altered density and both YAP1 levels and heterogeneity (Figures S2D–S2E′′′). Engineering defined tissue densities in microwells[55] further confirmed that YAP1 heterogeneity is determined by density independent of curvature (Figures S2F–S2F′′). Together, these data identify a defined intermediate-density range (0.5–1.1 reference nuclei per 100 $\mu m^2$) that maximizes YAP1 heterogeneity and coincides with the window of tissue patterning *in vivo* and *in vitro* (Figures 1A′′′, S1B–S1D′, S2G, and S2H). Organoids that failed to reach this threshold did not pattern (Figures S3A and S3A′). Experimentally maintaining low density—by inhibiting proliferation with aphidicolin[53] or taxol[54,55] or inducing lumen inflation—prevented secretory progenitor emergence (Figures S3B–S3C′), whereas washout of division inhibitors restored tissue density and partially rescued patterning (Figures S3B–S3B′′).

Together, these findings demonstrate that YAP1 heterogeneity is a population-level property, arising within a defined tissue-density regime, likely as a sensor of tissue integrity, that creates a permissive window for fate specification to restore patterning after regeneration.

## YAP1 integrates multiscale mechanical cues into lineage-biased chromatin states

To understand how tissue density is encoded into YAP1 activity, we analyzed the single-cell morphological and mechanical features across regenerating organoids. Morphological and mechanical variables exhibited heterogeneity dynamics closely mirroring YAP1 (Figures S1D′, S4A, and S4A′). Least absolute shrinkage and selection operator (LASSO) stability selection[56] revealed that YAP1 activity arises from the integration of cell-intrinsic properties (nuclear size and shape) and tissue-level context (local cell density, organoid size, and developmental time), together explaining ~40% of its variance (Figures S4B and S4C). To estimate the network of conditional dependencies between mechanical predictors and YAP1 activity, we applied graphical Gaussian modeling.[57,58] This analysis revealed that increased local cell density suppresses YAP1 both directly and indirectly, through its effects on nuclear size and geometry (Figures 1D and S4D).

Together, these relationships define a continuous morphological axis, or *morphoaxis*, that integrates nuclear morphology and local tissue density into a latent epithelial architecture governing YAP1 activity (Figures 1D and 1D′). Along this axis, YAP1 varied smoothly from $YAP1^{high}$ cells with large, elongated nuclei in sparse environments to $YAP1^{low}$ cells with small, round nuclei in crowded regions (Figures 1D–1E′ and S4E). Notably, the relationship between YAP1 activity and morphoaxis position was sigmoidal, with the 8-16-cell stage positioned near the inflection point (Figure 1E′). This non-linear mapping predicts that identical variance in morphoaxis position can generate maximal YAP1 heterogeneity specifically within this high-gain regime (Figures S4F and S4F′). Consistently, the sigmoidal model accurately predicted both the peak of YAP1 heterogeneity and the reduced heterogeneity observed under all perturbation conditions (Figures 1E′, S2A–S2A′′′, and S2E–S2E′′′). Projection of *in vivo* and microwell-cultured cells onto the morphoaxis revealed that both datasets collapse onto the master YAP1-morphoaxis curve defined in organoids, demonstrating conservation across systems (Figures S4G and S4H).

We next asked whether differences in nuclear YAP1 activity translate tissue mechanics into fate bias through transcriptional regulation. Given YAP1's role as a transcriptional co-regulator,[59,60] we performed single-cell assay for transposase-accessible chromatin using sequencing (ATAC-seq; Figure 1F). Consistent with prior *in vivo* studies,[61] regeneration was accompanied by widespread chromatin accessibility changes across regenerating cells, spanning nearly twice as much of the genome as those linked to secretory fate specification (Figures S5A and S5A′). We stratified cells according to YAP1 activity (Figure 1F; STAR Methods), identifying thousands of chromatin regions whose accessibility correlated with YAP1 levels (Figure 1F′). Regions accessible in $YAP1^{high}$ cells were enriched for AP1-associated factors, whereas regions enriched in $YAP1^{low}$ cells were associated with canonical intestinal regulators such as CDX2 (Figure 1F′′). Notably, chromatin regions accessible at intermediate YAP1 levels were enriched for secretory lineage motifs, including atonal BHLH transcription factor 1 (ATOH1), defining a state permissive for secretory specification (Figure 1F′′). Because secretory commitment is executed through Delta-Notch-mediated lateral inhibition, we asked whether YAP1-dependent chromatin bias selectively engages specific Delta ligands. Although both DLL1 and DLL4 were expressed at early organoid stages (Figures S5B–S5C′′), YAP1 activation preferentially increased DLL1 while suppressing DLL4, as revealed by RNA sequencing and imaging (Figures S5D–S5F′).

Consistent with a role for YAP1 in DLL1 emergence, $DLL1^{+}$ cells exhibited intermediate-to-high YAP1 activity during the 8-20-cell transition (Figures S5G–S5G′′). Uniform inhibition of YAP1[62] abolished DLL1 patterning (Figures 1G, 1G′, S5H, and S5I), confirming that YAP1 activity is required to initiate DLL1 expression. However, in wild-type organoids, many $YAP1^{high}$ cells remained $DLL1^{-}$, indicating that YAP1 activity alone is not sufficient to specify DLL1 fate (Figures S5G′, S5J, and S5K). Although YAP1 activation increased DLL1 expression, most mature secretory markers were reduced (Figure S5D),

Please cite this article in press as: Schwayer et al., Multiscale integration of tissue and chromatin context converts cell heterogeneity into stable intestinal patterning, Cell (2026), https://doi.org/10.1016/j.cell.2026.06.009



suggesting that YAP1 promotes secretory competence rather than lineage maturation. Consistently, uniform activation of YAP1 across all cells induced homogeneous intermediate DLL1 expression but failed to generate fully mature DLL1$^+$ cells (Figures 1G, 1G′, and S5I). These findings indicate that YAP1 establishes a permissive chromatin state but does not instruct DLL1 fate.

## YAP1 heterogeneity and DLL1 bistability drive tissue patterning

We next asked how transient YAP1 heterogeneity is converted into a stable cell fate pattern at the tissue level. Because YAP1 activity is permissive but not instructive, this process must involve an additional tissue-level regulatory mechanism.

To identify possible regulatory networks capable of performing this conversion, we developed a mathematical model of tissue patterning aimed at generating experimentally testable predictions linking YAP1 heterogeneity to fate specification. Classical models have explained DLL1 patterning through lateral inhibition, a process in which signaling between neighboring cells suppresses the adoption of similar fates.[16–18,63] To integrate YAP1 regulation of DLL1 with classical lateral inhibition,[16–18] we describe the DLL1 dynamics of each cell as a dynamical system controlled by the interplay of the YAP1 activity of that cell and the lateral signal, defined as the average DLL1 level of a cell's immediate neighbors. Similar to Waddington's metaphor of cell fates as valleys in a landscape,[64–66] our model defines DLL1$^+$ and DLL1$^-$ fates as stable points, or attractors, whose locations are determined by the combination of YAP1 and lateral signal (Figure 2A). Focusing on the 16-cell stage, when initial patterning emerges (Figure S5K), we generated three-dimensional spatial neighborhood graphs with each cell represented by a node, and edges representing direct contact between neighbors (Figure 2B). The connectivity statistics of these graphs are directly inferred from experiments (Methods S1; Figures S6A–S6A‴). Experimentally, we find that YAP1 activity of neighboring cells is uncorrelated (Figures S6D and S6D″), and we therefore generate heterogeneous YAP1 activity by randomly assigning values based on the experimentally measured distribution of YAP1 activity (Figure 2B; Methods S1). These neighborhood graphs served as input for simulations of proposed YAP1-DLL1 regulatory interactions, allowing us to predict DLL1 patterns (fraction of DLL1$^+$ cells per organoid) as model outputs (Figure 2B). We tested two initial models: the YAP1-prepatterned DLL1 activation and the interaction model. For each scenario, we systematically screened a wide range of model parameters (Methods S1; Figures S6B–S6C‴). In the first model, YAP1 pre-patterns the initial levels of DLL1 in a cell-autonomous manner (Figures S6C and S6E). This approach explained the outcome of YAP1 activation but failed to account for the loss of DLL1 expression following YAP1 inhibition (Methods S1; Figures 1G and 1G′, and S6C). In the second model, YAP1 modulates the strength of lateral inhibition, determining how much DLL1 is produced in response to lateral signals (Methods S1; Figures S6C′ and S6E′). While this model correctly predicted the effects of YAP1 inhibition, it could not recapitulate the DLL1 levels observed upon YAP1 activation (Figures 1G and 1G′). Together, these results suggest that neither a purely cell-autonomous model nor one based solely on lateral inhibition can fully explain the experimental data, indicating the need for a fundamentally different mechanism to account for both wild-type and perturbed conditions.

We next tested a more complex model in which YAP1 plays a dual role: activating DLL1 expression within individual cells while also modulating lateral interactions. This integrated model successfully captured both YAP1 inhibition and activation outcomes across a broad parameter space (Methods S1; Figures S6C″ and S6E″). However, a limitation of this model is that it assumes a direct, unique relationship between DLL1 levels and neighboring cell signals for any given YAP1 activity. As a result, the model predicts that DLL1 expression and secretory progenitor fate will be lost at homeostasis due to YAP1 downregulation—contrary to experimental observations (Figures S1B–S1B″). This discrepancy suggests the presence of a "memory" mechanism preserving DLL1 expression beyond the period of high YAP1 activity. The simplest theoretical explanation for this "memory effect" is the existence of additional regulatory interactions that allow YAP1$^{low}$ cells to retain a stable DLL1$^+$ state. Incorporating this feature into the model (Methods S1; Figures S6C‴ and S6E‴) produced DLL1 behavior that depends non-monotonously on both YAP1 activity and lateral signal (Figure 2C). This model defines a three-dimensional manifold that specifies which DLL1 attractor states are available as a function of both the intrinsic features (single-cell level of YAP1) and extrinsic features (average lateral inhibition) (Figure 2C). Specifically, cells in a YAP1$^{high}$ state show higher sensitivity to the environment, modulating DLL1 production as a function of the lateral inhibition received. By contrast, cells in a YAP1$^{low}$ state become insensitive to the neighbors (Figure S7A). This leads to fate bistability,[18] meaning that YAP1$^{low}$ cells exhibit two attractors at both DLL1$^+$ and DLL1$^-$ states (Figures 2C and S7A). As the two attractor states are separated by an activation barrier, YAP1 activity acts as the control parameter, enabling cells to access the DLL1$^+$ state. To reach the DLL1$^+$ fate at later stages (e.g., at the >32-cell stage), cells must first transition through a YAP1$^{high}$ state, as occurs at the 16-cell stage (Figures 2C and 2D). Once the DLL1$^+$ state is established, it is stably maintained—as confirmed by light-sheet imaging of DLL1 expression from 24–72 h (Figures 2E, 2E′, and S7B)—and the majority of DLL1$^+$ cells will be in a YAP1$^{low}$ state (Figures S7C and S7C′). The model recapitulates the wild-type DLL1$^+$ cell fraction (Figure 2F), the effect of YAP1 perturbations (Figures 2G, 2H, and S7D), and single-cell YAP1-DLL1 correlations (Figure S7E) and quantitatively outperforms other model candidates (Tables S1 and S2). Moreover, it predicts that, similar to the inhibition, YAP1 activation disrupts DLL1 patterning. However, in this case, the disruption results in uniform intermediate DLL1 expression, as cells mutually inhibit each other via lateral inhibition, hence inhibiting patterning. Imaging confirmed this, revealing more un-patterned organoids and an increased number of organoids with intermediate DLL1 expression (Figures S7D and S7F). To further experimentally test the model without altering cell-intrinsic YAP1 activity, we perturbed lateral inhibition. The model predicted that disrupting cell-cell communication would increase the fraction of DLL1$^+$ cells. Supporting this, Notch inhibition with the γ-secretase inhibitor DAPT[67] (N-[N-(3,5-Difluorophenacetyl)-L-alanyl]-S-phenylglycine t-butyl ester) led to

Please cite this article in press as: Schwayer et al., Multiscale integration of tissue and chromatin context converts cell heterogeneity into stable intestinal patterning, Cell (2026), https://doi.org/10.1016/j.cell.2026.06.009



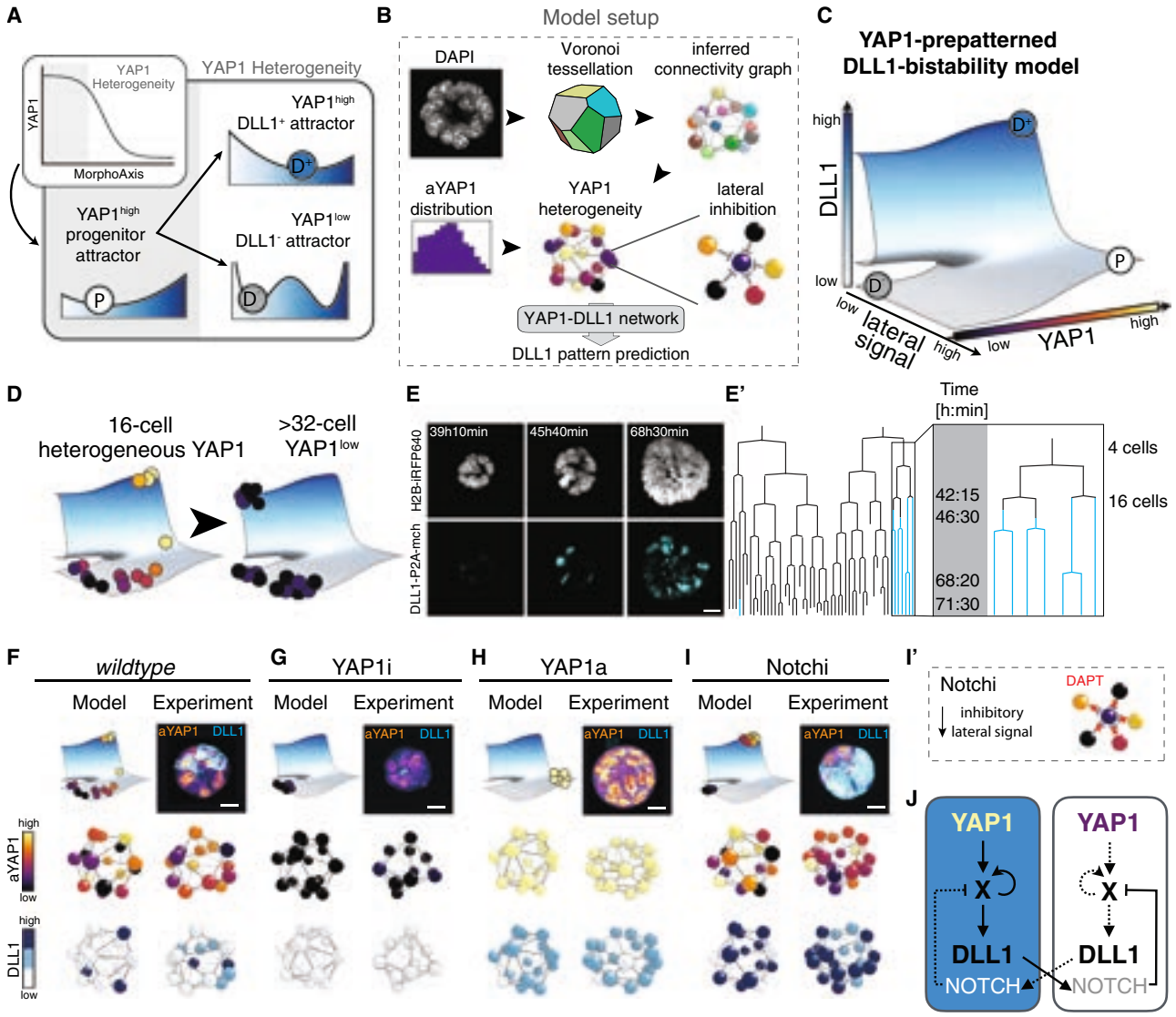


**Figure 2. YAP1 heterogeneity and DLL1 bistability drive patterning**

(A) Schematic of the proposed attractor structure, where YAP1$^{high}$ progenitors transition to DLL1$^{+/-}$ states.

(B) Model framework: 3D-segmented organoids are converted into connectivity graphs via Voronoi tessellation; simulated graphs sample experimental YAP1 distributions to compute lateral inhibition signals and predict DLL1 patterns.

(C) Attractor manifold of the YAP1-prepatterned DLL1 bistability model, showing stable DLL1 states as a function of YAP1 activity and neighbor-derived inhibition. Color indicates DLL1 level, and the surface gap denotes the bistability barrier.

(D) Attractor surfaces across developmental stages (16-cell heterogeneous YAP1 versus >32-cell low YAP1 organoids).

(E) Time-lapse snapshots of DLL1 reporter organoids (24–72 h; scale bars, 15 μm).

(E′) Lineage trees and single-cell tracks of DLL1$^{+}$ (blue) and DLL1$^{-}$ (black) cells.

(F) Neighborhood graph analysis of simulated (left) and experimental (right) organoids, showing DLL1$^{+}$ cell fractions (mean ± SEM; experiment: $N = 3$, $n = 340$ organoids; model: $n = 1{,}000$ simulations). DLL1 levels are classified as low, intermediate, or high (thresholds: 0.2 and 0.7).

(G–I) Attractor surfaces and neighborhood graphs for YAP1 inhibition (G), YAP1 activation (H), and Notch perturbation (I) (left), with corresponding experimental MIPs of aYAP1 and DLL1 and graph representations (right; YAP1 signal scaled 2× lower in H).

(I′) Schematic of Notch perturbation.

(J) Summary schematic of the YAP1-prepatterned DLL1 bistability model.

See also Figure S6.

a shift from the typical alternating DLL1-hairy and enhancer of split 1 (HES1) pattern to a net increase in DLL1$^{+}$ cell number (Figures 2I, 2I′, and S7G–S7H″). This experiment also confirmed our assumption that YAP1 acts upstream of DLL1 patterning as, despite the perturbed DLL1 pattern, YAP1 heterogeneity remains unchanged (Figures S7I–S7I″). Together, these findings

Please cite this article in press as: Schwayer et al., Multiscale integration of tissue and chromatin context converts cell heterogeneity into stable intestinal patterning, Cell (2026), https://doi.org/10.1016/j.cell.2026.06.009



CellPress
OPEN ACCESS

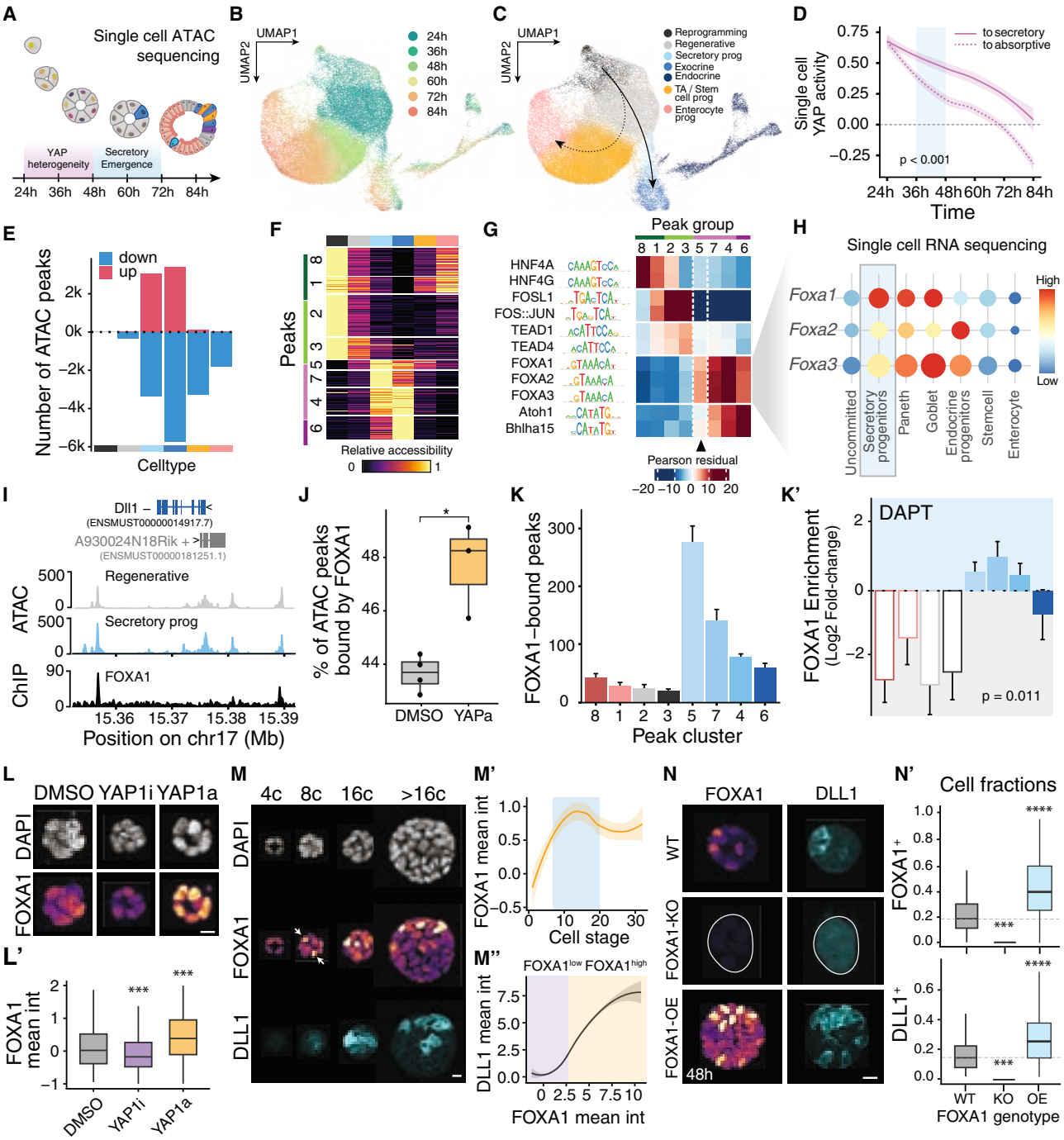


**Figure 3. Chromatin accessibility changes link YAP1 activity to secretory fate priming**

(A) Schematic of single-cell ATAC-seq time course.

(B and C) Uniform manifold approximation and projection (UMAP) projections colored by time (B) and cell type (C). Arrows indicate inferred trajectories toward absorptive (dashed) or secretory (solid) lineages.

(D) Mean YAP1 activity over time along absorptive (dashed) and secretory (solid) trajectories. Shaded region marks secretory emergence (36–48 h).

(E) Number of peaks gaining (red) or losing (blue) accessibility (|log fold change [FC]| > 0.81) relative to reprogramming cells.

(F) Heatmap of accessibility dynamics across cell types.

(G) Motif enrichment heatmap of selected peak groups.

(H) Dot plot of FOXAs expression across cell types.

(I) Representative ATAC-seq and ChIP-seq signals at the DLL1 locus in regenerative and secretory progenitor cells.

*(legend continued on next page)*

Please cite this article in press as: Schwayer et al., Multiscale integration of tissue and chromatin context converts cell heterogeneity into stable intestinal patterning, Cell (2026), https://doi.org/10.1016/j.cell.2026.06.009



highlight how fate bistability locks early heterogeneities into defined states, linking tissue-level YAP1 heterogeneity to robust cell-intrinsic patterning mechanisms.

Our model raises a central question: how is the dual role of YAP1 in both cell-intrinsically activating DLL1 expression and modulating cell-extrinsic lateral interactions implemented at the molecular level? Theoretically, such dual control could operate through an intermediate factor (denoted X in Figure 2J) that would fulfill this role if it (1) links YAP1 to DLL1, (2) exhibits self-activation to support bistability, and (3) is repressed by DLL1 in neighboring cells via trans-activation of Notch.

## FOXA1 specifies secretory fate downstream of YAP1

To identify the intermediate factor predicted by our model, we examined how YAP1-associated chromatin accessibility evolves during regeneration. Focusing on the period preceding DLL1 emergence (24–36 h), we annotated cellular states based on chromatin accessibility profiles and identified two early populations (Figures 3A–3C, S8A, and S8B). Reprogramming cells retained accessibility at mature epithelial markers (e.g., *Alpi*, *Aldob*, and *Apoa1*) while activating YAP1-associated regenerative genes (e.g., *Yap1*, *Areg*, *Anxa3*, and *Ajuba*)[22,30,46,61] but lacked canonical stem cell features (*Lgr5*, *Olfm4*, *Smoc2*, and *Ascl2*). Regenerative cells lost epithelial identity while maintaining the YAP1-associated regenerative signature and began reacquiring accessibility at stem cell loci. From this regenerative state, cells diverged into two principal lineages: DLL1$^+$ secretory progenitors and Notch-associated transit amplifying (TA) cells, which subsequently matured into absorptive progenitors (Figures 3C, S8A, and S8B). Cells committing to the secretory lineage retained higher YAP1 activity than absorptive-biased cells (Figure 3D), consistent with our model of YAP1 pre-patterning DLL1 expression.

Lineage commitment was accompanied by a marked asymmetry in chromatin dynamics. TA and absorptive progenitors predominantly lost accessibility, whereas secretory progenitors exhibited both gains and losses (Figure 3E). Chromatin accessibility progressively declined as YAP1 activity decreased in DLL1$^-$ cells, supporting a default differentiation trajectory characterized by chromatin closure (Figure S8C). By contrast, DLL1$^+$ cells maintained higher accessibility. To identify regulatory elements underlying these chromatin trajectories, we grouped differentially accessible peaks according to cell type-specific accessibility patterns (Figure 3F). Notably, a subset of regions associated with secretory progenitors (group 5) gained accessibility already in regenerative cells, marking the population of secretory-primed cells that exhibited higher YAP1 activity (Figures S8D–S8E′). Motif enrichment analysis revealed distinct regulatory modules (Figures 3G, S8F, and S8G). The absorptive trajectory was characterized by AP1-like (FOS-JUN) and HNF4 (hepatocyte nuclear factor 4) motif co-occurrence (groups 1 and 2), resolving into HNF4 dominance as chromatin accessibility decreased during maturation (group 8). By contrast, a separate peak group was enriched for AP1 and TEA domain transcription factor (TEAD) motifs but lacked HNF4 (group 3), consistent with a YAP1-associated regulatory module that may counter the default absorptive program (Figure 3G). Within the secretory lineage, ATOH1 motifs were enriched in peaks associated with mature and progenitor secretory cells (groups 7, 4, and 6). However, the secretory-primed peak group 5 lacked ATOH1 enrichment and instead showed strong FOXA motif enrichment (Figure 3G).

Among FOXA family members, FOXA1 emerged as a key candidate due to its specific expression in DLL1$^+$ secretory progenitor cells (Figures 3H and S9A–S9A″). We therefore asked whether FOXA1 fulfills the regulatory properties predicted by our model. Chromatin immunoprecipitation followed by sequencing (ChIP-seq) confirmed FOXA1 binding at secretory regulatory loci, including *Dll1* and *Atoh1* (Figures 3I and S9B). Notably, FOXA1 bound its own locus (Figure S9B′), suggesting potential autoregulation, consistent with the self-reinforcing property predicted by our bistability model. We next asked whether YAP1 regulates FOXA1 chromatin binding. FOXA1 ChIP-seq performed under YAP1 activation revealed increased FOXA1 occupancy genome-wide (Figure 3J). If FOXA1 acts downstream of YAP1 to prime secretory fate, it should preferentially bind regulatory elements that open in secretory-primed cells. Consistent with this prediction, FOXA1 ChIP signal was significantly enriched at group 5 ATAC peaks, the regions that gain accessibility in secretory-primed cells (Figure 3K). Our model further predicts that this intermediate factor is modulated by lateral inhibition. Accordingly, inhibition of Notch signaling using DAPT[67] further increased FOXA1 specificity at secretory regulatory sites (Figure 3K′). FOXA1 induction itself occurred independently of Notch signaling, as predicted by the model: perturbation of YAP1 activity in early organoids (<8 cells) showed that FOXA1 expression decreased upon YAP1 inhibition and increased upon YAP1 activation (Figures 3L and 3L′), prior to Delta-Notch patterning.

(J) FOXA1 ChIP signal across ATAC-defined peak groups in control and YAP1 activation (LATSi) conditions (Ctrl: $n = 4$; YAPa: $n = 3$ independent experiments; loess-normalized counts per million [CPM]).
(K) Number of FOXA1-bound peaks across peak groups (log2(IP/input) > 1.5; $n = 4$ independent experiments).
(K′) FOXA1 enrichment (log2(IP/input)) following Notch inhibition (DAPT) relative to DMSO (Ctrl: $n = 4$; DAPT: $n = 3$ independent experiments).
(L) MIPs of DAPI and FOXA1 in early organoids (<8-cell stage) under DMSO and YAP1 perturbations ($N = 3$; $n = 456$ DMSO, 972 YAP1i, 1,134 YAP1a organoids).
(L′) Quantification of FOXA1 intensity.
(M) MIPs of DAPI, FOXA1, and DLL1 across developmental stages (scale bars, 10 μm; arrowheads indicate FOXA1 preceding DLL1).
(M′) FOXA1 nuclear intensity across stages (mean ± 90% CI; shaded region indicates DLL1 emergence; $N = 3$, $n = 960$ organoids).
(M″) Correlation of FOXA1 and DLL1 intensities in single cells at 8–20 cell stages ($N = 3$, $n = 195$ organoids).
(N) MIPs of wild-type (WT), FOXA1 knockout (KO), and overexpression (OE) organoids at 48 h (scale bars, 10 μm).
(N′) FOXA1$^+$ (top) and DLL1$^+$ (bottom) cell fractions ($N = 3$; $n = 263$ WT, 331 KO, 351 OE organoids).
Statistical significance: $^*p < 0.05$ and $^{***}p < 0.001$. Boxplots show median, quartiles, and 1.5× IQR whiskers.
See also Figures S7 and S8.

Please cite this article in press as: Schwayer et al., Multiscale integration of tissue and chromatin context converts cell heterogeneity into stable intestinal patterning, Cell (2026), https://doi.org/10.1016/j.cell.2026.06.009



CellPress
OPEN ACCESS

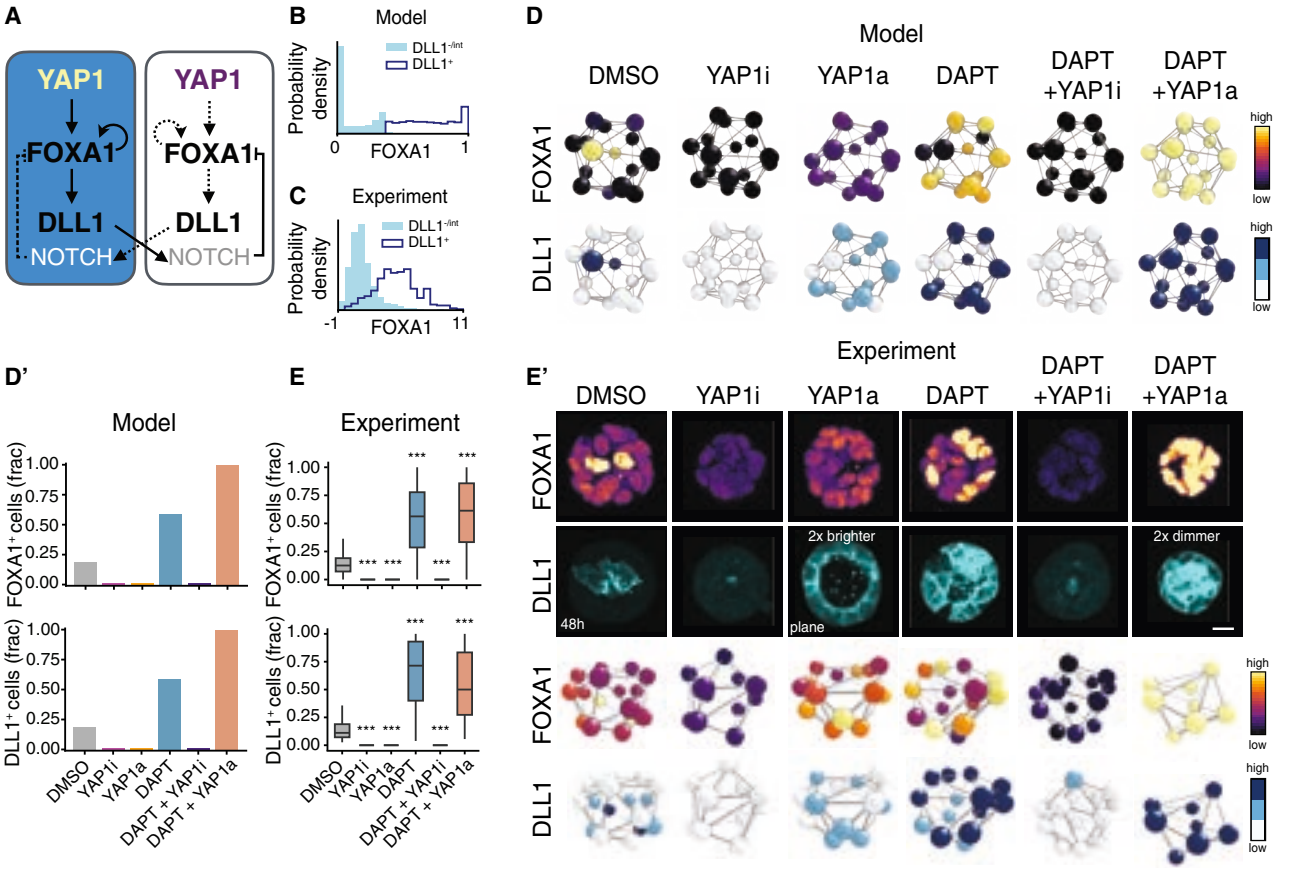


**Figure 4. FOXA1 mediates fate bistability by integrating YAP1 pre-patterning with lateral inhibition**

(A) Schematic of the YAP1-prepatterned DLL1 bistability model incorporating FOXA1 as an intermediate regulator.

(B and C) Predicted (B) and experimental (C) distributions of FOXA1 levels in DLL1$^{-/int}$ (light blue) and DLL1$^{+}$ (dark blue) cells.

(D) Neighborhood graph plots of model predictions for FOXA1 (top) and DLL1 (bottom) across perturbations; DLL1 is classified as low, intermediate, or high. (D′) Predicted fractions per organoid ($n$ = 1,000 simulations; SEM negligible).

(E) Experimental fractions of FOXA1$^{+}$ and DLL1$^{+}$ cells per organoid across conditions ($N$ = 3; $n$ = 351 DMSO, 1,352 YAP1i, 1,689 YAP1a, 838 DAPT, 1,367 DAPT+YAP1i, 636 DAPT+YAP1a organoids). Boxplots show median, quartiles, and 1.5× IQR whiskers.

(E′) MIPs of FOXA1 and DLL1 under perturbations (scale bars, 10 μm; DLL1 signal in DAPT+YAP1a shown 2× dimmer; YAP1a Z-plane 2× brighter), with corresponding neighborhood graphs of FOXA1 levels (top) and DLL1 classification (bottom).

See also Figures S9 and S10.

We next examined how FOXA1 relates to DLL1 expression. The FOXA1 protein appeared earlier during regeneration (4–8 cell stage) and strongly correlated with DLL1 levels at later stages (8–20 cells) (Figures 3M–3M″, S9C, and S9C′). To directly assess FOXA1 function in secretory fate specification, we genetically manipulated FOXA1 levels (Figures 3N, 3N′, and S9D–S9E′). FOXA1 knockout organoids failed to establish DLL1 patterning, demonstrating that FOXA1 is required for secretory progenitor specification (Figures 3N, 3N′, and S9D). Previous studies have suggested partially overlapping roles for FOXA1 and FOXA2 in secretory differentiation.[68,69] FOXA1 ChIP-seq revealed binding at the *Foxa2* locus (Figure S9F), and FOXA1 deletion reduced FOXA2 expression (Figure S9D). However, while FOXA1 knockout abolished DLL1 patterning, FOXA2 knockout did not significantly affect the expression of secretory progenitor markers (Figures S9G–S9G″). These findings indicate that FOXA1 functions upstream in initiating secretory progenitor commitment, whereas FOXA2 likely contributes at later stages of lineage maturation. Consistent with a broader role in secretory lineage initiation, FOXA1 ChIP-seq revealed binding at both the *Dll1* and *Dll4* loci (Figures S9H–S9H‴), and FOXA1 overexpression was sufficient to significantly increase the abundance of DLL1$^{+}$ and DLL4$^{+}$ cells (Figures S9I–S9J″). Although FOXA1 overexpression increased the fraction of DLL1$^{+}$ cells per organoid, inhibition of Notch signaling further expanded this population (Figures S9E and S9E′), indicating that while FOXA1 promotes DLL1 expression, the size of the DLL1$^{+}$ population remains constrained by tissue-scale lateral inhibition.

Altogether, our findings identify FOXA1 as the intermediate factor predicted by our model: YAP1 activity establishes a permissive chromatin landscape in regenerative cells, and in cells retaining YAP1 activity for longer, FOXA1 drives the commitment to secretory fate.

Please cite this article in press as: Schwayer et al., Multiscale integration of tissue and chromatin context converts cell heterogeneity into stable intestinal patterning, Cell (2026), https://doi.org/10.1016/j.cell.2026.06.009



### FOXA1 mediates fate bistability by integrating YAP1 pre-patterning with lateral inhibition

Having identified FOXA1 as the molecular link between YAP1 activity and DLL1 expression (Figure 4A), we next asked whether it also implements the regulatory interactions required for DLL1 bistability. To test this, we incorporated FOXA1 into our mathematical model, positioning it as an integrator of both intrinsic YAP1 activity and extrinsic lateral inputs from neighboring DLL1$^+$ cells (Methods S1; Figures 4A and S10A–S10B‴).

Lateral inhibition is likely mediated through trans-activation of Notch and its downstream effector HES1, a known repressor of DLL1.[70] Consistent with this hypothesis, predicted HES1 binding sites at the FOXA1 locus (putatively negative sites of regulation) displayed lower signals in secretory progenitors compared with non-FOXA1-expressing cells (e.g., enterocyte progenitors), supporting the hypothesis of a direct FOXA1 repression by HES1 (Figures 4A and S9K). This regulatory architecture, which integrates YAP1 activity and lateral inhibition, predicts a tight correlation between FOXA1 and DLL1 at the single-cell level (Figure 4B). Indeed, FOXA1 expression levels were strongly correlated with DLL1 both in simulations (Figure 4B) and experimentally (Figures 3M″ and 4C). Furthermore, consistent with experiments, the model predicts low FOXA1 levels under YAP1 inhibition and intermediate levels under YAP1 activation (Figures 4D and 4D′). Importantly, although a positive regulation of YAP1 by FOXA1 has been observed in liver cancer cells,[71] we ruled out this regulatory relationship in the intestinal system (Methods S1; Figures S10C–S10C‴). To confirm that lateral inhibition represses FOXA1 via Notch, we perturbed Notch signaling using DAPT.[67] In the absence of lateral inhibition, the model predicted—and experiments confirmed—increased fractions of both FOXA1$^+$ and DLL1$^+$ cells, consistent with de-repression of FOXA1 (Figures 4D–4E′).

This framework—where YAP1 activates FOXA1, while lateral signals from DLL1$^+$ neighbors inhibit FOXA1—explains how single cells integrate both intrinsic and extrinsic signals. The resulting landscape predicts complex, non-linear behaviors under combined perturbations (Figures 2C, S10D, and S10D′). First, the model predicts that while Notch inhibition alone increases DLL1 (Figures 2I, 2I′, 4D, and 4D′)[67] simultaneous inhibitions of YAP1 and Notch prevent DLL1$^+$ fate altogether. This occurs because, in the absence of YAP1 activity, cells stabilize in a DLL1$^-$ state regardless of lateral input (Figures 2D, 2E, 4D, and 4D′). Experimentally, this was confirmed by the complete loss of DLL1$^+$ cells under dual inhibition (Figures 4E and 4E′, DAPT+YAPi panel), underscoring the essential role of YAP1 pre-patterning. Second, although YAP1 activation disrupts DLL1 patterning by locking cells into an intermediate DLL1 state, where mutual inhibition blocks fate progression, our model predicts that this block could be lifted by simultaneous Notch inhibition (Figures 4D and 4D′). The removal of lateral inhibition allows specification into the DLL1$^+$ fate, increasing the fraction of both FOXA1$^+$ and DLL1$^+$ cells. This prediction was also validated: in organoids with uniformly high YAP1 activity, Notch inhibition restored the ability to specify DLL1$^+$ state (Figures 4E and 4E′, DAPT+YAPa panel). Together, these results validate a model in which FOXA1 integrates cell-intrinsic YAP1 activity and cell-extrinsic lateral inhibition to generate robust DLL1$^+$ fate bistability.

### Heterogeneity-driven bistability controls patterning during *in vivo* regeneration

Having constrained our model using *in vitro* organoid data, we next asked whether it could predict patterning dynamics during *in vivo* regeneration. Using the temporal YAP1 trajectory observed during regeneration *in vivo* (Figures 1A, 1A′, and S2G–S2G‴), we simulated FOXA1 and DLL1 patterning over time on a 2D cellular lattice (Figures S11A–S11A″ and S11C; Methods S1). The model predicts that FOXA1 and DLL1 levels are tightly correlated, with FOXA1$^+$ and DLL1$^+$ cells emerging around 48 h—and remaining stably patterned even after YAP1 activity diminishes (Figures 5A and 5A′). These predictions align closely with *in vivo* observations: FOXA1 expression is upregulated 48 h after injury, concurrent with the appearance of secretory progenitors (Figures 5B, 5B′, S11A‴, and S11A⁗). Our model further predicts that sustained YAP1 activity following injury would impair tissue re-patterning (Figures 5C and 5C′). To test this *in vivo*, we administered a LATS inhibitor[72] after irradiation during regeneration, thereby prolonging YAP1 activation (Figures S11B and S11B′). Sustained YAP1 activity disrupted pattern re-establishment (Figures 5D and 5D′), demonstrating that YAP1 downregulation is required for restoration of tissue organization during regeneration.

A key consequence of FOXA1-mediated bistability in our model is a memory effect, wherein cells retain the DLL1$^+$ state even after YAP1 activity subsides (Figure 2D). This feature enables cells to convert transient, heterogeneous YAP1 signals into lasting lineage specification, stabilizing patterning as the tissue transitions to homeostasis. To exclude alternative mechanisms where cells might become insensitive to YAP1 via complex biochemical processes, we activated YAP1 *in vivo* during homeostasis for 2.5 days.[72] As predicted by the model (Figures 5E and 5E′), uniform YAP1 activation during *in vivo* homeostasis disrupted existing patterning, resulting in a loss of secretory progenitor cells (Figures 5F and 5F′). This confirms that YAP1 acts as a critical control parameter not only during regeneration but also in maintaining tissue homeostasis. Notably, our data suggest that YAP1 activation alone is sufficient to re-sensitize cells to neighbors' lateral inputs, with cells starting to mutually inhibit each other, functionally disrupting existing patterns even in the presence of a homeostatic niche. Together, these results demonstrate that transient YAP1 heterogeneity, interpreted through FOXA1-mediated bistability and lateral inhibition, is both necessary and sufficient to establish robust, self-organized patterning of secretory progenitors.

## DISCUSSION

Here, we present a multiscale model of heterogeneity-driven tissue patterning. We demonstrate that YAP1 heterogeneity arises as intercellular differences during regeneration, rather than from pre-existing cell identity or transient oscillatory dynamics. This heterogeneity is gated by the tissue state: it emerges only once a critical intermediate tissue density is reached, and epithelial integrity has been re-established. Tissue density therefore functions as a regenerative timer, creating a defined window of opportunity during which patterning can occur. Mechanistically, this intermediate-density state positions cells within the

Please cite this article in press as: Schwayer et al., Multiscale integration of tissue and chromatin context converts cell heterogeneity into stable intestinal patterning, Cell (2026), https://doi.org/10.1016/j.cell.2026.06.009



CellPress
OPEN ACCESS

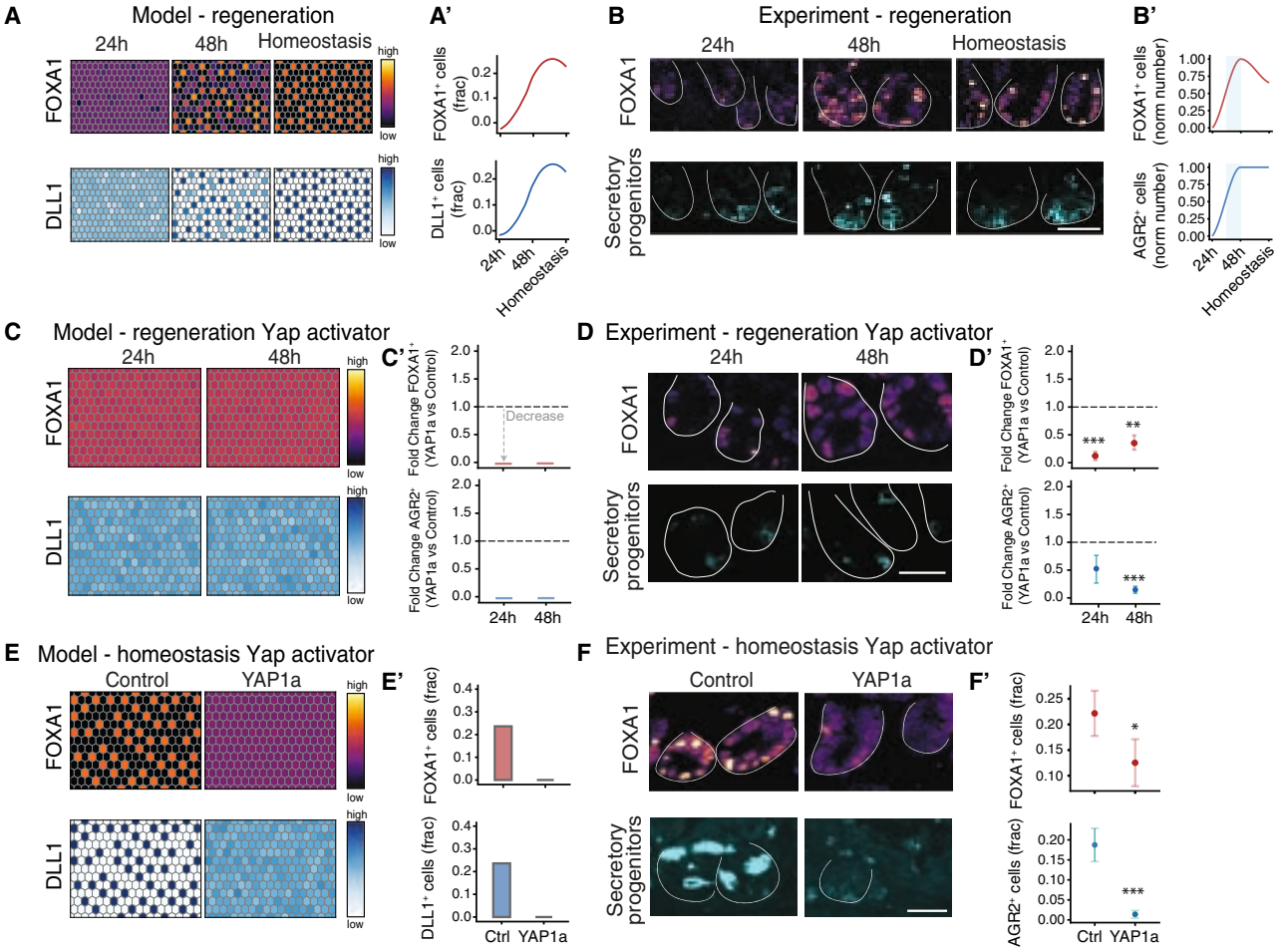


**Figure 5. Heterogeneity-driven bistability controls tissue patterning during *in vivo* regeneration**

(A) Model predictions of FOXA1 and DLL1 patterning during *in vivo* regeneration using parameters constrained from organoid experiments.

(A′) Time evolution of FOXA1$^+$ and DLL1$^+$ cell fractions ($n$ = 100 simulations; SEM negligible).

(B) MIPs of FOXA1 and AGR2 at 24 and 48 h post-irradiation (10 Gy) and at homeostasis (scale bar, 25 μm).

(B′) Temporal quantification of FOXA1$^+$ and AGR2$^+$ cell numbers (min-max scaled; $N$ = 3 mice per time point, $n$ = 9–20 crypts).

(C) Model predictions of sustained YAP1 activation during regeneration, showing reduced FOXA1 and DLL1 patterning.

(C′) Corresponding FOXA1$^+$ and DLL1$^+$ fractions ($n$ = 100 simulations; SEM negligible).

(D) MIPs of FOXA1 and AGR2 in YAP1 activator (LATSi)-treated tissue at 24 and 48 h post-injury.

(D′) Fold change in FOXA1$^+$ and AGR2$^+$ fractions relative to control ($N$ = 3 mice per time point; Vehicle: $n$ = 1,680 cells from 77 crypts; LATSi: $n$ = 1,114 cells from 53 crypts).

(E) Model predictions of acute YAP1 activation from a homeostatic state, resulting in reduced FOXA1 and DLL1 patterning.

(E′) Corresponding FOXA1$^+$ and DLL1$^+$ fractions ($n$ = 100 simulations; SEM negligible).

(F) Z-plane images of FOXA1 and AGR2 in control and YAP1-activated tissue (scale bars, 25 μm).

(F′) Quantification of FOXA1$^+$ and AGR2$^+$ fractions (mean ± SEM; $N$ = 3 mice per condition, $n$ = 14–17 crypts).

Statistical significance: *$p < 0.05$, **$p < 0.01$, and ***$p < 0.001$.

See also Figure S11.

high-gain regime of a sigmoidal relationship between mechanical cues and YAP1 activity. In this regime, small differences in local mechanical context and nuclear morphology are amplified into large differences in YAP1 activity, generating population-level heterogeneity. Outside this window, YAP1 responses are buffered and relatively insensitive to further mechanical variation. Thus, mechanical cues do not simply tune YAP1 levels—they determine when heterogeneity can emerge. At the cellular level, YAP1 activity is associated with a broad increase in chromatin accessibility, establishing a permissive, progenitor-like landscape that resets epithelial identity and reopens the potential for re-differentiation, favoring FOXA1 engagement. As YAP1 activity decreases heterogeneously, the subset of cells maintaining higher YAP1 levels preserves both the permissive chromatin state and the heightened responsiveness to DLL1-mediated lateral inhibition. In these cells, extrinsic lateral

Please cite this article in press as: Schwayer et al., Multiscale integration of tissue and chromatin context converts cell heterogeneity into stable intestinal patterning, Cell (2026), https://doi.org/10.1016/j.cell.2026.06.009



signaling reinforces FOXA1 expression, initiating secretory commitment and biasing them toward a DLL1$^{+}$ fate. Therefore, FOXA1 integrates intrinsic YAP1-driven chromatin states with extrinsic DLL1-mediated lateral inhibition, acting as a molecular switch that drives fate specification. FOXA1, in turn, establishes DLL1 bistability—a condition where high and low DLL1 expression states can coexist, with the eventual DLL1 level determined by the strength of lateral inhibition experienced during the prior YAP1$^{high}$ state.

The presence of FOXA1 effectively insulates YAP1 from the negative feedback typically imposed by lateral inhibition. By acting downstream of YAP1 and upstream of DLL1, FOXA1 allows YAP1 to indirectly promote lateral inhibition without being subject to its suppressive effects (Figures S7I–S7I″). Hence, FOXA1 enables YAP1 to act as a transient activator of patterning while preserving the robustness of the DLL1 feedback loop. This YAP1-FOXA1-DLL1 landscape describes cell fates as arising from multicellular attractors that incorporate both neighborhood interactions and intracellular states (Figures S10D and S10D′). Our model extends Waddington landscape models for cell fate decisions[17,18,63,64] to systems combining cell-cell interactions and cell state heterogeneities. Notably, while lateral inhibition-based bistability has been previously described, for example, in Drosophila bristle patterning,[18] our work shows that in the intestinal epithelium, bistability operates at low levels of lateral signaling to interpret short-range, single-cell pre-patterns, rather than long-range multicellular gradients. On a temporal scale, bistability allows cells to retain a memory of prior YAP1 activity during the regenerative process, maintaining DLL1 patterning even as YAP1 activity diminishes during homeostasis.[73,74] The predictive strength of our model, built entirely on *in vitro* data, was confirmed *in vivo*—capturing the emergence and stabilization of secretory progenitors during regeneration.

We anticipate that the heterogeneity-driven patterning framework described here extends to other epithelial systems where YAP1 and Delta-Notch signaling intersect. In human small intestinal organoids,[28] YAP1 heterogeneity emerges early during regeneration, and cells with higher YAP1 activity are preferentially associated with DLL1$^{+}$ progenitor states (Figures S11D–S11D‴). Similar relationships between elevated YAP1 activity and DLL$^{+}$ progenitors were observed in mouse colon and salivary gland epithelia (Figures S11E–S11F′). Together with recent work in bilayered mouse epithelia,[75] these observations suggest a conserved mechanochemical coupling between tissue architecture, YAP1 activity, and Notch-mediated lineage specification. Our work underscores how tissue-level properties, such as tissue density, are integrated with single-cell chromatin states and intercellular signaling to drive emergent collective behaviors, including patterning. It further identifies regulated cellular heterogeneity as a key control parameter for differentiation and tissue patterning. Through chromatin accessibility changes and fate bistability, transient heterogeneity can be mechanistically translated into long-lasting fate decisions. This mechanism may represent a fundamental principle governing tissue regeneration, enabling tissues to sense their structural integrity and functional state to then coordinate a return to homeostasis. Tumorigenesis may represent pathological fixation and spatial dysregulation of the mechanisms controlling YAP1 activity. Consistent with this view, YAP/transcriptional co-activator with PDZ-binding motif (TAZ) activation has been linked to tumor initiation, maintenance of stem-like traits, and impaired differentiation across multiple cancers.[76–78] Under this framework, dysregulated YAP1 signaling could stabilize heterogeneity-driven competence and memory modules, converting transient microenvironmental cues into persistent malignant states.

## Limitations of the study

A limitation of this study concerns the quantitative description of how YAP1 integrates mechanical and contextual inputs at the single-cell level. Although our data are consistent with a sigmoidal relationship between mechanical inputs and YAP1 activity, factors such as substrate stiffness, tissue architecture, extracellular matrix composition, culture conditions, and neighboring cell types may shift the transition, alter its steepness, or change the heterogeneity-permissive window. Our model shows that epithelial-intrinsic YAP1-FOXA1 dynamics are sufficient to establish chromatin competence and fate bistability *in vitro*, but intestinal regeneration *in vivo* occurs within a complex niche. Mesenchymal, immune, and matrix-derived signals likely influence the timing and spatial coordination of regeneration[25,79] and may stabilize, amplify, or coordinate this intrinsic epithelial pattern-forming circuit. Preservation of the mechanism *in vivo* supports a model in which epithelial regulatory modules operate within, and are reinforced by, the regenerative microenvironment. Finally, our cell-cell signaling model does not explicitly include organoid growth or cell division. Incorporating proliferation dynamics could help connect fate patterning to contexts where growth and fate specification are more tightly coupled.

## RESOURCE AVAILABILITY

### Lead contact

Further information and requests for resources and reagents should be directed to and will be fulfilled by the lead contact, Prisca Liberali (prisca.liberali@fmi.ch).

### Materials availability

New organoid lines (STAR/AGR2-KI, CTGF, FOXA1-KO, FOXA2-KO, and FOXA1-OE lines) are available through a materials transfer agreement (MTA).

### Data and code availability

- All sequencing data have been deposited at the Gene Expression Omnibus (GEO) under accession number GEO: GSE283662.
- Analysis of imaging and sequencing data was developed in the Liberali lab and is available at https://github.com/LiberaliLab/symmetry-breaking-2026. Detailed information on the packages used is provided in the STAR Methods section.
- Any additional information required to reanalyze the data reported in this paper is available from the lead contact upon request.

## ACKNOWLEDGMENTS

We thank the Liberali group, M. Verbeek, and C. Soneson for fruitful discussions; E. Tagliavini for IT support; J. Lüthi for Fractal support; H. Köhler for FACS sorting; T.O. Buchholz for help on cell segmentation; B. Treutlein and A. Xavier da Silveira dos Santos for help with library preparation of single-cell ATAC-seq; M. Garioni for help with mouse salivary organoids; M. Kahnwald for help with human intestinal organoids; M. Lütolf, M. Nikolaev, and O.

Please cite this article in press as: Schwayer et al., Multiscale integration of tissue and chromatin context converts cell heterogeneity into stable intestinal patterning, Cell (2026), https://doi.org/10.1016/j.cell.2026.06.009



Mitrofanova for providing material and initial training for microwell experiments; J. Tchorz and V. Orsini for intestinal tissue sections of the YAP1 activator experiment in homeostasis; R. Kageyama for DLL1-Venus-T2A-mCherry mice; J.-F. Spetz for technical assistance; C. Lambert and N. Accart for help with sample preparation; Claudia Flandoli for graphic design of schemes; and Zuzana Nascakova for the graphical abstract. We thank the Foundation Hubrecht Organoid Technology (now Foundation Hubrecht Organoid Biobank, https://www.hubrechtorganoidbiobank.org/) for the duodenal organoid line used in this study (HUB-04-A2-001). We thank C.P. Heisenberg, M. Lütolf, C. Tsiairis, J. Zaugg, G. D'Angelo, L. Giorgetti, S. Arber, and the Liberali group for reading the manuscript. C.S. was supported by the European Molecular Biology Organization (Postdoctoral Fellowship ALTF 660-2020) and the Human Frontier Science Program (HFSP) LT000746/2021-L. D.B.B. was supported by the NOMIS Foundation as a NOMIS fellow, an EMBO Postdoctoral Fellowship (ALTF 343-2022), and the Austrian Academy of Sciences through an APART-MINT Fellowship. B.S. was supported by the Francis Crick Institute, which receives its core funding from Cancer Research UK, the UK Medical Research Council, and the Wellcome Trust (FC001159). This work received funding from ERC to E.H. (grant number 851288) and to P.L. (grant number 758617) and from SNSF (310030_208162 and SNSF ERC TMCG-3_223263).

## AUTHOR CONTRIBUTIONS

P.L. conceived and supervised the study. C.S. initiated the project. P.L., C.S., and S.B. designed experiments and interpreted the data. D.B.B. and E.H. developed the mathematical model. D.B.B. performed simulations. C.S. and S.B. performed time-course experiments of mouse intestinal organoids. C.S. performed microwell experiments. L.C. established a 2D organoid. S.B., I.U., and L.C. performed experiments, perturbations, and laser ablation in 2D organoids. S.B. analyzed the data. C.S. trained neural networks for 3D segmentation. C.S. and S.B. developed a feature extraction pipeline for organoid and single-cell data and analyzed the mouse intestinal organoid and microwell experiments. S.B. and M.B.S. designed the single-cell image analysis and developed the Python package "ez-zarr." S.B. developed the statistical modeling and morphoaxis analysis of YAP heterogeneity. K.C.O. designed and generated the AGR2 knockin/STAR line. K.C.O. performed time-course experiments of human small intestine and mouse salivary gland organoids. C.S. performed the analysis. K.C.O. and C.S. performed and analyzed diphtheria toxin experiments. C.S. performed and analyzed mouse colon organoid experiments. C.B. and N.A.R. performed the ATAC-seq experiment. U.K. and G.C. prepared libraries and sequenced ATAC samples. S.B. and M.B.S. analyzed ATAC-seq experiments. O.E.D., B.S., J.K., and A.F. performed *in vivo* irradiation experiments. C.S. performed staining and imaging of *in vivo* samples. S.B. and C.S. analyzed *in vivo* data. S.B., C.S., and V.K. collected samples for ChIP sequencing. J.S. and M. Bühler performed ChIP sequencing. S.B. and M.B.S. analyzed the ChIP dataset. M. Bourdon designed probes and performed HCR-FISH. C.S. and K.C.O. designed the FOXA1 and FOXA2 knockout strategy. L.C.M. and I.U. generated and validated FOXA1 and FOXA2 knockout lines. S.B. and I.U. designed, generated, and validated the FOXA1 overexpression strategy. S.S. designed and cloned the CTGF reporter. Q.Y. generated the organoid line. C.S. performed light-sheet experiments. S.B. and C.S. analyzed CTGF light-sheet data. F.M. tracked single cells in DLL1 light-sheet data. P.L., E.H., D.B.B., S.B., and C.S. wrote the manuscript.

## DECLARATION OF INTERESTS

The authors declare no competing interests.

## STAR★METHODS

Detailed methods are provided in the online version of this paper and include the following:

- KEY RESOURCES TABLE
- EXPERIMENTAL MODEL AND STUDY PARTICIPANT DETAILS
  - Animal experiments and mouse intestinal organoid lines
  - Mouse intestinal organoid maintenance culture
  - Patient-derived human organoid lines
- METHOD DETAILS
  - Generation of FOXA1-KO and FOXA2-KO organoid line
  - Foxa1 qPCR analysis
  - Cloning and generation of FOXA1-OE organoid line
  - Mouse intestinal organoid regeneration time course
  - Compound treatments
  - Fixed sample preparation and antibody staining
  - High-throughput imaging of mouse intestinal organoid time course
  - Irradiation experiments
  - Sectioning, immunostaining and imaging of OCT embedded *in vivo* tissue
  - Deparaffinization and staining of YAP1 activator treated *in vivo* tissue sections
  - Live sample preparation and light sheet imaging
  - Design and construction of CTGF-mNeonGreen-NLS transcriptional reporter
  - Generation of CTGF-mNEONgreen-NLS organoid line and tracking
  - Microwell experiments
  - 2D organoid culture
  - Laser Ablation on 2D organoids
  - scATAC sequencing time course
  - Nuclei Isolation and scATAC-seq Library Preparation
  - ChIPseq sample dissociation
  - ChIPseq library preparation and sequencing
  - scRNA sequencing time course
  - Single cell isolation and scRNA-seq Library Preparation
  - HCR-FISH of Notch ligands
  - Generation of Agr2-p2a-FLAG-mStayGold-2xNLS; 8xSTAR-sTom-2xNLS organoids
  - Lineage-biased time-course experiment using AGR-STAR organoid line
  - Lineage-enrichment time-course experiment using compound treatments
  - Human intestinal organoid regeneration time course and culturing
  - Mouse Salivary Gland Organoids
  - Diphteria Toxin time-course experiment
  - Mouse colon organoid regeneration
- QUANTIFICATION AND STATISTICAL ANALYSIS
  - Lineage analysis of DLL1-P2A-mcherry line in lightsheet imaging
  - Image analysis of high-content organoid data
  - Normalised density calculation
  - Statistical modeling of YAP1 heterogeneity
  - scATACseq analysis
  - ChIPseq analysis
  - scRNAseq analysis
  - Analysis of Diphteria Toxin experiment
  - Statistical analysis

## SUPPLEMENTAL INFORMATION

Supplemental information can be found online at https://doi.org/10.1016/j.cell.2026.06.009.

Received: July 2, 2025
Revised: March 7, 2026
Accepted: June 8, 2026

## REFERENCES

1. Kondo, S., and Miura, T. (2010). Reaction-diffusion model as a framework for understanding biological pattern formation. Science *329*, 1616–1620. https://doi.org/10.1126/science.1179047.

Please cite this article in press as: Schwayer et al., Multiscale integration of tissue and chromatin context converts cell heterogeneity into stable intestinal patterning, Cell (2026), https://doi.org/10.1016/j.cell.2026.06.009



2. Green, J.B.A., and Sharpe, J. (2015). Positional information and reaction-diffusion: two big ideas in developmental biology combine. Development *142*, 1203–1211. https://doi.org/10.1242/dev.114991.

3. Nacu, E., and Tanaka, E.M. (2011). Limb regeneration: a new development? Annu. Rev. Cell Dev. Biol. *27*, 409–440. https://doi.org/10.1146/annurev-cellbio-092910-154115.

4. Rink, J.C. (2018). Stem Cells, Patterning and Regeneration in Planarians: Self-Organization at the Organismal Scale. Methods Mol. Biol. *1774*, 57–172. https://doi.org/10.1007/978-1-4939-7802-1_2.

5. Rogers, K.W., and Schier, A.F. (2011). Morphogen gradients: from generation to interpretation. Annu. Rev. Cell Dev. Biol. *27*, 377–407. https://doi.org/10.1146/annurev-cellbio-092910-154148.

6. Turing, A.M. (1952). The chemical basis of morphogenesis. Philos. Trans. R. Soc. Lond. B Biol. Sci. *237*, 37–72. https://doi.org/10.1098/rstb.1952.0012.

7. Wolpert, L. (1969). Positional information and the spatial pattern of cellular differentiation. J. Theor. Biol. *25*, 1–47. https://doi.org/10.1016/s0022-5193(69)80016-0.

8. Goodwin, B.C., and Cohen, M.H. (1969). A phase-shift model for the spatial and temporal organization of developing systems. J. Theor. Biol. *25*, 49–107. https://doi.org/10.1016/s0022-5193(69)80017-2.

9. Wolpert, L. (1989). Positional information revisited. Development *107*, 3–12. https://doi.org/10.1242/dev.107.Supplement.3.

10. Briscoe, J., and Ericson, J. (1999). The specification of neuronal identity by graded Sonic Hedgehog signalling. Semin. Cell Dev. Biol. *10*, 353–362. https://doi.org/10.1006/scdb.1999.0295.

11. Kraut, R., and Levine, M. (1991). Spatial regulation of the gap gene giant during Drosophila development. Development *111*, 601–609. https://doi.org/10.1242/dev.111.2.601.

12. Panman, L., and Zeller, R. (2003). Patterning the limb before and after SHH signalling. J. Anat. *202*, 3–12. https://doi.org/10.1046/j.1469-7580.2003.00138.x.

13. Ephrussi, A., and St Johnston, D. (2004). Seeing Is Believing: The Bicoid Morphogen Gradient Matures. Cell *116*, 143–152. https://doi.org/10.1016/S0092-8674(04)00037-6.

14. Jaeger, J., and Reinitz, J. (2006). On the dynamic nature of positional information. BioEssays *28*, 1102–1111. https://doi.org/10.1002/bies.20494.

15. Artavanis-Tsakonas, S., Rand, M.D., and Lake, R.J. (1999). Notch signaling: cell fate control and signal integration in development. Science *284*, 770–776. https://doi.org/10.1126/science.284.5415.770.

16. Collier, J.R., Monk, N.A., Maini, P.K., and Lewis, J.H. (1996). Pattern formation by lateral inhibition with feedback: a mathematical model of delta-notch intercellular signalling. J. Theor. Biol. *183*, 429–446. https://doi.org/10.1006/jtbi.1996.0233.

17. Sprinzak, D., Lakhanpal, A., Lebon, L., Santat, L.A., Fontes, M.E., Anderson, G.A., Garcia-Ojalvo, J., and Elowitz, M.B. (2010). Cis-interactions between Notch and Delta generate mutually exclusive signalling states. Nature *465*, 86–90. https://doi.org/10.1038/nature08959.

18. Corson, F., Couturier, L., Rouault, H., Mazouni, K., and Schweisguth, F. (2017). Self-organized Notch dynamics generate stereotyped sensory organ patterns in Drosophila. Science *356*, eaai7407. https://doi.org/10.1126/science.aai7407.

19. Sternberg, P.W. (1993). Falling off the knife edge. Curr. Biol. *3*, 763–765. https://doi.org/10.1016/0960-9822(93)90025-j.

20. Artavanis-Tsakonas, S., Matsuno, K., and Fortini, M.E. (1995). Notch signaling. Science *268*, 225–232. https://doi.org/10.1126/science.7716513.

21. Chitnis, A., Henrique, D., Lewis, J., Ish-Horowicz, D., and Kintner, C. (1995). Primary neurogenesis in Xenopus embryos regulated by a homologue of the Drosophila neurogenic gene Delta. Nature *375*, 761–766. https://doi.org/10.1038/375761a0.

22. Gregorieff, A., Liu, Y., Inanlou, M.R., Khomchuk, Y., and Wrana, J.L. (2015). Yap-dependent reprogramming of Lgr5(+) stem cells drives intestinal regeneration and cancer. Nature *526*, 715–718. https://doi.org/10.1038/nature15382.

23. Aloia, L., McKie, M.A., Vernaz, G., Cordero-Espinoza, L., Aleksieva, N., van den Ameele, J., Antonica, F., Font-Cunill, B., Raven, A., Aiese Cigliano, R., et al. (2019). Epigenetic remodelling licences adult cholangiocytes for organoid formation and liver regeneration. Nat. Cell Biol. *21*, 1321–1333. https://doi.org/10.1038/s41556-019-0402-6.

24. Tetteh, P.W., Basak, O., Farin, H.F., Wiebrands, K., Kretzschmar, K., Begthel, H., van den Born, M., Korving, J., de Sauvage, F., van Es, J.H., et al. (2016). Replacement of lost Lgr5-positive stem cells through plasticity of their enterocyte-lineage daughters. Cell Stem Cell *18*, 203–213. https://doi.org/10.1016/j.stem.2016.01.001.

25. Yui, S., Azzolin, L., Maimets, M., Pedersen, M.T., Fordham, R.P., Hansen, S.L., Larsen, H.L., Guiu, J., Alves, M.R.P., Rundsten, C.F., et al. (2018). YAP/TAZ-dependent reprogramming of colonic epithelium links ECM remodeling to tissue regeneration. Cell Stem Cell *22*, 35–49.e7. https://doi.org/10.1016/j.stem.2017.11.001.

26. Lukonin, I., Serra, D., Challet Meylan, L., Volkmann, K., Baaten, J., Zhao, R., Meeusen, S., Colman, K., Maurer, F., Stadler, M.B., et al. (2020). Phenotypic landscape of intestinal organoid regeneration. Nature *586*, 275–280. https://doi.org/10.1038/s41586-020-2776-9.

27. Viragova, S., Li, D., and Klein, O.D. (2024). Activation of fetal-like molecular programs during regeneration in the intestine and beyond. Cell Stem Cell *31*, 949–960. https://doi.org/10.1016/j.stem.2024.05.009.

28. Oost, K.C., Kahnwald, M., Barbiero, S., de Medeiros, G., Suppinger, S., Kalck, V., Meylan, L.C., Smallwood, S.A., Stadler, M.B., and Liberali, P. (2023). Dynamics and plasticity of stem cells in the regenerating human colonic epithelium. bioRxiv. . Preprint at. https://doi.org/10.1101/2023.12.18.572103.

29. Priya, R., Allanki, S., Gentile, A., Mansingh, S., Uribe, V., Maischein, H.-M., and Stainier, D.Y.R. (2020). Tension heterogeneity directs form and fate to pattern the myocardial wall. Nature *588*, 130–134. https://doi.org/10.1038/s41586-020-2946-9.

30. Serra, D., Mayr, U., Boni, A., Lukonin, I., Rempfler, M., Challet Meylan, L., Stadler, M.B., Strnad, P., Papasaikas, P., Vischi, D., et al. (2019). Self-organization and symmetry breaking in intestinal organoid development. Nature *569*, 66–72. https://doi.org/10.1038/s41586-019-1146-y.

31. Balaban, N.Q., Merrin, J., Chait, R., Kowalik, L., and Leibler, S. (2004). Bacterial persistence as a phenotypic switch. Science *305*, 1622–1625. https://doi.org/10.1126/science.1099390.

32. Stewart, P.S., and Franklin, M.J. (2008). Physiological heterogeneity in biofilms. Nat. Rev. Microbiol. *6*, 199–210. https://doi.org/10.1038/nrmicro1838.

33. Zinner, M., Lukonin, I., and Liberali, P. (2020). Design principles of tissue organisation: How single cells coordinate across scales. Curr. Opin. Cell Biol. *67*, 37–45. https://doi.org/10.1016/j.ceb.2020.07.004.

34. Turner, D.A., Baillie-Johnson, P., and Martinez Arias, A.M. (2016). Organoids and the genetically encoded self-assembly of embryonic stem cells. BioEssays *38*, 181–191. https://doi.org/10.1002/bies.201500111.

35. Schauer, A., Pinheiro, D., Hauschild, R., and Heisenberg, C.-P. (2020). Zebrafish embryonic explants undergo genetically encoded self-assembly. Elife *9*, e55190. https://doi.org/10.7554/eLife.55190.

36. Ji, N., Middelkoop, T.C., Mentink, R.A., Betist, M.C., Tonegawa, S., Mooijman, D., Korswagen, H.C., and van Oudenaarden, A. (2013). Feedback Control of Gene Expression Variability in the Caenorhabditis elegans Wnt Pathway. Cell *155*, 869–880. https://doi.org/10.1016/j.cell.2013.09.060.

37. Raj, A., and van Oudenaarden, A. (2008). Nature, Nurture, or Chance: Stochastic Gene Expression and Its Consequences. Cell *135*, 216–226. https://doi.org/10.1016/j.cell.2008.09.050.

Please cite this article in press as: Schwayer et al., Multiscale integration of tissue and chromatin context converts cell heterogeneity into stable intestinal patterning, Cell (2026), https://doi.org/10.1016/j.cell.2026.06.009



38. Eldar, A., and Elowitz, M.B. (2010). Functional roles for noise in genetic circuits. Nature *467*, 167–173. https://doi.org/10.1038/nature09326.

39. Chazaud, C., Yamanaka, Y., Pawson, T., and Rossant, J. (2006). Early lineage segregation between epiblast and primitive endoderm in mouse blastocysts through the Grb2-MAPK pathway. Dev. Cell *10*, 615–624. https://doi.org/10.1016/j.devcel.2006.02.020.

40. Schröter, C., Stapornwongkul, K.S., and Trivedi, V. (2023). Local cellular interactions during the self-organization of stem cells. Curr. Opin. Cell Biol. *85*, 102261. https://doi.org/10.1016/j.ceb.2023.102261.

41. Fabrèges, D., Corominas-Murtra, B., Moghe, P., Kickuth, A., Ichikawa, T., Iwatani, C., Tsukiyama, T., Daniel, N., Gering, J., Stokkermans, A., et al. (2024). Temporal variability and cell mechanics control robustness in mammalian embryogenesis. Science *386*, eadh1145. https://doi.org/10.1126/science.adh1145.

42. Mahoney, J.E., Mori, M., Szymaniak, A.D., Varelas, X., and Cardoso, W.V. (2014). The hippo pathway effector Yap controls patterning and differentiation of airway epithelial progenitors. Dev. Cell *30*, 137–150. https://doi.org/10.1016/j.devcel.2014.06.003.

43. Rocchi, C., Cinat, D., Serrano Martinez, P., Bruin, A.L.J., Baanstra, M., Brouwer, U., Del Angel Zuivre, C., Schepers, H., van Os, R., Barazzuol, L., et al. (2021). The Hippo signaling pathway effector YAP promotes salivary gland regeneration after injury. Sci. Signal. *14*, eabk0599. https://doi.org/10.1126/scisignal.abk0599.

44. Rosado-Olivieri, E.A., Anderson, K., Kenty, J.H., and Melton, D.A. (2019). YAP inhibition enhances the differentiation of functional stem cell-derived insulin-producing β cells. Nat. Commun. *10*, 1464. https://doi.org/10.1038/s41467-019-09404-6.

45. Panciera, T., Azzolin, L., Fujimura, A., Di Biagio, D., Frasson, C., Bresolin, S., Soligo, S., Basso, G., Bicciato, S., Rosato, A., et al. (2016). Induction of expandable tissue-specific stem/progenitor cells through transient expression of YAP/TAZ. Cell Stem Cell *19*, 725–737. https://doi.org/10.1016/j.stem.2016.08.009.

46. Ayyaz, A., Kumar, S., Sangiorgi, B., Ghoshal, B., Gosio, J., Ouladan, S., Fink, M., Barutcu, S., Trcka, D., Shen, J., et al. (2019). Single-cell transcriptomes of the regenerating intestine reveal a revival stem cell. Nature *569*, 121–125. https://doi.org/10.1038/s41586-019-1154-y.

47. Das, S., Parigi, S.M., Luo, X., Fransson, J., Kern, B.C., Okhovat, A., Diaz, O.E., Sorini, C., Czarnewski, P., Webb, A.T., et al. (2024). Liver X receptor unlinks intestinal regeneration and tumorigenesis. Nature *637*, 1198–1206. https://doi.org/10.1038/s41586-024-08247-6.

48. Yin, X., Farin, H.F., van Es, J.H., Clevers, H., Langer, R., and Karp, J.M. (2013). Niche-independent high-purity cultures of Lgr5+ intestinal stem cells and their progeny. Nat. Methods *11*, 106–112. https://doi.org/10.1038/nmeth.2737.

49. Oost, K.C., van Voorthuijsen, L., Fumagalli, A., Lindeboom, R.G.H., Sprangers, J., Omerzu, M., Rodriguez-Colman, M.J., Heinz, M.C., Verlaan-Klink, I., Maurice, M.M., et al. (2018). Specific labeling of stem cell activity in human colorectal organoids using an ASCL2-responsive minigene. Cell Rep. *22*, 1600–1614. https://doi.org/10.1016/j.celrep.2018.01.033.

50. Heinz, M.C., Oost, K.C., and Snippert, H.J.G. (2020). Introducing the stem cell ASCL2 reporter STAR into intestinal organoids. Star Protoc. *1*, 100126. https://doi.org/10.1016/j.xpro.2020.100126.

51. Gjorevski, N., Nikolaev, M., Brown, T.E., Mitrofanova, O., Brandenberg, N., DelRio, F.W., Yavitt, F.M., Liberali, P., Anseth, K.S., and Lutolf, M.P. (2022). Tissue geometry drives deterministic organoid patterning. Science *375*, eaaw9021. https://doi.org/10.1126/science.aaw9021.

52. Maimets, M., Nikolaev, M., Lövkvist, C., Bertillot, F., Larsen, H.L., Bressan, R.B., Georgantzoglou, A., Gjorevski, N., Filidou, E., Zøylner, M., et al. (2026). Engineered intestinal crypt geometry uncovers YAP1-dependent fetal-to-adult transition. Cell Stem Cell *33*, 487–501.e7. https://doi.org/10.1016/j.stem.2026.01.006.

53. Yang, Q., Xue, S.-L., Chan, C.J., Rempfler, M., Vischi, D., Maurer-Gutierrez, F., Hiiragi, T., Hannezo, E., and Liberali, P. (2021). Cell fate coordinates mechano-osmotic forces in intestinal crypt formation. Nat. Cell Biol. *23*, 733–744. https://doi.org/10.1038/s41556-021-00700-2.

54. Horwitz, S.B. (1994). Taxol (paclitaxel): mechanisms of action. Ann. Oncol. *5*, S3–S6.

55. Schiff, P.B., Fant, J., and Horwitz, S.B. (1979). Promotion of microtubule assembly in vitro by taxol. Nature *277*, 665–667. https://doi.org/10.1038/277665a0.

56. Meinshausen, N., and Bühlmann, P. (2010). Stability selection. J. R. Stat. Soc. B *72*, 417–473. https://doi.org/10.1111/j.1467-9868.2010.00740.x.

57. Snijder, B., Sacher, R., Rämö, P., Damm, E.-M., Liberali, P., and Pelkmans, L. (2009). Population context determines cell-to-cell variability in endocytosis and virus infection. Nature *461*, 520–523. https://doi.org/10.1038/nature08282.

58. Snijder, B., and Pelkmans, L. (2011). Origins of regulated cell-to-cell variability. Nat. Rev. Mol. Cell Biol. *12*, 119–125. https://doi.org/10.1038/nrm3044.

59. Zanconato, F., Forcato, M., Battilana, G., Azzolin, L., Quaranta, E., Bodega, B., Rosato, A., Bicciato, S., Cordenonsi, M., and Piccolo, S. (2015). Genome-wide association between YAP/TAZ/TEAD and AP-1 at enhancers drives oncogenic growth. Nat. Cell Biol. *17*, 1218–1227. https://doi.org/10.1038/ncb3216.

60. Cai, D., Feliciano, D., Dong, P., Flores, E., Gruebele, M., Porat-Shliom, N., Sukenik, S., Liu, Z., and Lippincott-Schwartz, J. (2019). Phase separation of YAP reorganizes genome topology for long-term YAP target gene expression. Nat. Cell Biol. *21*, 1578–1589. https://doi.org/10.1038/s41556-019-0433-z.

61. Singh, P.N.P., Madha, S., Leiter, A.B., and Shivdasani, R.A. (2022). Cell and chromatin transitions in intestinal stem cell regeneration. Genes Dev. *36*, 684–698. https://doi.org/10.1101/gad.349412.122.

62. Barry, E.R., Morikawa, T., Butler, B.L., Shrestha, K., de la Rosa, R., Yan, K.S., Fuchs, C.S., Magness, S.T., Smits, R., Ogino, S., et al. (2012). Restriction of intestinal stem cell expansion and the regenerative response by YAP. Nature *493*, 106–110. https://doi.org/10.1038/nature11693.

63. Jiménez, A., Cotterell, J., Munteanu, A., and Sharpe, J. (2017). A spectrum of modularity in multi-functional gene circuits. Mol. Syst. Biol. *13*, 925. https://doi.org/10.15252/msb.20167347.

64. Corson, F., and Siggia, E.D. (2012). Geometry, epistasis, and developmental patterning. Proc. Natl. Acad. Sci. USA *109*, 5568–5575. https://doi.org/10.1073/pnas.1201505109.

65. Rand, D.A., Raju, A., Sáez, M., Corson, F., and Siggia, E.D. (2021). Geometry of gene regulatory dynamics. Proc. Natl. Acad. Sci. USA *118*, e2109729118. https://doi.org/10.1073/pnas.2109729118.

66. Sáez, M., Blassberg, R., Camacho-Aguilar, E., Siggia, E.D., Rand, D.A., and Briscoe, J. (2022). Statistically derived geometrical landscapes capture principles of decision-making dynamics during cell fate transitions. Cell Syst. *13*, 12–28.e3. https://doi.org/10.1016/j.cels.2021.08.013.

67. Geling, A., Steiner, H., Willem, M., Bally-Cuif, L., and Haass, C. (2002). A gamma-secretase inhibitor blocks Notch signaling in vivo and causes a severe neurogenic phenotype in zebrafish. EMBO Rep. *3*, 688–694. https://doi.org/10.1093/embo-reports/kvf124.

68. Ye, D.Z., and Kaestner, K.H. (2009). Foxa1 and Foxa2 control the differentiation of goblet and enteroendocrine L- and D-cells in mice. Gastroenterology *137*, 2052–2062. https://doi.org/10.1053/j.gastro.2009.08.059.

69. Burtscher, I., and Lickert, H. (2009). Foxa2 regulates polarity and epithelialization in the endoderm germ layer of the mouse embryo. Development *136*, 1029–1038. https://doi.org/10.1242/dev.028415.

70. Kageyama, R., Ohtsuka, T., and Kobayashi, T. (2007). The Hes gene family: repressors and oscillators that orchestrate embryogenesis. Development *134*, 1243–1251. https://doi.org/10.1242/dev.000786.

71. Yu, W., Qiao, Y., Tang, X., Ma, L., Wang, Y., Zhang, X., Weng, W., Pan, Q., Yu, Y., Sun, F., et al. (2014). Tumor suppressor long non-coding RNA,

Please cite this article in press as: Schwayer et al., Multiscale integration of tissue and chromatin context converts cell heterogeneity into stable intestinal patterning, Cell (2026), https://doi.org/10.1016/j.cell.2026.06.009



MT1DP is negatively regulated by YAP and Runx2 to inhibit FoxA1 in liver cancer cells. Cell. Signal. *26*, 2961–2968. https://doi.org/10.1016/j.cellsig.2014.09.011.

72. Namoto, K., Baader, C., Orsini, V., Landshammer, A., Breuer, E., Dinh, K.T., Ungricht, R., Pikiolek, M., Laurent, S., Lu, B., et al. (2024). NIBR-LTSi is a selective LATS kinase inhibitor activating YAP signaling and expanding tissue stem cells in vitro and in vivo. Cell Stem Cell *31*, 554–569.e17. https://doi.org/10.1016/j.stem.2024.03.003.

73. Zhao, J., Perkins, M.L., Norstad, M., and Garcia, H.G. (2023). A bistable autoregulatory module in the developing embryo commits cells to binary expression fates. Curr. Biol. *33*, 2851–2864.e11. https://doi.org/10.1016/j.cub.2023.06.060.

74. Xiong, W., and Ferrell, J.E., Jr. (2003). A positive-feedback-based bistable "memory module" that governs a cell fate decision. Nature *426*, 460–465. https://doi.org/10.1038/nature02089.

75. Journot, R.P., Huyghe, M., Barthelemy, A., Couto-Moreira, H., Deshayes, T., Harari, L., Sumbal, J., Faraldo, M.M., Dubail, M., Fouillade, C., et al. (2025). Conserved signals control self-organization and symmetry breaking of murine bilayered epithelia during development and regeneration. Dev. Cell *60*, 2576–2593.e6. https://doi.org/10.1016/j.devcel.2025.06.007.

76. Zanconato, F., Cordenonsi, M., and Piccolo, S. (2016). YAP/TAZ at the roots of cancer. Cancer Cell *29*, 783–803. https://doi.org/10.1016/j.ccell.2016.05.005.

77. Ganesh, K., Wu, C., O'Rourke, K.P., Szeglin, B.C., Zheng, Y., Sauvé, C.G., Adileh, M., Wasserman, I., Marco, M.R., Kim, A.S., et al. (2019). A rectal cancer organoid platform to study individual responses to chemoradiation. Nat. Med. *25*, 1607–1614. https://doi.org/10.1038/s41591-019-0584-2.

78. Ganesh, K., Basnet, H., Kaygusuz, Y., Laughney, A.M., He, L., Sharma, R., O'Rourke, K.P., Reuter, V.P., Huang, Y.-H., Turkekul, M., et al. (2020). L1CAM defines the regenerative origin of metastasis-initiating cells in colorectal cancer. Nat. Cancer *1*, 28–45. https://doi.org/10.1038/s43018-019-0006-x.

79. Hageman, J.H., Heinz, M.C., Kretzschmar, K., van der Vaart, J., Clevers, H., and Snippert, H.J.G. (2020). Intestinal Regeneration: Regulation by the Microenvironment. Dev. Cell *54*, 435–446. https://doi.org/10.1016/j.devcel.2020.07.009.

80. Sato, T., Vries, R.G., Snippert, H.J., van de Wetering, M., Barker, N., Stange, D.E., van Es, J.H., Abo, A., Kujala, P., Peters, P.J., et al. (2009). Single Lgr5 stem cells build crypt-villus structures in vitro without a mesenchymal niche. Nature *459*, 262–265. https://doi.org/10.1038/nature07935.

81. Sanjana, N.E., Shalem, O., and Zhang, F. (2014). Improved vectors and genome-wide libraries for CRISPR screening. Nat. Methods *11*, 783–784. https://doi.org/10.1038/nmeth.3047.

82. Koo, B.-K., Stange, D.E., Sato, T., Karthaus, W., Farin, H.F., Huch, M., van Es, J.H., and Clevers, H. (2011). Controlled gene expression in primary Lgr5 organoid cultures. Nat. Methods *9*, 81–83. https://doi.org/10.1038/nmeth.1802.

83. Tallapragada, N.P., Cambra, H.M., Wald, T., Keough Jalbert, S., Abraham, D.M., Klein, O.D., and Klein, A.M. (2021). Inflation-collapse dynamics drive patterning and morphogenesis in intestinal organoids. Cell Stem Cell *28*, 1516–1532.e14. https://doi.org/10.1016/j.stem.2021.04.002.

84. McLean, I.W., and Nakane, P.K. (1974). Periodate-lysine-paraformaldehyde fixative. A new fixation for immunoelectron microscopy. J. Histochem. Cytochem. *22*, 1077–1083. https://doi.org/10.1177/22.12.1077.

85. de Medeiros, G., Ortiz, R., Strnad, P., Boni, A., Moos, F., Repina, N., Challet Meylan, L., Maurer, F., and Liberali, P. (2022). Multiscale light-sheet organoid imaging framework. Nat. Commun. *13*, 4864. https://doi.org/10.1038/s41467-022-32465-z.

86. Weterings, S.D.C., Eto, H., de Leede, J.-D., Giladi, A., Hoekstra, M.E., Beijk, W.F., Liefting, E.J.M., van den Anker, K.B., van Rheenen, J., van Oudenaarden, A., et al. (2024). NOTCH-driven oscillations control cell fate decisions during intestinal homeostasis. bioRxiv. . Preprint at. https://doi.org/10.1101/2024.08.26.609553.

87. Kaaij, L.J.T., Mohn, F., van der Weide, R.H., de Wit, E., and Bühler, M. (2019). The ChAHP complex counteracts chromatin looping at CTCF sites that emerged from SINE expansions in mouse. Cell *178*, 1437–1451.e14. https://doi.org/10.1016/j.cell.2019.08.007.

88. Morabito, A., Malkmus, J., Pancho, A., Zuniga, A., Zeller, R., and Sheth, R. (2023). Optimized protocol for whole-mount RNA fluorescent in situ hybridization using oxidation-mediated autofluorescence reduction on mouse embryos. Star Protoc. *4*, 102603. https://doi.org/10.1016/j.xpro.2023.102603.

89. Passaro, M., Martinovic, M., Bevilacqua, V., Hershberg, E.A., Rossetti, G., Beliveau, B.J., Bonnal, R.J.P., and Pagani, M. (2020). OligoMinerApp: a web-server application for the design of genome-scale oligonucleotide in situ hybridization probes through the flexible OligoMiner environment. Nucleic Acids Res. *48*, W332–W339. https://doi.org/10.1093/nar/gkaa251.

90. Beliveau, B.J., Kishi, J.Y., Nir, G., Sasaki, H.M., Saka, S.K., Nguyen, S.C., Wu, C.-T., and Yin, P. (2018). OligoMiner provides a rapid, flexible environment for the design of genome-scale oligonucleotide in situ hybridization probes. Proc. Natl. Acad. Sci. USA *115*, E2183–E2192. https://doi.org/10.1073/pnas.1714530115.

91. Choi, H.M.T., Schwarzkopf, M., Fornace, M.E., Acharya, A., Artavanis, G., Stegmaier, J., Cunha, A., and Pierce, N.A. (2018). Third-generation in situ hybridization chain reaction: multiplexed, quantitative, sensitive, versatile, robust. Development *145*, dev165753. https://doi.org/10.1242/dev.165753.

92. Fujii, M., Matano, M., Nanki, K., and Sato, T. (2015). Efficient genetic engineering of human intestinal organoids using electroporation. Nat. Protoc. *10*, 1474–1485. https://doi.org/10.1038/nprot.2015.088.

93. Oost, K.C., Kahnwald, M., Barbiero, S., and de Medeiros, G.Q.G. (2023). Dynamics and plasticity of stem cells in the regenerating human colonic epithelium. bioRxiv.. Preprint at.

94. Moore, J., Basurto-Lozada, D., Besson, S., Bogovic, J., Bragantini, J., Brown, E.M., Burel, J.-M., Casas Moreno, X., de Medeiros, G., Diel, E.E., et al. (2023). OME-Zarr: a cloud-optimized bioimaging file format with international community support. Histochem. Cell Biol. *160*, 223–251. https://doi.org/10.1007/s00418-023-02209-1.

95. Lüthi, J., Cerrone, L., Comparin, T., Hess, M., Hornbachner, R., Tschan, A., Glasner de Medeiros, G.Q., Repina, N.A., Cantoni, L.K., Steffen, F.D., et al. (2026). Fractal: Towards FAIR bioimage analysis at scale with OME-Zarr-native workflows. bioRxiv. . Preprint at. https://doi.org/10.64898/2026.03.05.709921.

96. Barbiero, S., Soneson, C., Liberali, P., and Stadler, M.B. (2025). ez-zarr: A Python package for easy access and visualisation of OME-Zarr filesets. J. Open Source Softw. *10*, 7882. https://doi.org/10.21105/joss.07882.

97. Ortiz, R., de Medeiros, G., Peters, A.H.F.M., Liberali, P., and Rempfler, M. (2020). RDCNet: Instance segmentation with a minimalist recurrent residual network. In Machine Learning in Medical Imaging, M. Liu, P. Yan, C. Lian, and X. Cao, eds. (Springer International Publishing), pp. 434–443. https://doi.org/10.1007/978-3-030-59861-7_44.

98. Stringer, C., Wang, T., Michaelos, M., and Pachitariu, M. (2021). Cellpose: a generalist algorithm for cellular segmentation. Nat. Methods *18*, 100–106. https://doi.org/10.1038/s41592-020-01018-x.

99. van der Walt, S., Schönberger, J.L., Nunez-Iglesias, J., Boulogne, F., Warner, J.D., Yager, N., Gouillart, E., and Yu, T.; scikit-image contributors (2014). scikit-image: image processing in Python. PeerJ *2*, e453. https://doi.org/10.7717/peerj.453.

100. Snijder, B., Sacher, R., Rämö, P., Liberali, P., Mench, K., Wolfrum, N., Burleigh, L., Scott, C.C., Verheije, M.H., Mercer, J., et al. (2012).

Please cite this article in press as: Schwayer et al., Multiscale integration of tissue and chromatin context converts cell heterogeneity into stable intestinal patterning, Cell (2026), https://doi.org/10.1016/j.cell.2026.06.009



Single-cell analysis of population context advances RNAi screening at multiple levels. Mol. Syst. Biol. *8*, 579. https://doi.org/10.1038/msb.2012.9.

101. Huber, W., Carey, V.J., Gentleman, R., Anders, S., Carlson, M., Carvalho, B.S., Bravo, H.C., Davis, S., Gatto, L., Girke, T., et al. (2015). Orchestrating high-throughput genomic analysis with Bioconductor. Nat. Methods *12*, 115–121. https://doi.org/10.1038/nmeth.3252.

102. Stuart, T., Srivastava, A., Madad, S., Lareau, C.A., and Satija, R. (2021). Single-cell chromatin state analysis with Signac. Nat. Methods *18*, 1333–1341. https://doi.org/10.1038/s41592-021-01282-5.

103. Heinz, S., Benner, C., Spann, N., Bertolino, E., Lin, Y.C., Laslo, P., Cheng, J.X., Murre, C., Singh, H., and Glass, C.K. (2010). Simple combinations of lineage-determining transcription factors prime cis-regulatory elements required for macrophage and B cell identities. Mol. Cell *38*, 576–589. https://doi.org/10.1016/j.molcel.2010.05.004.

104. Machlab, D., Burger, L., Soneson, C., Rijli, F.M., Schübeler, D., and Stadler, M.B. (2022). monaLisa: an R/Bioconductor package for identifying regulatory motifs. Bioinformatics *38*, 2624–2625. https://doi.org/10.1093/bioinformatics/btac102.

105. Gaidatzis, D., Lerch, A., Hahne, F., and Stadler, M.B. (2015). QuasR: quantification and annotation of short reads in R. Bioinformatics *31*, 1130–1132. https://doi.org/10.1093/bioinformatics/btu781.

106. Quinlan, A.R., and Hall, I.M. (2010). BEDTools: a flexible suite of utilities for comparing genomic features. Bioinformatics *26*, 841–842. https://doi.org/10.1093/bioinformatics/btq033.

107. Kent, W.J., Sugnet, C.W., Furey, T.S., Roskin, K.M., Pringle, T.H., Zahler, A.M., and Haussler, D. (2002). The human genome browser at UCSC. Genome Res. *12*, 996–1006. https://doi.org/10.1101/gr.229102.

108. Smyth, G.K. (2005). limma: Linear Models for Microarray Data. In Bioinformatics and Computational Biology Solutions Using R and Bioconductor, R. Gentleman, V.J. Carey, W. Huber, R.A. Irizarry, and S. Dudoit, eds. (Springer-Verlag), pp. 397–420. https://doi.org/10.1007/0-387-29362-0_23.

109. Patro, R., Duggal, G., Love, M.I., Irizarry, R.A., and Kingsford, C. (2017). Salmon provides fast and bias-aware quantification of transcript expression. Nat. Methods *14*, 417–419. https://doi.org/10.1038/nmeth.4197.

110. Love, M.I., Soneson, C., Hickey, P.F., Johnson, L.K., Pierce, N.T., Shepherd, L., Morgan, M., and Patro, R. (2020). Tximeta: Reference sequence checksums for provenance identification in RNA-seq. PLoS Comput. Biol. *16*, e1007664. https://doi.org/10.1371/journal.pcbi.1007664.

111. Rath, S., Sharma, R., Gupta, R., Ast, T., Chan, C., Durham, T.J., Goodman, R.P., Grabarek, Z., Haas, M.E., Hung, W.H.W., et al. (2021). MitoCarta3.0: an updated mitochondrial proteome now with sub-organelle localization and pathway annotations. Nucleic Acids Res. *49*, D1541–D1547. https://doi.org/10.1093/nar/gkaa1011.

112. McCarthy, D.J., Campbell, K.R., Lun, A.T.L., and Wills, Q.F. (2017). Scater: pre-processing, quality control, normalization and visualization of single-cell RNA-seq data in R. Bioinformatics *33*, 1179–1186. https://doi.org/10.1093/bioinformatics/btw777.

113. Lun, A.T.L., McCarthy, D.J., and Marioni, J.C. (2016). A step-by-step workflow for low-level analysis of single-cell RNA-seq data with Bioconductor. F1000Res *5*, 2122. https://doi.org/10.12688/f1000research.9501.2.

114. Hie, B., Cho, H., DeMeo, B., Bryson, B., and Berger, B. (2019). Geometric sketching compactly summarizes the single-cell transcriptomic landscape. Cell Syst. *8*, 483–493.e7. https://doi.org/10.1016/j.cels.2019.05.003.

Please cite this article in press as: Schwayer et al., Multiscale integration of tissue and chromatin context converts cell heterogeneity into stable intestinal patterning, Cell (2026), https://doi.org/10.1016/j.cell.2026.06.009



## STAR★METHODS

### KEY RESOURCES TABLE

| REAGENT or RESOURCE | SOURCE | IDENTIFIER |
|---|---|---|
| **Antibodies** | | |
| Anti-active YAP1 | Abcam | Cat# ab205270; RRID: AB_2813833 |
| XP® Anti-YAP Rabbit Monoclonal | Cell Signaling Technology | Cat# 14074; RRID: AB_2650491 |
| Anti-DLL1 | R&D Systems | Cat# AF3970; RRID: AB_2092836 |
| Anti-FOXA1 | Abcam | Cat# ab170933; RRID: AB_3065104 |
| Anti-FOXA2 [EPR4466] | Abcam | Cat# ab108422; RRID: AB_11157157 |
| Anti-FOXA3 | Abcam | Cat# ab222245; RRID: AB_3751778 |
| Anti-AGR 2 gradient | Abcam | Cat# ab209224; RRID: AB_3751779 |
| Anti-Hes1 | Cell Signaling Technology | Cat# 11988; RRID: AB_2728766 |
| Anti-Lamin A | Abcam | Cat# ab8980; RRID: AB_306909 |
| Anti-GFP | Abcam | Cat# ab5450; RRID: AB_304897 |
| Anti-Olfm4 | Cell Signaling Technology | Cat# 39141; RRID: AB_2650511 |
| Anti-DLL4 | R&D Systems | Cat# AF1389; RRID: AB_354770 |
| Anti-AldolaseB | Abcam | Cat# ab75751; RRID: AB_2226682 |
| Anti-Chromogranin A Polyclonal | Thermo Fisher Scientific | Cat#PA5-77917; RRID: AB_2735659 |
| Donkey anti-Rabbit IgG (H+L) Highly Cross-Adsorbed Secondary Antibody, Alexa Fluor Plus 488 | Thermo Fisher Scientific | Cat# A32790; RRID: AB_2866495 |
| Donkey anti-Sheep IgG (H+L) Cross-Adsorbed Secondary Antibody, Alexa Fluor 568 | Thermo Fisher Scientific | Cat# A21099; RRID: AB_10055702 |
| Alexa Fluor 488 donkey anti mouse IgG | Thermo Fisher Scientific | Cat# A-21202; RRID: AB_141607 |
| Highly Cross-Adsorbed Secondary Antibody, Alexa Fluor™ 568 | Thermo Fisher Scientific | Cat# A10037; RRID: AB_11180865) |
| Alexa Fluor 488 donkey anti goat IgG | Thermo Fisher Scientific | Cat# A-11055; RRID: AB_2534102 |
| Donkey anti-Sheep IgG (H+L) Cross-Adsorbed Secondary Antibody, Alexa Fluor™ 568 | Thermo Fisher Scientific | Cat# A-21099; AB_10055702 |
| Alexa Fluor 647 donkey anti sheep IgG | Thermo Fisher Scientific | Cat# A-21448; RRID: AB_10374882 |
| Donkey anti-Rat IgG (H+L) Highly Cross-Adsorbed Secondary Antibody, Alexa Fluor Plus 647 | Thermo Fisher Scientific | Cat# A48272; RRID: AB_2893138 |
| Multiplexing Blocker Rabbit | NanoTag Biotechnologies | Cat# K0202-50; RRID: AB_3075894 |
| anti-Rabbit IgG sdAb – FluoTag-X4 | NanoTag Biotechnologies | Cat# N2404-AF647-S; RRID: AB_3076043 |
| **Chemicals, peptides, and recombinant proteins** | | |
| DMEM/F12 + HEPES | STEMCELL Technologies | Cat# 36254 |
| GlutaMAX | Thermo Fisher Scientific | Cat# 35050038 |
| Primocin | Invivogen | Cat# ant-pm-1 |
| B27 | Thermo Fisher Scientific | Cat# 17504044 |
| NAC | Sigma-Aldrich | Cat# A7250 |
| WNT surrogate Fc | UproteinExpress | Cat# N001 |
| R-Spondin1 | Kind gift from Novartis | N/A |
| Noggin | PeproTech | Cat# AF-250-38-01M |
| Nrg1 | R&D Systems | Cat# 5898-NR-050 |
| IGF1 | R&D Systems | Cat# 291-G1-01M |
| FGF2 | R&D Systems | Cat# 233-FB-500 |
| A83-01 | Sigma-Aldrich | Cat# SML0788-5MG |
| Type I atelocollagen | ReproCELL | Cat# KKN-IPC-50 |
| IntestiCult™ Organoid Growth Medium (Mouse) | STEMCELL Technologies | Cat# 06005 |

(*Continued on next page*)

Please cite this article in press as: Schwayer et al., Multiscale integration of tissue and chromatin context converts cell heterogeneity into stable intestinal patterning, Cell (2026), https://doi.org/10.1016/j.cell.2026.06.009





*Continued*

| REAGENT or RESOURCE | SOURCE | IDENTIFIER |
|---|---|---|
| Penicillin-Streptomycin solution 100X | VWR | Cat# 392-0406 |
| Y-27632 (ROCK inhibitor) | STEMCELL Technologies | Cat# 72304 |
| CHIR99021 (GSK3B inhibitor) | STEMCELL Technologies | Cat# 72054 |
| Hygromycin B | Fisher Scientific | Cat# 10-687-010 |
| TrypLE | Life Technologies | Cat# 12604013 |
| N2 | Thermo Fisher Scientific | Cat# 17502-048 |
| N-acetylcysteine | Sigma | Cat# A7250 |
| murine EGF | R&D Systems | Cat# 2028-EG-200 |
| Matrigel | Corning | Cat# 356255 |
| LATS inhibitor | Kind gift from Novartis | N/A |
| Verteporfin | SIGMA-ALDRICH | Cat# SML0534 |
| DMSO | SIGMA-ALDRICH | Cat# 276855 |
| DAPT | Stemgent | Cat# 04-0041 |
| Prostaglandin E2 | SIGMA-ALDRICH | Cat# P0409 |
| Forskolin | TOCRIS | Cat# 1099 |
| CFTR inhibitor (CFTRi-172) | Selleck Chemicals | Cat# S7139 |
| Taxol (Paclitaxel) | Selleck Chemicals | Cat# S1150 |
| Aphidicolin (from Nigrospora sphaerica, ≥98%) | SIGMA-ALDRICH | Cat# A0781 |
| Paraformaldehyde, 16% Solution, EM Grade | Electron Microscopy Sciences | Cat# 15710 |
| Triton X-100 | SIGMA-ALDRICH | Cat# T9284 |
| Collagen type I | Bio-Connect | Cat# KKN-IAC-50 |
| Thiazovivin | Stemgent | Cat# 04-0017 |
| Valproic Acid | SIGMA-ALDRICH | Cat# 4543 |
| Sodium Bicarbonate | Alfa Aesar | Cat# J63025-AP |
| TrypLE Express | Thermo Fisher Scientific | 12-604-021 |
| PEG200 | SIGMA-ALDRICH | Cat# P3015 |
| 50% formamide | SIGMA-ALDRICH | Cat# #4610 |
| 5% hydrogen peroxide | SIGMA-ALDRICH | Cat# H1009 |
| IWP-2 2 μM (Porcupine Inhibitor) | STEMCELL Technologies | Cat # 72124 |
| Trypsin-EDTA | Gibco | Cat# 11580626 |
| Trypsin-inhibitor | Thermo Fisher Scientific | Cat# 17075029 |
| Diphteria toxin | SIGMA-ALDRICH | Cat# D0564 |
| Polybrene | SIGMA-ALDRICH | Cat# TR-1003-G |
| **Critical commercial assays** | | |
| Qiagen RNAeasy mini kit | Qiagen | Cat# 74104 |
| PrimeScript RT Master Mix | Takara | Cat# RR036A |
| Qiaquick gel extraction kit | Qiagen | Cat# 28706 |
| Mix & Go E. Coli transformation kit | Zymo Research | Cat# T3001 |
| QIAprep Spin Miniprep Kit | Qiagen | Cat# 27106 |
| NucleoBond Xtra Midi kit | Macherey-Nagel | Cat# 740410.50 |
| Chromium Single Cell ATAC Library & Gel Bead Kit | 10x Genomics | PN-1000110 |
| NEBNext Ultra II DNA Library Prep Kit for Illumina | New England Biolabs | E7645 |
| Chromium Single Cell 3′ Library & Gel Bead Kit v2 | 10x Genomics | PN-120237 |
| **Deposited data** | | |
| scATACseq, ChIPseq and scRNAseq | This paper | GEO: GSE283662 |
| **Experimental models: Cell lines** | | |
| FOXA1-KO organoid line | This paper | N/A |
| FOXA2-KO organoid line | This paper | N/A |
| FOXA1-OE organoid line | This paper | N/A |

(*Continued on next page*)

*Continued*

| REAGENT or RESOURCE | SOURCE | IDENTIFIER |
|---|---|---|
| CTGF-mNEON-NLS organoid line | This paper | N/A |
| Agr2-p2a-FLAG-mStayGold-2xNLS; 8xSTAR-sTom-2xNLS organoid line | This paper | N/A |
| HEK293-T LentiX cells | Takara Bio | Cat# Z2180N |
| **Experimental models: Organisms/strains** | | |
| C57BL/6 wildtype mouse for organoid generation | Charles River Laboratories | N/A |
| Cas9 mouse strain B6;129S4-Gt(ROSA)26Sortm1 (rtTA*M2)Jae Col1a1tm1(tetO-cas9)Sho/J (KH2/iCas9) for organoid generation | JAX | RRID: IMSR_JAX:029415 |
| Lgr5::DTR-EGFP for organoid generation | Genentech, deSauvage laboratory | N/A |
| **Oligonucleotides** | | |
| See Table S5 | | N/A |
| **Recombinant DNA** | | |
| 8xSTAR-sTom-2xNLS construct | Heinz et al.[50] | RRID: Addgene_136261 |
| pLV 4xSTAR-mNEONGreen-NLS-blast | Heinz et al.[50] | RRID: Addgene_136258 |
| pMDG.2 | pMD2.G was a gift from Didier Trono | RRID: Addgene_12259 |
| psPAX2 | psPAX2 was a gift from Didier Trono | RRID: Addgene_12260 |
| lentiCRISPRv2 | Sanjana et al.[81] | RRID: Addgene_52961 |
| **Software and algorithms** | | |
| Custom data analysis code | This work | Github: https://github.com/LiberaliLab/symmetry-breaking-2026; Zenodo: 10.5281/zenodo.20445477 |
| Fractal platform | Lüthi et al.[95] | https://fractal-analytics-platform.github.io/ |
| 'ez-zarr' | Barbiero et al.[96] | https://fmicompbio.github.io/ez_zarr/ |
| RDCNet (version v0.4) | Ortiz et al.[97] | https://github.com/fmi-basel/RDCNet |
| Cellpose | Stringer et al.[98] | https://github.com/MouseLand/cellpose |

## EXPERIMENTAL MODEL AND STUDY PARTICIPANT DETAILS

### Animal experiments and mouse intestinal organoid lines

All mice used in this study were confirmed healthy at the time of experimentation, with no clinical signs of illness or immune compromise. Animals were naive to prior experimental procedures and had not received any drugs, treatments, or test substances before enrollment in the current study. For irradiation experiments, wild-type C57BL/6J mice were bred and maintained in individually ventilated cages at the Francis Crick Institute Biological Research Facility under specific pathogen-free conditions or maintained in a conventional animal facility and health-monitored according to institutional guidelines at University of California Berkeley. Male C57BL/6J mice (Jackson Labs, Stock No. 000664) were purchased at six weeks of age and utilized between seven and eight weeks of age. Animals were housed in a temperature-controlled environment (21°C) with a relative humidity of 30–70% under a 12-hour light/dark cycle, with ad libitum access to standard rodent chow and water. Mouse experiments were performed according to the guidelines detailed in the Project Licence granted by the UK Home Office to Brigitta Stockinger (PP0858308) or approved by the Institutional Animal Care and Use Committee (IACUC) at the University of California, Berkeley. All other animal experiments were approved by the Basel Cantonal Veterinary Authorities and performed in accordance with the Guide for Care and Use of Laboratory Animals. For mouse intestinal organoid generation, male wild-type C57BL/6 SOPF mouse line between 8 and 12 weeks old was used (Charles River Laboratories and Jackson Labs).

### Mouse intestinal organoid maintenance culture

Organoids were generated from isolated crypts of mice, as previously described.[80] In brief, the first part of the small intestine, the Duodenum, was cut open longitudinally, flushed with cold PBS and villi were removed using a cold glass slide. Tissue was cut into fragments and incubated in 2.5 mM EDTA/PBS at 4°C for 30min under shaking. Tissue was transferred into cold PBS and shaken

Please cite this article in press as: Schwayer et al., Multiscale integration of tissue and chromatin context converts cell heterogeneity into stable intestinal patterning, Cell (2026), https://doi.org/10.1016/j.cell.2026.06.009



vigorously, and supernatant was collected. The procedure was repeated two more times, to collect in total three fractions. Each fraction was centrifuged at 300xg for 5 min at 4°C. Pellets were collected in 5ml DMEM/F12/Hepes (STEMCELL), 1× Glutamax (Thermo Scientific), and 100μg/ml Penicillin-Streptomycin and centrifuged at 300xg for 5min at 4°C. After removing the supernatant, the pellet was resuspended in IntestiCult Organoid Growth Medium (STEMCELL Technologies) with 100 μg/ml Penicillin-Streptomycin, 10μM ROCK inhibitor. After that maintenance of organoid cultures was performed in IntestiCult Organoid Growth Medium (STEMCELL Technologies) with 100μg/ml Penicillin-Streptomycin.

### Patient-derived human organoid lines

Tissue material was originally obtained from patients included in HUB-Cancer protocol (12-093). Patient samples are collected with freely given, specific, informed and unambiguous consent and ethics approval for organoid derivation and data collection (Biobanks Review Committee, UMC Utrecht, sub-bank numbers 12/093). The used organoid line in this human study was provided by the Foundation Hubrecht Organoid Technology (now Foundation Hubrecht Organoid Biobank) (https://www.hubrechtorganoidbiobank.org/). The image based time courses on regenerating organoids were performed with line: HUB-04-A2-001 (human small intestine, Female, 69 years old).

## METHOD DETAILS

### Generation of FOXA1-KO and FOXA2-KO organoid line

For the CRISPR-Cas9 mediated knockout of FOXA1 and FOXA2, 20bp long guide sequences were designed using the online CHOPCHOP tool (https://chopchop.cbu.uib.no) and cloned into the lentiCRISPRv2 backbone (Addgene plasmid #52961) using the protocol described previously.[81] Briefly, vectors were digested using BsmBI and used for ligation with the phosphorylated sgRNA oligos (Table S5). Lentiviral particles were produced in HEK293-T LentiX cells (Takara Bio Cat: Z2180N Lot: AN60006S) using a 2nd generation lentiviral system (pMDG.2, Addgene plasmid #12259, and psPAX2, Addgene plasmid #12260) and the plasmid described above. Supernatant from producing cells was concentrated using Amicon Ultra-15, 100 kDa centrifugation columns (Merck Millipore, cat# UFC910024) and used for lentiviral infection as described previously.[82] In brief, 4 wells of a 24-well plate of organoids were used per infection reaction. Organoids were collected and digested at 37°C for 8 min. After washing with DMEM, cells were resuspended in 400 μl infection medium (Intesticult, 15-20% Wnt3a-CM, 10μM Y-27632 ROCK inhibitor, 3 μM CHIR, 10 μl Polybrene 10ug/ml). 100 μl of lentivirus concentrate was added and spinoculated for 1h at 32°C at 500xg. Tubes were then placed in the incubator for 5-7h at 37°C. Cell suspension was washed once with DMEM and resuspended in infection medium without Polybrene and matrigel. After 20-30 min, infection medium without Polybrene was added. FOXA1-KO mutants were generated by double-infection with gRNA#15 and gRNA#18. For FOXA2-KO mutants, three different clones were generated: clone1: gRNA#3 and #4, clone2: gRNA #4 and #5, clone3: gRNA #6 and #3. Generated organoids were passaged once before selecting with 1μg/ml Puromycin over the course of 2 passages. After selection, organoid culture was performed as described above.

### Foxa1 qPCR analysis

RNA was extracted from 2 wells of a 24-well plate of organoids using the Qiagen RNAeasy mini kit (Qiagen cat# 74104) according to the manufacturer's instructions. RNA was quantified using a Nanodrop One (ThermoFisher Scientific), and 2 μg of total RNA was reverse transcribed into cDNA using the PrimeScript RT Master Mix (Takara #RR036A) following the manufacturer's instructions. RT-PCR was performed on a StepOne real-time PCR system (ThermoFisher Scientific) using Sybr Green (ThermoFisher Scientific #A25742) and the primers listed in Table S5 (hexabiogen.com). The comparative CT (ddCT) method was used to determine the relative expression of the target gene compared to the housekeeping gene Elongation factor 1 alpha (EF1α).

### Cloning and generation of FOXA1-OE organoid line

To generate a stable FOXA1 overexpression (FOXA1-OE) line in mouse small intestinal organoids, the mouse *Foxa1* coding sequence was synthesized de novo (Twist Bioscience) and cloned into a PiggyBac transposon backbone enabling stable genomic integration. The construct consisted of the *Foxa1* open reading frame driven by the constitutive EF1α promoter, together with a PGK-driven hygromycin resistance cassette for antibiotic selection. The transgene cassette was flanked by PiggyBac inverted terminal repeats (ITRs) to allow transposase-mediated integration into genomic TTAA sites. Following assembly, the final plasmid was validated by full plasmid sequencing to confirm correct integration and sequence integrity. For stable genomic integration, organoids were co-electroporated with the PiggyBac donor plasmid and a helper plasmid encoding the PiggyBac transposase at a 2:1 mass ratio. Electroporation was performed in ENR medium lacking antibiotics as reported before.[30] Briefly, organoids were digested into single cells and resuspended in BTX electroporation solution (cat# 732-1285). 7 ug of reporter constructs and 3 ug of pBase constructs were added to 1x $10^6$ single cells with a total volume of 100μl and placed on ice. Cell-plasmid mixture was added to cuvette, and the cuvette's impedance was confirmed within the range of 0.030 to 0.05 before electroporation. Following electroporation, 400μl of BTX electroporation solution was applied to dilute and transfer the electroporation mixture, which was then incubated at room temperature for 30min and centrifuged at 300xg for 3 minutes at 4°C. After centrifugation, the supernatant was removed, and the remaining cells with 50μl of buffer was mixed with Matrigel (Corning) and seeded on 24-well plates. 500μl of ENR medium with WNT3a conditional medium, ROCKi and CHIR was added to each well. After 5-day culture at 37°C in a CO2 incubator, organoids were returned to

Please cite this article in press as: Schwayer et al., Multiscale integration of tissue and chromatin context converts cell heterogeneity into stable intestinal patterning, Cell (2026), https://doi.org/10.1016/j.cell.2026.06.009



standard ENR conditions and expanded prior to selection. Antibiotic selection was initiated right after the first passage (6-days post-electroporation) using 300 μg/mL hygromycin B, a concentration determined by prior kill-curve analysis to reliably eliminate non-transfected organoids. Selection was maintained for at least 7 days, during which non-transfected organoids died, while hygromycin-resistant organoids remained viable and expanded. To ensure robustness and reproducibility, FOXA1-OE organoids were generated from three independent electroporations performed on three separate organoid batches. Stable lines were maintained under standard ENR culture conditions and used for downstream experiments.

### Mouse intestinal organoid regeneration time course

Organoids were collected in cold DMEM/F-12 with 15 mM HEPES (Stem Cell Technologies) supplemented with 100 μg/ml Penicillin–Streptomycin, 1× Glutamax (Thermo Scientific) between 3-5 days after passaging and digested with TrypLE (Life Technologies, #12604013) for 20min at 37°C. Dissociated cells were collected and passed through a 30μm cell strainer (Sysmex). Single cells were sorted by FACS (cell sorters: Becton Dickinson Influx with software version 1.2.0.142 or BD FACS Diva with software version 8.0.1 or SONY MA9000 with software version 3.2.0 were used). Forward and side scatter were used to remove cell doublets and debris. Sorted cells were collected in ENR medium composed of advanced DMEM/F-12 with 15mM HEPES (STEM CELL Technologies) supplemented with 100 μg/ml Penicillin-Streptomycin, 1×Glutamax (Thermo Fisher Scientific), 1×B27 (Thermo Fisher Scientific), 1xN2 (Thermo Fisher Scientific), 1mM N-acetylcysteine (Sigma), 500ng/ml R-Spondin (kind gift from Novartis), 100 ng/ml Noggin (PeproTech) and 100 ng/ml murine EGF (R&D Systems) plus Y-27632 (ROCK inhibitor, STEMCELL Technologies). After spinning down single cells at 900xg, the pellet was resuspended in 60% ENR medium + Y-27632 and 40% Matrigel (Corning). 5ul droplets with 3,000 cells were seeded per well of a 96-well plate (Greiner, 655090). After 20min of solidification at 37°C, 100μl of medium was added per well. From 0h to 24h, Day0 medium was used: ENR was supplemented with 15-20% Wnt3a-conditioned medium (Wnt3a-CM), 3μM of CHIR99021 (GSK3B inhibitor, STEMCELL Technologies, cat# 72054) and 10μM Y-27632 (ROCK inhibitor, STEMCELL Technologies). From 24h-72h, Day1 medium was used: ENR was supplemented with 15-20% Wnt3a-conditioned medium (Wnt3a-CM) and 10μM Y-27632 (ROCK inhibitor, STEMCELL Technologies). From 72h till 120h only ENR medium was added. Wnt3a-conditioned medium was produced in-house by Wnt3a L-cells (kind gift from Novartis).

### Compound treatments

Single-cells were plated in 5ul droplets of 40% Matrigel (Corning) and 60% ENR + 10μM ROCK inhibitor, into a 96-well plate. For YAP1 perturbation experiments, 5μM LATS inhibitor[72] was added from 0h onwards and 5μM Verteporfin (SIGMA-ALDRICH, cat# SML0534) was added from 36h and DMSO (SIGMA-ALDRICH, cat# 276855) was used as a control. For Notch inhibition experiments, 10μM DAPT (Stemgent cat# 04-0041) was used from 0h onwards. To induce lumen inflation and nuclear stretch, 0.5μM Prostaglandin E2 (PGE)[53] or 10μM Forskolin[83] was added from 24h onwards. For rescue experiments, 100 μM CFTR inhibitor (CFTRi-172 cat# S7139) was co-administered from 24 h to block CFTR-dependent fluid secretion, and organoids were fixed at 48 h. Quantifications were normalized to the corresponding CFTR− or CFTR+ control conditions. To inhibit cell division and induce a lower density state, 5-10nM Taxol (Paclitaxel, Selleck Chemicals, cat# S1150) or 250nM Aphidicolin (from Nigrospora sphaerica, ≥98%, SIGMA-ALDRICH, cat# A0781) was used from 24h-72h. For the washout condition, organoids were treated from 24h-48h and exchanged with Day1 medium from 48h-72h.

### Fixed sample preparation and antibody staining

One 96-well plate per time point was prepared and the entire plate was fixed as follows: Plate was centrifuged at 900xg for 10min at 10°C; 4% PFA (Electron Microscopy Sciences) in PBS was added and organoids were fixed for 45min at room temperature. Plate was washed three times with PBS and sealed with Aluminium foil for storage at 4°C or further processed for antibody staining. Here, organoids were permeabilized with 0.5% Triton X-100 (SIGMA-ALDRICH) for 1h and blocked for 1h with 3% Normal Donkey Serum (SIGMA-ALDRICH) in PBS containing 0.1% Triton X-100 at room temperature. Primary antibody stainings were performed overnight at 4°C shaking and secondary antibody staining was performed for 2h at room temperature shaking and sample was washed three times with PBS. For AGR2 antibody stainings, nanobodies were used as following: after permeabilisation and blocking procedure, sample was incubated in multiplexing blocker solution (1:1.5 stoichiometric to AGR2 antibody) for 1h at room temperature; nanobody pre-complex of AGR2 antibody and anti-Rabbit IgG sdAb - FluoTag-X4 (1:1.5 stoichiometric to AGR2 antibody) in PBS was incubated for 1h in the dark at room temperature; after incubation period, pre-complex was diluted in blocking solution without multiplexing blocker solution and added to the sample for a 2h incubation period at room temperature. Samples were washed three times in PBS. Concentrations of antibodies were used as following: Anti-active YAP1 (1:200, Abcam, ab205270), XP® Anti-YAP Rabbit Monoclonal (1:200, CST, #14074), Anti-DLL1 (1:100, R&D Systems, #AF3970), Anti-FOXA1 (1:200, Abcam, ab170933), Anti-FOXA2 (1:200, Abcam, ab108422), Anti-FOXA3 (1:100, Abcam, ab222245), Anti-AGR 2 gradient (1:500, Abcam, ab209224), Anti-Hes1 (1:200, CST, #11988), Anti-Lamin A (1:100, Abcam, ab8980), Anti-GFP (1:500, Abcam, ab5450), Anti-Olfm4 (1:100, CST, #39141), Anti-DLL4 (1:100, R&D Systems, AF39141), Anti-AldolaseB (1:300, Abcam, #ab75751), Anti-Chromogranin A Polyclonal (1:500, Thermo Fisher Scientific, #PA5-77917). All secondary antibodies were used at a concentration of 1:500. Nuclei staining was performed using 100μg/ml DAPI (4',6-Diamidino-2-Phenylindole, Invitrogen) along with the secondary antibody staining.

Please cite this article in press as: Schwayer et al., Multiscale integration of tissue and chromatin context converts cell heterogeneity into stable intestinal patterning, Cell (2026), https://doi.org/10.1016/j.cell.2026.06.009



### High-throughput imaging of mouse intestinal organoid time course

High-throughput imaging was performed on a Yokogawa (CellVoyager 7000S), an automated spinning disk microscope equipped with CSU-W1 Confocal Scanner Unit (Yokogawa) with a 50μm pinhole disk unit, 2 sCMOS cameras (Andor Neo5.5, 2,560 × 2,160 pixels) and a 100mW 405nm Cube Laser, 200mW Laser 488nm Saphire Laser, 200nW Saphire Laser 561nm, 100mW 640nm Cube Laser (all from Coherent) using a 40x/0.95 UPLSAPOx2 (Olympus) Objective, or on a Yokogawa (CellVoyager 8000) equipped with CSU-W1 Confocal Scanner Unit (Yokogawa) with a 50μm pinhole disk unit, 2 sCMOS cameras (Hamamatsu Orca Flash 4 version 3, 2,048 × 2,048 pixels), and 100mW 405nm laser, 150mW Laser 488nm, 200mW Laser 561nm, 100mW 640nm Laser (all Lasers are Obis lasers from Coherent) using a 20x/1.0 water immersion Objective (Yokogawa). For imaging, either a fixed area was imaged or an intelligent imaging approach (Search First module of Wako software) was used, where the entire well was scanned with 4x and organoids were segmented and in the next step only fields that contained organoids were imaged with 40x. Z-stacks were acquired at 1-2μm z-step and ranged from 26μm for small organoids to 80μm for big organoids.

### Irradiation experiments

7-8 weeks old C57BL/6J male mice were lethally irradiated with 10 Gy[46,47] from a GSR D1 $^{137}$Caesium source irradiator (2 x 5 Gy doses with 3h rest between exposures). Mice were injected i.v. with 2.5 x $10^6$ bone marrow cells from C57BL/6J WT male mice in a volume of 0.2ml 24h after irradiation. At the indicated time points, the small intestine was divided in 3 sections of equal length and fixed in periodate-lysine-4% paraformaldehyde (PLP) buffer[84] overnight at 4°C. Tissues were washed twice with PBS and incubated in 30% sucrose overnight at 4°C. Each section was then rolled in a proximal to distal fashion, embedded in OCT and stored at -80 °C. Where indicated, mice were treated with LATSi[72] at a dose of 100 mg/kg. The first dose was administered immediately prior to irradiation. Treatment was continued every 12 hours for a total of five doses.

### Sectioning, immunostaining and imaging of OCT embedded *in vivo* tissue

OCT block was cut into 20μm thick section using Histology Cryostat CryoStar NX70 and Ultra Microtome Blades (Thermo Scientific, #30-538-35). Sections were placed onto Superfrost; Excell; Microscope Slides (Epredia, #10149870) and processed for antibody staining. First, sections were carefully washed 3x with PBS and incubated in permeabilisation and blocking solution (3% Normal Donkey Serum (SIGMA-ALDRICH) in PBS containing 0.5% Triton X-100) for 1h at room temperature. Antibody staining was performed as mentioned above (*section: Fixed sample preparation and antibody staining*). After antibody staining, sections were closed with Mounting medium (Ibidi, #50001) and a cover slip (Corning® 24x50 mm Rectangular #1½ Cover Glass, #CLS2980245-1000EA). Imaging was performed on an upright microscope Axio Imager M2 (Zeiss) equipped with CSU-W1 Confocal Scanner Unit (Yokogawa) with a 50um pinhole disk unit, a sCMOS cameras (PCO.edge 4.2M, PCO), an MS-2000 motorized stage (Applied Scientific Instrumentation) and controlled with VisiView 6.0 imaging software (Visitron Systems GmbH). Illumination was achieved with 405, 488, 561 and 639 lasers and VS-Homogenizer (Visitron Systems GmbH). A Fluar 5x/0.25 Air objective was used for acquiring overviews of the entire swiss roll and a 40x/1.3Oil objective (EC Plan Neofluar, Zeiss) was used to acquire ROIs as tiles. Z-stacks of around 20-40μm were acquired at a z-step of 1μm.

### Deparaffinization and staining of YAP1 activator treated *in vivo* tissue sections

Paraffin sections of YAP1 or vehicle treated samples were a kind gift of the Tchorz group.[72] Details on animal maintenance, and *in vivo* treatments can be found here.[72] In brief, C57BL/6 male mice (12-weeks-old) were treated with NIBR-LTSi (100mg/kg) or vehicle (0.5% methylcellulose (MC), 0.5% Tween 80) for 2.5 days and animals were sacrificed 4h after treatment, tissue was fixed in formalin and embedded as Swiss rolls in paraffin. Paraffin block was cut in 5μm sections. For AGR2 staining, Paraffin sections were treated as following: Samples were heated for 45min at 60°C. Slides were cooled down for 10min and incubated 2x for 3min in 100% EtOH, for 2min in 95% EtOH, for 3min in 75% EtOH, and for 5min in ddH2O. Sodium citrate buffer was added and heated for 50min at 90°C. After cooling down the slides, slides were transferred in ddH2O, and antibody staining was performed as above (OCT sections). For FOXA1 staining, Paraffin sections were treated as following: Sections were incubated 2x 5min in Xylol (Histograde, Biosystems) at RT and incubated 2x for 3min in 100% EtOH, for 2min in 95% EtOH, for 3min in 75% EtOH, and for 5min in ddH2O. Antigen retrieval was performed for 30 min at 95 degrees in Reveal Decloaker RTU BIOCARE MEDICAL, pH6. Antibody staining was performed as above (OCT sections).

### Live sample preparation and light sheet imaging

Organoids were collected in cold DMEM/F-12 with 15 mM HEPES (Stem Cell Technologies) supplemented with 100 μg/ml Penicillin–Streptomycin, 1× Glutamax (Thermo Scientific) between 3-5 days after passaging and digested with TrypLE (Life Technologies, #12604013) for 20min at 37°C. Dissociated cells were collected and passed through a 30μm cell strainer (Sysmex). Samples were mounted as previously described.[30,85] In brief, a custom designed and 3D printed imaging chamber was used. A 25 μm thin FEP foil (Katco) was plasma treated and then placed into the imaging chamber and glued with biocompatible silicone to the bottom of the chamber (Silpuran 4200; Wacker) and cured overnight at room temperature. Chamber was washed with EtOH and ddH2O for 3x times. Chamber was UV sterilized for 20min and pre-warmed before 5 μl droplets of single-cell suspension in 60% Matrigel (Corning) was added. After 15min, droplets solidified and Day0 medium was added. The LS1-Live dual illumination and inverted detection microscope from Viventis Microscopy Sàrl was used to perform light sheet imaging. At 24h post plating, organoids at the 2- or 4-cell

Please cite this article in press as: Schwayer et al., Multiscale integration of tissue and chromatin context converts cell heterogeneity into stable intestinal patterning, Cell (2026), https://doi.org/10.1016/j.cell.2026.06.009



stage were selected. A volume of 150 μm and Z-spacing of 2μm was acquired. Medium was refreshed every 24h according to time-course medium changes (*section: Mouse intestinal organoid regeneration time course*).

### Design and construction of CTGF-mNeonGreen-NLS transcriptional reporter

The YAP1 transcriptional target Ctgf (Ccn2) was selected as a proxy for YAP1 activity. Using a combination of the Eukaryotic Promoter Database (Swiss Institute of Bioinformatics, https://epd.expasy.org/epd/) as well as the ChIP-Atlas (https://chip-atlas.org/) a relevant Ccn2 promoter sequence was defined taking the following DNA binding transcription factors into account: Tead1, Tead2, Tead3, Tead4, Smad2, Smad3 and Smad4. For the Search Motif Tool (EPD) a cut-off p-value of 1E-03 was used. Employing the ChIP-Atlas peak browser, peaks were assessed without a cell type class selection. A MACS2 significance threshold of Q value < 1E-05 was considered. Eventually a 1074bp long sequence was selected mapping to chr10:24,594,651-24,595,725 (GRCm38/mm10).

The above-described sequence was ordered as gBlock (IDT). Due to high sequence complexity 4 repetitive bases have been deleted (see sequence below). To generate a stable reporter-line the PiggyBac transposon system was used. To that end a pPB-CAG-DEST-pA-pgk-hph vector (kind gift from J. Betschinger, Novartis) was subcloned to introduce a single MluI cloning site. To do so, the initial backbone was linearized with XbaI (cat# R0145T, NEB) and BbsI (cat#R0539S, NEB) and a gBlock (IDT) was used to introduce the MluI cut site via Gibson assembly (cat# E2611L, NEB). Using MluI (cat# R3198S, NEB) the expression vector was linearised, and Gibson assembly was used to incorporate the mNeonGreen-NLS coding sequence, amplified via PCR from pLV 4xSTAR-mNeonGreen-NLS-blast (Addgene #136258). In a subsequent cloning step this construct was cut with AccI (cat# R0161S) and XcmI (cat# R0533S) to remove the CAG promoter. A gBlock was used to retain parts of the mNeonGreen protein coding sequence as well as to introduce the above described Ctgf promoter sequence.

The Qiaquick gel extraction kit (cat# 28706, Qiagen) was used to purify PCR and digestion products from agarose gels. Mix & Go E. Coli transformation kit (cat# T3001, Zymo Research) treated DH5alpha cells (cat# 18265-017, Invitrogen) were used for transformation and plasmid amplification. Bacterial selection was performed using Ampicillin (100μ/ml). Plasmid purification was performed using QIAprep Spin Miniprep Kit (cat# 27106, Qiagen) and NucleoBond Xtra Midi kit (cat# 740410.50, Macherey-Nagel).

#### *Ctgf promoter sequence*

CCCAACTGAACCCCTACTGGCCTCCTTATACCTCTTTCTTCTCCCACTATATTCCCTGACACTTAGCTTCTGAACACAGCCATTTGG
TCTGAACTCATAAACTTATTTTTCTAGAAAAGCCATGCCCAGTCATTCCCCTTGCCTCCCTGGACCCTGAAGACAAGTTCTTACATA
AAGAGTGCTGAAAATCTCCCTGGGAACCTACATCCTTGGCTTTCATATCTTTCAGCCATCAAAATGGTTATCTCCAGTGACCAAAG
ATCAAATGCCTGTATTTCAGATACAAAAGTTGCACATAGGAATTCTGGGAGGAGAGGAGGCATTTCAAATGGCTATAAGCACCCT
TCTCCTCTCAGTAGAAGAACACCAAGAGACTACAGCCCCGTAAAGAAAAAAAAAAATCCAAAACAAAGAAAAATATTTTTTTTAATTT
CTAGGGGCCCATGGTATTTGCCTCTTGAGCTATTTGAGTCTTGAGAAGTTTTTATGTCAGTAGCCAGAACTGGCAAAGAGATTTTTA
AGAAGAAAAGATCAGAGAAATAATCGTTTATTTCTAAGTTATATTTCATCAGGAGGGGTGAGAAGATGATATGGAGAAAGTTTTACTT
CTTGGTGTTGTGCTGGAAACACAGCGCCTTTTTTTTCCTGGCGAGCTAAAGTGTGCCAGCTTTTTCAGACGGAGGAATGTGGAGT
GTCAAGGGGTCAGGATCAATCCGGTGTGAGTTGATGAGGCAGGAAGGTGGGGAGGAATGTGAGGAATGTCCCTGTTTGTGTAG
GACTCCATTCAGTTCTTTGGCGAGCCGGCTCCCGGGAGCGTATAAAAGCCAGCGCCGCCCGCCTAGTCTCACACAGCTCTTCT
CTCCAAGAAGACTCAGCCAGATCCACTCCAGCTCCGACCCCAGGAGACCGACCTCCTCCAGACGGCAGCAGCCCCAGCCCAGC
CGACAACCCCAGACGCCACCGCCTGGAGCGTCCAGACACCAACCTCCGCCCCTGTCCGAATCCAGGCTCCGGCCGCGCCTCT
CGTCGCCTCTGCACCCTGCTGTGCATCCTCCTACCGCGTCCCGATC

### Generation of CTGF-mNEONgreen-NLS organoid line and tracking

CTGF-mNEONgreen-NLS reporter line was generated via electroporation as reported before.[30] Briefly, organoids were digested into single cells and resuspended in BTX electroporation solution (cat# 732-1285). 7 ug of reporter constructs and 3 ug of pBase constructs were added to 1x $10^6$ single cells with a total volume of 100μl and placed on ice. Cell-plasmid mixture was added to cuvette, and the cuvette's impedance was confirmed within the range of 0.030 to 0.05 before electroporation. Following electroporation, 400μl of BTX electroporation solution was applied to dilute and transfer the electroporation mixture, which was then incubated at room temperature for 30min and centrifuged at 300xg for 3 minutes at 4°C. After centrifugation, the supernatant was removed, and the remaining cells with 50μl of buffer was mixed with Matrigel (Corning) and seeded on 24-well plates. 500μl of ENR medium with WNT3a conditional medium, ROCKi and CHIR was added to each well. After 5-day culture at 37°C in a CO2 incubator, organoids were again digested to single cells and sorted for positive fluorescent signal. Following another round of 5-day culture, 30-50 single organoids were hand-picked and seeded in individual wells for expansion. The fluorescent signal of the reporter was verified via live imaging. 5 organoid lines with positive signal were selected and further stained for cell markers to check the cellular composition of the organoid tissue. The organoid line with the appropriate fluorescent signal and cellular composition were selected for experiments. Single cells were tracked for a period of one cell division. Time heterogeneity was calculated as the coefficient of variation of CTGF within the same cell over time.

### Microwell experiments

Microwells were prepared as previously described.[51] In brief, PDMS stamps were plasma treated and Collagen type I (Koken) - Matrigel mix (20%/80%) was added and inverted onto glass-bottom MatTek dish on top of two spacers. After 30min of solidification at

Please cite this article in press as: Schwayer et al., Multiscale integration of tissue and chromatin context converts cell heterogeneity into stable intestinal patterning, Cell (2026), https://doi.org/10.1016/j.cell.2026.06.009



37°C, the stamp was removed and the single-cell suspension was added. After 5min, cells were seeded in the microwells, and gentle washing was performed to get rid of the remaining cells. A Collagen-Matrigel mix (20%/80%) was added onto a cover slip and inverted on top of the microwells and incubated for 15 min. ISC expansion medium and Thiazovivin (2.5 μM; Stemgent) was added. ISC expansion medium: DMEM/F-12 with 15mM HEPES (STEM CELL Technologies) supplemented with 100 μg/ml Penicillin-Streptomycin, 1×Glutamax (Thermo Fisher Scientific), 1×B27 (Thermo Fisher Scientific), 1xN2 (Thermo Fisher Scientific), 1mM N-acetylcysteine (Sigma), 500ng/ml R-Spondin (kind gift from Novartis), 100 ng/ml Noggin (PeproTech) and 50 ng/ml murine EGF (R&D Systems) plus 3μM GSK-3β inhibitor CHIR99021 (Stem Cell Technologies, cat# 72052) and 1mM valproic Acid (Sigma #P4543).

## 2D organoid culture

### *Hydrogel preparation*

Hydrigel preparation was adapted from an existing protocol.[86] Hydrogels were generated using a collagen I and Matrigel composite matrix to recapitulate key features of the extracellular matrix (ECM). Type I atelocollagen (5 mg/mL; ReproCELL, cat. no. KKN-IPC-50) was used as the primary structural component. To prevent premature fibrillogenesis, all reagents and consumables were maintained on ice throughout the preparation procedure.

A neutralized collagen precursor was prepared by combining collagen stock solution with 10× DMEM and sodium bicarbonate at an 8:1:1 volume ratio. For example, 160 μL collagen was mixed with 20 μL DMEM, 20 μL 10× DMEM and 1.4ul od Sodium Bicarbonate, yielding a final concentration of 4 mg/mL. The mixture was gently pipetted to ensure homogeneity while minimizing bubble formation. Successful pH adjustment was visually confirmed by the phenol red indicator shifting from yellow to a light pink color. To generate the final hydrogel formulation, the neutralized collagen precursor was combined with Matrigel (10 mg/mL) at a 4:1 volume ratio. This resulted in a final matrix composition of 3.2 mg/mL collagen and 2 mg/mL Matrigel, corresponding to a total protein concentration of approximately 5.2 mg/mL. The mixture was gently homogenized on ice immediately prior to plating. For gel formation, 96-well glass-bottom plates were subjected to plasma treatment to enhance surface wettability. Plates were kept chilled before matrix deposition to avoid premature polymerization. A 25 μL aliquot of the hydrogel mixture was dispensed into each well to evenly cover the bottom surface. Polymerization was induced by transferring the plate to a 37°C incubator for 30 minutes.

### *Seeding*

For seeding, fully grown intestinal organoids were dissociated into single cells using TrypLE Express (Thermo Fisher Scientific) for 5 min at 37°C. For one well of 96-well plate we seeded 50k cells/well. After disaggregation, the organoids were centrifuged at 600xg for 5 min at 4°C and the pellet was resuspended in ENR medium supplemented with 15–20% Wnt3a-conditioned medium. The organoids were seeded in a small volume (30 μL) in each chamber and incubated at 37 °C and 5% CO2. Medium was refreshed every day. All experiments were performed 3 d after seeding.

## Laser Ablation on 2D organoids

Laser ablation was performed on confluent intestinal epithelial monolayers cultured on collagen–Matrigel matrices as described above. Targeted ablation was performed using a STELLARIS8 equipped with a femtosecond pulsed infrared two-photon laser (tunable 680–1030 nm). A 25× water immersion objective (NA 0.95) was used to focus the laser at the basal plane of the monolayer. Regions of interest (ROIs) were circular, manually defined, and targeted to the basal cell–matrix interface. Ablation was performed at 25% laser power with 10 consecutive repetitions per ROI. Pixel size was set to 0.9 μm. Cells for ablation were manually selected, and ROIs were positioned to selectively disrupt basal cell–cell junctions. Non-ablated regions within the same monolayer served as internal controls.

## scATAC sequencing time course

Wild-type organoids, isolated from a 10 weeks old male C57BL/6 mouse, were collected in cold advanced DMEM/F-12 with 15 mM HEPES (Stem Cell Technologies, cat# 36254), supplemented with 100 μg/mL Penicillin-Streptomycin and 1× Glutamax (Thermo Scientific, cat# 35050061). The organoids were pelleted at 600xg for 5 minutes at 4°C and digested into single cells at 37°C in a water bath for 20min using TrypLE (Life Technologies, #12604013) containing 10μM ROCK inhibitor (Y-27632). After digestion, single cells were pelleted at 600xg for 5min at 4°C, resuspended in PBS supplemented with 10μM ROCK inhibitor, and passed through a 30μm cell strainer. Single cells were sorted using a Becton Dickinson Influx cell sorter or SONY, MA900 cell sorter equipped with a 100μm nozzle. Live single cells were gated based on DRAQ7 staining, size, and granularity. Sorted cells were collected in 1.5mL tubes containing 200μL ENR medium supplemented with 10μM ROCK inhibitor, then pelleted at 900xg for 5 minutes. The cell pellets were resuspended in ENR medium consisting of advanced DMEM/F-12 with 15mM HEPES (Stem Cell Technologies, cat# 36254), supplemented with 100 μg/mL Penicillin-Streptomycin, 1× Glutamax (Thermo Scientific, cat# 35050061), 1× B27 (Thermo Scientific, cat# A1895602), 1× N2 (Thermo Scientific, cat# 17502001), 1 mM N-acetylcysteine (Sigma, cat# A7250), 500 ng/mL R-Spondin (Novartis), 100 ng/mL Noggin (PeproTech, cat# 250-38), and 100 ng/mL murine epidermal growth factor (EGF; R&D Systems). The medium was mixed with Matrigel (Corning) at a 1:1 ratio. For each well of a six-well plate, five droplets of 50μL, each containing 30,000 single cells (i.e. 0.6k cell/μL), were seeded and cultured for 24h in ENR medium supplemented with 25% WNT3A-conditioned medium (WNT3A-CM), 10μM ROCK inhibitor (Stem Cell Technologies, cat# 72304), and 3μM GSK-3β inhibitor CHIR99021 (Stem Cell Technologies, cat# 72052). From 24h to 72h, organoids were cultured in ENR medium supplemented with 25% WNT3A-CM and 10μM ROCK inhibitor, and from 72h onwards, ENR medium alone was used. Organoids were harvested at 24, 36, 48, 60, 72, and 84 hours

Please cite this article in press as: Schwayer et al., Multiscale integration of tissue and chromatin context converts cell heterogeneity into stable intestinal patterning, Cell (2026), https://doi.org/10.1016/j.cell.2026.06.009



post-seeding. Harvested organoids were digested into single cells and prepared for FACS sorting as described above. Sorted cells (50 – 100k) were collected in 1.5 mL tubes containing 200µl ENR medium supplemented with 10µM ROCK inhibitor. The cells were pelleted at 900xg for 5min at 4°C, and the pellet was resuspended in 600µL freezing medium (Stem Cell Technologies, cat# 210373) supplemented with 10µM ROCK inhibitor. Cell suspensions were frozen in cryo-boxes at -80°C and transferred to liquid nitrogen storage after 24h.

### Nuclei Isolation and scATAC-seq Library Preparation

The sorted and cryopreserved cells from each organoid time point were thawed in a 37°C water bath and washed three times with 0.8% BSA-PBS. After the third wash, cells were transferred into BSA-coated 0.2mL PCR tubes. Nuclei were then isolated using a low-input nuclei isolation protocol (Demonstrated protocol CG000169 · Rev D, 10x Genomics), with an 8-minute lysis time. Propidium iodide was used to identify the nuclei, and counting was performed using the MoxiGo II counter (Orflo Technologies). Nuclei were loaded to achieve a target recovery of 10,000 nuclei; if recovery was insufficient, all available nuclei were loaded instead. scATAC-seq libraries were generated using the Chromium Single Cell ATAC Library & Gel Bead Kit (PN-1000110) following the user guide (CG000168 · Rev A, 10x Genomics). Libraries were sequenced on the Illumina NovaSeq platform.

### ChIPseq sample dissociation

Lgr5::DTR-eGFP organoids were grown in ENR medium supplemented with 1:2000 DMSO (5µM YAP activator, or 5µM DAPT) and collected 4-days after mechanical splittin g. Organoids were collected in 5ml DMEM/F-12 with 15mM HEPES (Stem Cell Technologies, cat# 36254), supplemented with 100 µg/mL Penicillin-Streptomycin, 1× Glutamax (Thermo Scientific, cat# 35050061), and pelleted at 600xg for 5 min at 4°C. After discarding supernatant, organoids were resuspended in 2ml TrypLE (Life Technologies, #12604013) and 10µM ROCK inhibitor and incubated at room temperature for 10min; every 5min the mix was resuspended pipetting for 10x, to ensure single cell dissociation. To quench TrypLE reaction, 6ml DMEM/F-12 with 15mM HEPES (Stem Cell Technologies, cat# 36254), supplemented with 100 µg/mL Penicillin-Streptomycin, 1× Glutamax (Thermo Scientific, cat# 35050061) was added to the suspension. After pelleting single-cell suspension at 600xg for 5min at 4°C cell pellet was resuspended in 1ml PBS and filtered through FACS tube (35µm, #352235 Corning). Cells were counted and 10M cells per sample were resuspended in 10ml PBS before proceeding with ChIP library preparation.

### ChIPseq library preparation and sequencing

ChIP was done as described in Kaaij et al. *Cell* 2019 with minor modifications.[87] A total of $10^7$ cells were crosslinked for 8min at room temperature in 10mL PBS supplemented with 1% formaldehyde (Sigma, F8775). The reaction was quenched by adding glycine to a final concentration of 0.125M. Cells were pelleted by centrifugation at 500×g for 3min at 4°C, washed once with PBS, pelleted again, flash-frozen in liquid nitrogen, and stored until further processing. 30µL of a 1:1 mixture of Protein A/G Dynabeads (Invitrogen, 10002D and 10004D) was pre-coupled with 3µL of FOXA1 antibody (ab170933) for 1 hour at room temperature, followed by three washes with 1× ChIP buffer and stored on ice until use. The cells were lysed in 10mL of buffer A (50mM HEPES pH 8.0, 140mM NaCl, 1mM EDTA, 10% glycerol, 0.5% NP-40, 0.25% Triton X-100) on ice for 10min. After centrifugation, the pellet was resuspended in 5mL of buffer B (10mM Tris pH 8.0, 1mM EDTA, 0.5mM EGTA, 200mM NaCl) and incubated on ice for 5min. Nuclei were pelleted by centrifugation at 500×g for 3min at 4°C, resuspended in 150µL of buffer C (50mM Tris pH 8.0, 5mM EDTA, 1% SDS, 100mM NaCl), and incubated on ice for 10min. TE buffer (1.3mL) was then added, and chromatin was sheared in 15mL tubes using a Bioruptor Pico device for two sessions of 10 cycles (30 seconds ON / 30 seconds OFF). After shearing, 160µL of 10× ChIP buffer (0.1% SDS, 10% Triton X-100, 12mM EDTA, 167mM Tris-HCl pH 8.0, 1.67M NaCl) was added. The chromatin was transferred to fresh tubes and centrifuged at 13,000×g for 10min at 4°C. Per sample, 30µL of 1:1 pre-coupled beads were added to the chromatin, and the mixture was incubated with rotation for 4 hours at 4°C. The ChIP samples were washed four times with LSB (10mM Tris-HCl pH 8.0, 1mM EDTA pH 8.0, 140mM NaCl, 1% Triton X-100, 0.1% SDS, 0.1% sodium deoxycholate), twice with HSB (same as LSB but with 500mM NaCl), twice with LiSB (10mM Tris-HCl pH 8.0, 1mM EDTA pH 8.0, 250mM LiCl, 0.5% NP-40, 0.5% sodium deoxycholate), and once with TE+ buffer (10mM Tris-HCl pH 8.0, 1mM EDTA, 50mM NaCl). During the final wash, beads were transferred to fresh tubes, and the wash buffer was completely removed. DNA was eluted twice from the beads using 75µL of elution buffer (10mM Tris-HCl pH 8.0, 1mM EDTA pH 8.0, 150mM NaCl, 1% SDS) by incubation at 65C with shaking. The eluates were pooled, and 2µL of RNase A (20 µg/µL) was added, followed by incubation for 1 hour at 37°C. Input samples were adjusted to a total volume of 150µL with elution buffer and processed in the same manner as ChIP samples. Proteinase K (2µL, 20mg/mL) was added, and samples were incubated for 2 hours at 55°C and then for 6 hours at 65°C. Afterward, 9µL of 5M NaCl, 30µL of AMPure XP beads, and 190µL of isopropanol were added. Samples were vigorously mixed, incubated at room temperature for 10min, and the beads were collected on a magnetic rack. The beads were washed twice with 80% ethanol, and DNA was eluted in 30µL of 10mM Tris-HCl pH 8.0 for 5min at 37°C. For library preparation, 25µL of ChIP DNA or 50ng of input DNA was used with the NEBNext Ultra II Library Prep Kit for Illumina (NEB), following the manufacturer's protocol but with reactions scaled down to half-volume. Libraries were sequenced on the NovaSeq 6000 platform (Illumina) with paired end reads (2x 56 bp).

Please cite this article in press as: Schwayer et al., Multiscale integration of tissue and chromatin context converts cell heterogeneity into stable intestinal patterning, Cell (2026), https://doi.org/10.1016/j.cell.2026.06.009



### scRNA sequencing time course

Small intestinal organoids were derived from the duodenum of a 10-week-old male C57BL/6 wild-type mouse as described in Sato et al, Nature 2009. For amplification and maintenance, organoids were cultured in IntestiCult Organoid Growth Medium (STEMCELL Technologies) with 100 μg/ml Penicillin-Streptomycin. Organoid timecourses were started by performing a single-cell dissociation of the maintenance cultures. Specifically, organoids were collected 6 days after passaging and digested with TripLE (Invitrogen) with 10 μM Y-27632 (ROCK inhibitor; STEMCELL Technologies) for 20 min at 37 °C. Dissociated cells were passed through a cell strainer with a pore size of 30 μm and stained with DRAQ7 dye (Invitrogen). Single cells were isolated by fluorescence-activated cell sorting (FACS; SONY MA900 Cell Sorter) by gating for live (DRAQ7-negative) single cells. Cells were seeded into Matrigel (Corining) droplets (1:1 ratio Matrigel:ENR medium) at a density of 600 cell/ul, marking the start of the organoid timecourse. ENR medium consisted of Advanced DMEM/F-12 with 15 mM HEPES (STEM CELL Technologies) supplemented with 100 μg/ml Penicillin and Streptomycin, 1x Glutamax (Thermo Fisher Scientific), 1x B27 (Thermo Fisher Scientific), 1x N2 (Thermo Fisher Scientific), 1 mM N-acetylcysteine (Sigma), 500 ng/ml R-Spondin (kind gift from Novartis), 100 ng/ml Noggin (PeproTech) and 100 ng/ml murine EGF (R&D Systems). For the first 24 hours of the timecourse, ENR was supplemented with 25% Wnt3a-conditioned medium (Wnt3a-CM), 10 μM Y-27632 (ROCK inhibitor, STEMCELL Technologies) and 3 μM of CHIR99021 (STEMCELL Technologies). From 24 to 72 hr, ENR was supplemented with 25% Wnt3a-CM and 10 μM Y-27632 (ROCK inhibitor, STEMCELL Technologies). From 72 to 108 hr, only ENR was added to the organoids. Wnt3a-CM was produced in-house by Wnt3a L-cells (kind gift from Novartis).

### Single cell isolation and scRNA-seq Library Preparation

Organoids were collected at baseline (0h) and at 12-hour intervals throughout the regeneration timecourse (24-108h) for single cell RNA sequencing. For each timepoint, organoids were collected and digested to a single-cell suspension and FACS sorted as described above. For single-cell RNA sequencing library preparation, 13k cells were sorted per collection vial per timepoint. Single-cell libraries were prepared using the 10x Genomics Chromium Single Cell 3′ Reagent Kit v2 according to the manufacturer's protocol. Gel bead-in-emulsion (GEM) generation, reverse transcription, cDNA amplification, and library construction were performed following standard procedures. Libraries were sequenced on an Illumina NextSeq 500 platform using a 75-cycle kit with paired-end configuration (Read 1: 26 bp; Read 2: 56 bp; single index: 8 bp). Base calling was performed using Illumina RTA (v2.4.11), and FASTQ files were generated using bcl2fastq2 (v2.17).

### HCR-FISH of Notch ligands

All solutions used for HCR-FISH were prepared nuclease free. Mouse intestinal organoids grown either on 96-well plates (Greiner, 655090) or Ibidi 18-well glass bottom plates. Organoids were fixed for each time point 45min at room temperature in a 4% formaldehyde solution (EMS) in PBS. Samples were then washed 3 times in PBS and kept in a preserving solution (20% PEG200, Sigma P3015, 50% formamide, Sigma Aldrich #4610, in 2x SSC) overnight with agitation before transfer at -20°C until use. Upon use, samples were washed twice with PBS Tween 0.2% and permeabilized at room temperature under gentle agitation with 3 different solutions used sequentially as follow: 2 x 40min SDS 4% in 200mM Boric acid pH7, 5x5min in PBS Triton 0.5%, 3x2min in PBS Tween 0,2%. Sample autofluorescence was then quenched as per Morabito et al.[88] with slight modifications: the bleaching solution (5% hydrogen peroxide, Sigma H1009, in PBS) was prepared each time fresh, without sodium hydroxide to avoid RNA degradation, and added for 30min under a custom made photobleacher equipped with 25 x 36.W white LED (Samsung). Samples were then washed 3x5min in PBS. All probes sets were designed with Oligominer webapp[89] based on the Oligominer probe design pipeline,[90] checked for off-target sequences with BLAST, and subsequently split and appended with half initiator sequences (for B1, B2 or B5 amplifiers) as per HCR-FISH v3 probe design.[91] Hybridization and amplification steps were performed with commercial buffers and amplifiers from to Molecular Instruments, according to protocol instructions for samples in solution from the manufacturer. Samples were then stained with Dapi (VWR #ACRO202710500, 2μg/mL) in PBS for 1h, briefly washed in PBS, and mounted in SlowFade glass (ThermoFisher #S36917) prior to imaging.

Imaging of organoids was performed as mentioned in the section 'High-throughput imaging of mouse intestinal organoid time course' or using an inverted Zeiss AxioObserver (Zeiss) with a Zeiss 40x/1.3 NA oil objective equipped with a CSU-W1 Confocal Scanner Unit (Yokogawa, 50um pinhole disk unit), 2 sCMOS cameras (Orca-Fusion BT, Hamamatsu), a MS2000 motorized stage with z-piezo drive (Applied Scientific Instrumentation) and controlled with VisiView 6.0 imaging software (Visitron Systems GmbH). Illumination was achieved with a Ziva Light Engine (Lumencor) equipped with 7 solid-state lasers, and HCR-FISH signals and DAPI were specifically imaged with the 639nm, 577nm and 405nm laser lines. Emission filters used were as follow: BP 445/49, BP 606/18, BP 691/64. Z-stacks with 1 micron interval were acquired, and Z-series were acquired first, then channels. Quantification and downstream analysis of HCR-FISH was performed as described in section '*Image analysis of high-content organoid data*'.

### Generation of Agr2-p2a-FLAG-mStayGold-2xNLS; 8xSTAR-sTom-2xNLS organoids

Organoids were cultured under standard expansion conditions using IntestiCult Organoid Growth Medium (STEMCELL Technologies) or ENR medium (see Mouse intestinal organoid regeneration time course). The Agr2-p2a-FLAG-mStayGold-2xNLS; 8xSTAR-sTom-2xNLS organoid line was generated in the inducible Cas9 background B6;129S4-Gt(ROSA) 26Sortm1(rtTA*M2)Jae Col1a1tm1(tetO-cas9)Sho/J (KH2/iCas9; RRID: IMSR_JAX:029415).

Please cite this article in press as: Schwayer et al., Multiscale integration of tissue and chromatin context converts cell heterogeneity into stable intestinal patterning, Cell (2026), https://doi.org/10.1016/j.cell.2026.06.009



### CRISPR/Cas9-Mediated Targeting of the Agr2 Locus

sgRNAs targeting the Agr2 locus were designed using the CRISPR tool available on (https://benchling.com), prioritizing guides with high predicted on-target efficiency and minimal off-target risk. The selected guide sequence (5′-TGTAGAGCCAACTGCGCACC-3′) overlapped the Agr2 stop codon to facilitate C-terminal tagging (Figure S1E). Synthetic crRNA and tracrRNA (IDT) were annealed to generate the guide RNA duplex. Organoids were dissociated into single cells and electroporated with the crRNA:tracrRNA duplex together with an HDR targeting construct encoding p2a-FLAG-mStayGold-2xNLS. Electroporation was performed using a NEPA21 electroporator (NEPA GENE) according to a previously established protocol.[92] In brief, 24h prior to electroporation, organoids were cultured in electroporation medium consisting of ENR medium without Pen/Strep supplemented with ROCK inhibitor (ROCKi) and CHIR99021. To enhance single-cell survival and editing efficiency, 1.25% DMSO was added to the electroporation medium 4–12 h prior to electroporation. Organoids were subsequently dissociated into single cells and resuspended in BTX electroporation solution (BTX; cat# 732-1285). For transposon-based reporter integration, 1 × 10 ^6 single cells were mixed with 10 μg reporter plasmid DNA 8xSTAR-sTom-2xNLS construct (Addgene plasmid #136261) (see KRT for construct details) and 5 μg pminiTol2 plasmid in a final volume of 100 μl.[49,50] For endogenous knock-in experiments, synthetic crRNA and tracrRNA (IDT) were annealed to generate guide RNA duplexes and combined with 10 μg HDR donor constructs containing the desired insert flanked by 5′ and 3′ homology arms (e.g., 5′ homology arm–P2A-FLAG-mStayGold-2xNLS–3′ homology arm). Cell–DNA/RNP mixtures were maintained on ice prior to electroporation.

The mixtures were transferred to electroporation cuvettes, and impedance was confirmed to fall within the range of 0.030–0.055 prior to pulsing. Immediately following electroporation, 400 μl Opti-MEM supplemented with ROCKi was added to dilute the electroporation mixture. Cells were incubated at room temperature for 30 min and subsequently centrifuged at 500 × g for 5 min at 4°C. The supernatant was removed, and cell pellets were resuspended in a 1:1 mixture of Matrigel (Corning) and electroporation medium supplemented with 1.25% DMSO. Cells were seeded into two wells of a 6-well plate. After 2 h, the medium was replaced with fresh electroporation medium lacking DMSO.

For organoid recovery and expansion, cultures were maintained according to the established single-cell outgrowth protocol in antibiotic-free conditions. After 5 days of culture at 37°C and 5% CO2, organoids were dissociated into single cells and either enriched by fluorescence-activated cell sorting (FACS) based on reporter expression or subjected to the appropriate selection strategy corresponding to the integrated construct (i.e., blasticidin selection (3 μg/mL for the STAR-reporter). Resistant organoids were manually isolated and clonally expanded.

### Clonal Isolation and Validation

Single organoid clones were manually picked and expanded. One monoclonal line was selected and used for all downstream experiments to ensure experimental consistency and reproducibility. Correct targeting and expression of the Agr2 fusion protein were validated by immunofluorescence staining using an Agr2-specific antibody.

## Lineage-biased time-course experiment using AGR-STAR organoid line

Single-cell dissociation was performed as described in '*Mouse intestinal organoid regeneration time course*', with a FACS-based sorting strategy of using the top 15% of mTomato signal to isolate stem cells (STAR+ cells), 488-positive cell population - identified by comparing to negative wildtype control sample - to isolate secretory cells, and double-negative cells to isolate enterocytes.

## Lineage-enrichment time-course experiment using compound treatments

To perform lineage enrichments for the different cell types, previously published compound treatment combinations were used.[48] To enrich for stem cells, organoids were cultured for 24 days in CHIR99021 (1.5-3 μM, Stemgent) and valproic acid (0.5-1 mM, Sigma-Aldrich); to enrich for secretory progenitors, in CHIR99021 (1.5-3 μM, Stemgent) and DAPT (5-10 μM, Stemgent), and to enrich for enterocyte progenitors, in IWP-2 (1-2μM, Stemgent) and valproic acid (0.5-1 mM, Sigma-Aldrich). The pre-treatment conditions were performed in ENR medium along with a DMSO control. Single-cell time-course experiments were then performed as described in '*Mouse intestinal organoid regeneration time course*'.

## Human intestinal organoid regeneration time course and culturing

Mature organoids are collected by rinsing the culture well with 1-2 ml ice cold DMEM++ (DMEM/F12 and 15 mM HEPES, Stem Cell Technologies + 1x GlutaMAX, Thermo Fisher Scientific + 100 U/ml Penicilin/Streptomycin, Thermo Fisher Scientific) and transferring the solution into a 15 ml tube (Falcon). Next, DMEM+++ is added until a total volume of 7 ml is reached before centrifuging the tube at 400xg for 4 min at 4°C. Supernatant is discarded and organoids are resuspended into 2 ml of prewarmed 0.05% Trypsin + EDTA (Gibco) and incubated for ~10 min at 37°C. Trypsinization is stopped using 2 ml of a trypsin-inhibitor (Thermo Fisher Scientific) as well as 3 ml of DMEM+++ after reaching a single-cell suspension. Singularized cells are then centrifuged at 600xg for 5 min at 4°C and supernatant is discarded subsequently. Next, the cell pellet is resuspended into Start medium[93] and then filtered through a 40 μm filter to remove large debris and cell clumps. Filtered cells were FAC-sorted to remove remaining smaller debris as well as doublets and count the number of remaining cells. Finally, the cell-suspension is diluted to 50 cells/μl into a ~66% Matrigel (corning) and ~34% Start medium as previously described[28]: 0.5 nM Next-Generation Surrogate WNT (WNT-NGS, UproteinExpress), 1 μg/ml human R-Spondin1 (gift from Novartis), 100 ng/ml murine Noggin (PeproTech), 1.25 mM N-acetylcysteine (Sigma), 0.5 μM A83-01 (Sigma), 100 ng/ml human IGF1 (R&D Systems), 50 ng/ml human FGF2, 1x B27 supplement (Thermo Fisher Scientific), 25 nM human Gastrin, 50 ng/ml human EGF (R&D Systems), 1 ng/ml human NRG1 (R&D Systems), 10 μM Y-27632, 100 U/ml

Please cite this article in press as: Schwayer et al., Multiscale integration of tissue and chromatin context converts cell heterogeneity into stable intestinal patterning, Cell (2026), https://doi.org/10.1016/j.cell.2026.06.009



Penicillin/Streptomycin, 1x Glutamax (Thermo Fisher Scientific) supplement diluted in DMEM/F12 (+15 mM HEPES). A minor modification to the timing described in Oost et al. was implemented. Based on empirical optimization by the authors, cultures for time-course experiments were maintained in Start medium for four days, followed by two additional days in Start medium without Y-27632.

For maintenance, the Matrigel mixture is plated into cell culture plates (Corning) in 15-20 μl droplets and are covered after a 20 min 37°C solidification period with warm *Start* medium. Medium is changed after 5 days to *Balanc*e medium which is the same as Start medium, but without the Wnt-NGS, A83-01, Y-27632, and with adjusted concentrations of 0.5 μg/ml human R-spondin, 5 ng/mL human EGF, 10 ng/mL human NRG1 and plus 2.5 μM all-trans retinoic acid (Sigma-Aldrich) and is refreshed once with new *Balance* medium at day 7 and 10 until maturation is reached, typically at day 13.

Fixation and antibody staining of human small intestinal regenerative time course was performed as described in '*Fixed sample preparation and antibody staining*', imaging was performed as described in '*High-throughput imaging of mouse intestinal organoid time course*' and quantification and downstream analysis was performed as described in section '*Image analysis of high-content organoid data*'.

### Mouse Salivary Gland Organoids

#### *Organoid generation and culturing*

Mouse salivary gland organoids (SGO) were derived from submandibular glands of C57BL/6 mice and maintained in DMEM/F12 supplemented with 15 mM HEPES (STEMCELL Technologies), 1× GlutaMAX (Thermo Fisher Scientific), and Primocin (100 μg/mL Invivogen). Basal medium was further supplemented with B27 (1:50 Thermo Fisher Scientific), N-acetylcysteine (1.25 mM Sigma-Aldrich), recombinant Wnt surrogate Fc (0.5 nM UproteinExpress), R-spondin 1 (1 μg/mL kind gift from Novartis), Noggin (100 ng/mL PeproTech), Nrg1 (10 ng/mL R&D systems ), IGF1 (100 ng/mL R&D systems), FGF2 (50 ng/mL R&D systems), and A83-01 (0.5 μM Sigma-Aldrich). This formulation is referred to as mouse SGO expansion medium.

#### *Single-Cell Regeneration Time-Course Assay*

For regeneration experiments, mature organoids were collected, washed in cold basal medium, and brought to a total volume of 7 mL prior to centrifugation at 400×g for 4 min at 4°C. The supernatant was removed, and organoids were resuspended in prewarmed 0.05% trypsin-EDTA (Gibco) and incubated at 37°C until dissociation into single cells was achieved. Trypsinization was quenched by addition of trypsin inhibitor (Thermo Fisher Scientific) together with basal medium. Cells were centrifuged at 600×g for 5 min at 4°C, and the pellet was resuspended in mouse SGO expansion medium and passed through a 40 μm cell strainer to remove debris and residual aggregates. Single cells were embedded in approximately 66% growth factor–reduced Matrigel (Corning) diluted in mouse SGO expansion medium and plated at a density of 40 cells/μL. For regeneration time-course experiments, cultures were maintained in mouse SGO expansion medium containing the ROCK inhibitor Y-27632 (10 μM) for the first three days following single cell plating. Thereafter, medium lacking Y-27632 was refreshed, and cultures were maintained until day 6. Fixation and antibody staining of mouse salivary gland regenerative time course was performed as described in '*Fixed sample preparation and antibody staining*', imaging was performed as described in '*High-throughput imaging of mouse intestinal organoid time course*' and quantification and downstream analysis was performed as described in section '*Image analysis of high-content organoid data*'.

### Diphteria Toxin time-course experiment

Time course experiment was performed as in section 'Mouse intestinal organoid regeneration time course'. LGR5-DTR-eGFP signal was imaged using Yokogawa (CellVoyager 7000S) at low resolution (20x objective) before addition of diphteria toxin to identify the organoids with already present LGR5+ stem cells. Diphteria toxin (DT) was added at 60h after single-cell plating at a concentration of 0.05 μM (Sigma). Fixation at 72h and stainings were performed as described in section 'Fixed sample preparation and antibody staining'. Organoids were imaged first at 20x to perform organoid matching after 12h of growth and then imaged at 40x for high resolution imaging of YAP1 activity.

### Mouse colon organoid regeneration

Organoids were collected in cold DMEM/F-12 with 15 mM HEPES (Stem Cell Technologies) supplemented with 100 μg/ml Penicillin–Streptomycin, 1× Glutamax (Thermo Scientific) between 3-5 days after passaging. Passaged organoids were centrifuged at 600×g for 5 min at 4°C. Organoids were collected in 30% ENR medium supplemented with 30% Wnt3a-conditioned medium and 10μM Y-27632 (ROCK inhibitor, STEMCELL Technologies) and 70% matrigel. 5ul droplets of hard split organoids were seeded per well of a 96-well plate (Greiner, 655090). After 20min of solidification at 37°C, 100μl of medium was added per well. Fixation and antibody staining of mouse colon organoids was performed as described in '*Fixed sample preparation and antibody staining*', imaging was performed as described in '*High-throughput imaging of mouse intestinal organoid time course*' and quantification and downstream analysis was performed as described in section '*Image analysis of high-content organoid data*'.

## QUANTIFICATION AND STATISTICAL ANALYSIS

### Lineage analysis of DLL1-P2A-mcherry line in lightsheet imaging

The analysis of the DLL1 movies was performed using the framework described in.[85] After cropping the raw data, the denoising algorithm from[85] was applied, followed by deconvolution. To predict single-cell tracks, the RDCNet network[85] was used on the H2B

channel. Individual tracks were manually inspected and corrected using the Fiji plugin Mastodon. Subsequently, the emergence of DLL1-positive cells was determined by visually inspecting the corresponding fluorescence channel. By combining the corrected track predictions with the DLL1 fluorescence data, we determined whether both daughter cells of a dividing DLL1-positive mother cell expressed DLL1.

## Image analysis of high-content organoid data

### *Raw-image processing, 2D and 3D segmentation, feature extraction*

Raw-images were converted to the Open Microscopy Environment format (OME-Zarr)[94,95] using the Fractal platform (https://fractal-analytics-platform.github.io/). Where needed, the python package 'ez-zarr' (https://fmicompbio.github.io/ez_zarr/) was used for post-processing of OME-Zarr (e.g. feature extraction).[96] Whole-well MIPs of the DAPI-channel were segmented with a custom model using RDCNet (version v0.4).[97] For nuclei segmentations, a RDCnet model[97] was trained from scratch based on 3D data of DAPI stained organoids from 24h-72h of organoid regeneration time courses. For cell segmentations, 2D and 3D Cellpose[98] models were re-trained based on 3D data of DAPI stained nuclei and E-cadherin stained cell membranes of organoids from 24h-72h regeneration time courses. Nuclei and cell segmentations were linked through maximum overlap. Feature extraction of single-nucleus, cell, cytoplasm and organoid-level information was performed using the scikit-image package[99] and custom-written code in Python. Extracted features were casted in a SingleCellExperiment object for further post-processing.

### *Quality control and normalization*

Organoid filtering was performed by removing single-cells and debris based on area measurements. Mis-segmented organoids were filtered out by calculating the Euler number and only retaining objects with Euler number equals to one and by applying an object-to-bounding box filter and only retaining objects covering more than 5% of the label mask. Mis-segmentations of single-cells were filtered by identifying empty masks (low DAPI mean intensity) and too small cells (smaller than 1/10 of the median size observed). To correct for signal decay along the z-axis due to reduced penetration in the sample, for each intensity feature we summarised measurements along z-axis into 7 to 8 bins (averaging 1,200 to 9,000 single cell measurements per bin) and fit a loess model of intensity feature over z-axis bins (using the r function loess(), with span = 0.5, family = "symmetric", and control = loess.control(surface = "direct"). Finally, we subtract the fitted values from the raw extracted values. For z-score value calculation, data were standardized against the average (mu) and standard deviation (sigma) of the entire distribution or in case of perturbation experiments, data were standardized against the mu and sigma of DMSO or WT controls.

### *YAP1 activity readout*

YAP1 activity was quantified as the mean intensity (total signal divided by area) of active YAP1 antibody staining in the nucleus (unless otherwise indicated, eg. total YAP1 staining for microwells).

### *Single cell classification and cell-to-cell variability calculation*

For classification into YAP1$^{high/low}$, FOXA1$^{-/int/+}$, DLL1$^{-/int/+}$ k-means clustering was performed, where YAP1$^{-}$ cells were classified into YAP1$^{low}$ and YAP1$^{int/+}$ into YAP1$^{high}$ cells. Organoid-level mean intensities were calculated by averaging the z-scored mean intensities of all nuclei/cells per organoid. Coefficient of variation was calculated as standard deviation of the z-corrected mean intensity of all nuclei/cells per organoid divided by the average of the z-corrected mean intensity of all nuclei/cells. For the coefficient of variation of classified YAP1 activity, a pseudo-count of 0.01 was introduced in the calculation of the mean to avoid numerical instabilities during division. For line plots of organoid-level information, data were smoothed using the loess function in R; for single-cell data, the data frame was first uniformly subsampled (30 cells per cell-stage from >900 organoids) and then loess function was used to produce the smoothed line plots. Correlation plots were produced by correlating the single-cell FOXA1 and DLL1 z-scored mean intensities per organoid and then averaging the per-organoid level information. Loess function was used to produce smoothed line plots unless otherwise indicated in figure legends.

## Normalised density calculation

To allow comparison between 3D and 2D systems, we matched them based on surface geometry - specifically, by comparing surface area in 3D organoids to the perimeter in 2D systems (*in vivo* and microwells). Tissue density was defined as the number of nuclei per unit: either per 100 $\mu m^2$ of surface area in 3D data or per 10 $\mu m$ of perimeter in 2D data. To normalise tissue density across systems, we applied a scaling factor: for 3D organoids, this involved multiplying by the mean projected area of nuclei in 2D and dividing by the reference nuclear area (based on a reference diameter of 7.5 $\mu m$); for 2D data, we multiplied by the mean nuclear diameter and divided by the reference nuclear diameter (7.5 $\mu m$). The thresholds for intermediate density (0.5-1.1) were chosen based on the density values spanning the peak of CV of aYAP1 in organoids (Figure 1C').

## Statistical modeling of YAP1 heterogeneity

To investigate how nuclear YAP1 levels relate to local and global morpho-structural features in intestinal organoids, we implemented a multistep computational framework based on 2,162 organoids. To ensure robust morphological measurements and to enable extension to both 2D and 3D systems, all downstream analyses were restricted to nuclei located in the middle optical plane of each organoid, yielding a dataset of 18,030 nuclei.

To identify predictive features underlying YAP1 variability, we first selected a subset of 754 cells from 130 organoids exhibiting heterogeneous YAP1 expression, defined by a coefficient of variation (CV) in nuclear YAP1 intensity greater than 0.6. We applied

Please cite this article in press as: Schwayer et al., Multiscale integration of tissue and chromatin context converts cell heterogeneity into stable intestinal patterning, Cell (2026), https://doi.org/10.1016/j.cell.2026.06.009



stability selection[56] using the stabsel() function from the R package stabs, specifying a per-family error rate (PFER) of 1 and a selection probability cutoff of 0.9 to identify robust predictors. Variables were considered robust if their maximum selection probability (phat) exceeded 0.5 (Figure S4B). Among the features evaluated, local cell density (LCD) was calculated following the approach of Snijder et al. (2012).[100] Unlike the original implementation, which used a fixed radius, we computed the LCD across a range of radii from 3 to 15 μm in 0.5 μm increments. Instead of pre-selecting a radius, we allowed the stability selection framework to identify the most informative scale. This approach consistently retained an LCD measured at a 3.5 μm radius, which was subsequently used for all downstream analyses. The final selected features included: nuclear size, developmental stage ($log_2$-transformed division count), nuclear axis ratio (minor/major axis), developmental time, and LCD at 3.5 μm. We then used the full dataset (n = 18,030 nuclei) for model fitting and evaluation. The data were randomly split into an 80% training set and a 20% test set. A multivariable ordinary least squares (OLS) model was trained on the training subset using the five selected features to predict log-transformed nuclear YAP1 intensity. The model explained 40% of the variance in YAP1 levels and achieved a normalized root mean squared error (nRMSE) of 0.18. All projections and visualizations shown in Figures S4C and S4D are based on predictions from the held-out test set. To uncover interdependencies among the selected predictors and their relation to YAP1 activity, we computed a regularized conditional independence network (referred to as 'Graphical Gaussian Modeling', GGM in the main text). This approach is advantageous over simple correlation coefficients, as it reduces the risk of spurious correlations caused by strong covariations between predictors. Moreover, it provides a more interpretable and synthetic representation of the rules governing the relationship between YAP1 activity and local single cell features. All predictors were z-score standardized, and we performed 1,000 iterations of subsampling ($n$ = 200 nuclei per iteration). In each iteration, every feature was regressed on all others using linear models; coefficients were then averaged across iterations and symmetrized to construct a stable network of conditional dependencies. From this network, we observed that three features—nuclear size, local cell density (LCD), and nuclear axis ratio—formed a highly interconnected triad, suggesting coordinated regulation of nuclear morphology and local crowding in association with YAP1 activity. Based on the conditional dependency structure, we defined two prototypical mechanical states: State-1 (YAP-high prototype): low LCD (0), low axis ratio (0), high nuclear size (1), and State-2 (YAP-low prototype): high LCD (1), high axis ratio (1), low nuclear size (0). Mechanical features were min–max scaled to the [0,1] interval using the full organoid dataset. Each nucleus was projected onto the vector connecting State-1 to State-2 using a normalized vector projection:

$$t = \frac{(P - A) \cdot (B - A)}{\| B - A \|^2},$$

where $P$ is the scaled feature vector of a nucleus, and $A$ and $B$ correspond to the YAP-high and YAP-low prototypes, respectively. This projection defines a continuous morpho-axis, positioning each cell along a mechanical continuum from YAP-high to YAP-low states. The global morpho-axis range derived from untreated organoids was stored and used for normalization across experimental systems. To quantify how YAP1 activity varies along the morpho-axis, nuclear YAP1 intensities were log-transformed and z-score normalized using the mean and standard deviation of DMSO-treated control cells. To span the full mechanical range of the morpho-axis for curve fitting, we included Forskolin and PGE-treated samples. Importantly, these perturbations were used exclusively to extend the dynamic range of the morpho-axis for model fitting, and were not included in feature selection or GGM inference. Cells were binned along the morpho-axis, and mean YAP1 z-scores per bin were computed. The relationship between morpho-axis position and YAP1 activity was fitted using a four-parameter logistic (sigmoidal) model:

$$Y(x) = y_{low} + \frac{y_{high} - y_{low}}{1 + e^{-k(x - x_0)}},$$

where: $y_{low}$ and $y_{high}$ define lower and upper plateaus, $x_0$ represents the midpoint of transition, and $k$ describes the steepness of the transition. Model fitting was performed using nonlinear least squares (nls) on the normalized morpho-axis. This analysis revealed a sigmoidal dependence of YAP1 activity on the morpho-axis, characterized by buffered plateaus at both extremes and a narrow high-gain transition regime.

## scATACseq analysis

All analyses, unless stated otherwise, were performed within R (version 4.2.0) and Bioconductor (version 3.15),[101] using SeuratObject version 4.1.0, Seurat version 4.1.1, and Signac version 1.7.0.

### *Alignment and quantification*

Fragment files with aligned read coordinates were generated for each sample (one file per each of the timepoints: 24h, 36h, 48h, 60h, 72h, 84h), using CellRanger ATAC (version 1.2.0) with the "count" subtool and reference "refdata-cellranger-atac-mm10-1.2.0". For initial quantification, genomic features were obtained by combining promoters (transcription start sites (TSS) expanded to 1000 base pairs centered on the TSS) and enhancer from the cellranger annotation. All overlapping regions were collapsed, and any region overlapping a cellranger annotated blacklist region was removed. Alignments in these regions were then quantified with Signac::FeatureMatrix() from the fragment files.

### *Quality control, filtering, normalization and dimensionality reduction*

Cells with fewer than 300 detected features were excluded, and features detected in fewer than 10 cells were removed, yielding 83,493 cells across 302,405 features. Quality control metrics were calculated using TSSenrichment() and NucleosomeSignal(). Cells

with TSS enrichment $\leq$ 2, nucleosomal signal $\geq$ 5, $\leq$ 2,500 fragments, or $\leq$ 25% fragments in promoters (calculated using FRiP()) were excluded, resulting in 68,905 cells. Normalisation was performed with RunTFIDF() (method = 1, scale.factor = 10,000), and variable features were selected using FindTopFeatures() (min.cutoff = "q50"), yielding 151,214 features. Dimensionality reduction was performed using RunSVD() (n = 50). The first component of the resulting Latent Semantic Index (LSI) was excluded from all subsequent analysis as it showed high correlation with sequencing depth (as shown by DepthCor()). Using the remaining LSI components as input, a total of 38 clusters were identified using FindNeighbors() and FindClusters() (resolution = 3).

### YAP1 activity score and Motif enrichment

A per-cell YAP1 activity score was computed in single-cell ATAC-seq data using a gene module scoring approach adapted from established best practices for gene set activity inference in single-cell datasets.[102] Because gene accessibility serves as a proxy for regulatory activity in scATAC-seq, we quantified YAP1 activity by averaging the predicted expression of a curated YAP1 target gene set and subtracting the average signal of matched control genes within the same cell. The YAP1 target gene set was derived from a previously published and experimentally validated list of YAP1 target genes.[30] For each cell, a module score was calculated by comparing the mean accessibility of YAP1 target genes to that of control genes matched for overall expression characteristics, thereby controlling for cell-to-cell technical and biological variability.

To visualize YAP1 activity dynamics, cells were ordered according to their YAP1 activity score, thereby defining a continuous YAP-dynamic axis independent of predefined trajectories or principal components. Per-cell YAP1 activity scores were smoothed along this axis using generalized additive models (GAMs) implemented in the mgcv package (v1.9-3). Smoothing was performed using cubic regression splines (bs = "cs") with restricted maximum likelihood (REML) estimation and a gamma parameter of 3 to penalize overfitting. Smoothed predictions were evaluated on an evenly spaced grid along the YAP-dynamic axis, constrained to the observed data range to prevent edge overshoot, and remaining missing values were linearly interpolated. For heatmap visualization of YAP-associated chromatin accessibility dynamics, features significantly associated with the YAP-dynamic axis were first identified (FDR $\leq$ 0.05) and filtered for robust signal (95th percentile log-normalized accessibility > 0.05), yielding 11,000 peaks. Accessibility profiles were smoothed along the YAP-dynamic axis using the same GAM framework and scaled to a 0–1 range per feature. Features were clustered using k-means clustering (centers = 6, nstart = 10, iter.max = 50), and the resulting clusters were visualized using ComplexHeatmap.

To identify transcription factor motifs associated with distinct phases of YAP1 activity dynamics, genes were first grouped according to their smoothed expression patterns along pseudotime. Based on k-means clustering (k = 6) of pseudotime-smoothed gene expression profiles, clusters were consolidated into three biologically defined categories reflecting their temporal relationship to YAP1 activity: ‘‘YAP early’’ genes, enriched in YAP-high cells, ‘‘YAP prolonged’’ genes, expressed across YAP-high to YAP-mid states, and ‘‘YAP late’’ genes, enriched in YAP-low cells. These groups comprised 2,282 (YAP early), 6,486 (YAP prolonged), and 2,232 (YAP late) genes, respectively (11,000 genes total). Genomic regions corresponding to these genes were retrieved from the Seurat-based annotation object and resized to a uniform width centered on the region midpoint to standardize sequence length. DNA sequences were extracted using ‘getSeq()‘ and used as input for motif enrichment analysis. Motif enrichment was performed using ‘calcBinnedMotifEnrR()‘ from the monaLisa package. Sequences were assigned to bins corresponding to the three YAP dynamic groups (YAP early, YAP prolonged, YAP late). Enrichment was computed using the "otherBins" background option, such that each bin was compared against the combined set of sequences from the remaining bins. Position weight matrices (PWMs) from the JASPAR2020 database were used for motif scanning. For visualization, 2–3 representative motifs per class were selected based on enrichment strength, literature support, and relevance to intestinal lineage specification and fate patterning (Figure 1F’’).

### Predicted RNA expression, initial cell type annotation and peak calling

Gene coordinates were extracted from the reference (genes gtf file in refdata-cellranger-atac-mm10-1.2.0) including type = ‘‘gene’’ and gene_type = ‘‘protein_coding’’. Only standard chromosomes were retained, using GenomeInfoDb::keepStandardChromosomes(), with pruning.mode = ‘‘coarse’’. Predicted gene expression was quantified with GeneActitity(), with extend.upstream = 2000, extend.downstream = 0, biotypes = NULL (as only protein coding genes were already pre-selected), and max.width = 5e+05. The RNA count matrix was normalized with NormalizeData(), normalize.method = ‘‘LogNormalize’’ and scale.factor = median(seurat$nCount_RNA) (the median total predicted RNA count per cell). Coarse-grain cell type annotation was performed by assigning the 38 clusters to cell types based on predicted RNA expression of known markers of intestinal lineages averaged over cells in each cluster. We removed 1,929 cells (2 of the 38 clusters) showing high expression of stress markers (including *Hsp90aa1*, and *Hsp90b1*). Peaks were identified for each of these preliminary cell types with Signac::CallPeaks() using MACS2 (version 2.1.3.3),[103] with effective.genome.size = 1.87e9, extsize = 200, and shift = -100, and merged across clusters, yielding 252,049 peaks. A second fragment quantification was then performed using Signac::FeatureMatrix(), replacing the initial generic promoter/enhancer features by the sample specific peaks identified in our data.

### Final cell type annotation and transfer labels to full dataset

The preliminary cell type annotation revealed that regenerative and TA / Stem cell progenitors were much more abundant in our data compared to other cell types. In order to reduce the weight of these frequent cell types, for example in the identification of variable features, we randomly subsampled these two cell types from about 15,000 and 36,000 cells respectively to 10,000 each, reducing the total number of cells to 36,988 (seuratSubsampled object). The normalization and latent semantic indexing were then repeated on seuratSubsampled (runTFIDF(), FindTopFeatures(), RnuSVD()), and a 2D embedding was generated using RunUMAP with dims = 2:30, umap.method = ‘uwot’, n.neighbors = 30L, min.dist = 0.3 and spread = 1. Cell types were re-annotated by clustering

Please cite this article in press as: Schwayer et al., Multiscale integration of tissue and chromatin context converts cell heterogeneity into stable intestinal patterning, Cell (2026), https://doi.org/10.1016/j.cell.2026.06.009



seuratSubsampled using FindNeighbors() and FindClusters() with resolution = 2.0, resulting in 28 clusters, that were assigned to cell types using marker genes as described, resulting in final cell type assignment of the subsampled cells (Figure S8B). We transferred the cell type annotation from the seuratSubsampled to the full dataset, projecting all cells into the LSI and UMAP embeddings identified from the subsampled cells. Cell types of non-sampled cells were assigned using the cell type of the nearest subsampled cell in LSI space.

#### *Differential Accessibility and Motif Enrichment Analysis*

Log2 fold changes of accessibility between each of Reprogramming, Regenerative, Secretory progenitors, Exocrine, TA / Stem cell progenitors, Enterocyte progenitors and reprogramming cells were computed similarly as in Signac:::FoldChange.ChromatinAssay but using a pseudocount of 0.2. Peaks with absolute log2 fold change > 1.75 in any contrast were retained, yielding 10,938 differentially accessible peaks (Figure 3F). We calculated the average accessibility for each cell type by taking the mean of log2 normalized accessibility values over cells, and then calculated relative accessibility for each peak by linearly scaling its celltype averages into the interval from zero to one. Based on these relative accessibilities, peaks were clustered in 8 groups using the kmeans function in R. Motif enrichment analysis was performed with calcBinnedMotifEnrR() from the monaLisa package[104] in the 8 identified groups and JASPAR2020 as motif database. We sorted motifs by significance (“negLog10Padj”) and selected the top 50 plus TEAD motifs, which we manually included for their known role as YAP1 co-factors. The identified motifs were then clustered with motifSimilarity(), and 2–3 representative motifs were shown (Figures 3G and S8G).

### ChIPseq analysis

All analyses, unless stated otherwise, were performed within R (version 4.3.2) and Bioconductor (version 3.18).[101] ChIP-seq read pairs were aligned to the GRCm38/mm10 mouse genome assembly using the qAlign function from the QuasR package[105] with default parameters. BigWig files with alignment fragment coverage along the genome were generated from the bam files using bedtools version 2.30,[106] by first extracting a bed file with fragment coordinates (bedtools bamtobed), calculating genome coverage in a bedGraph file (bedtools genomecov) and then converting it to BigWig format using bedGraphToBigWig from KentTools version 442.[107] To calculate ChIP enrichments in ATAC peaks, we first counted the number of ChIP fragments overlapping a peak using qCount with shift = “halfinsert” (overlaps are determined using the midpoint of each ChIP fragment). The raw counts r where then normalized to log2-counts per million lcpm using lcpm = log2(r / N * 1e6 + 1), where N is the total number of alignments in a sample. As we observed non-linearities between replicates, we separated lcpm values into IP (lcpm_ip) and input samples (lcpm_input) and separately normalized them using the normalizeCyclicLoess function from the limma package with default parameters,[108] producing lcpm_ip_loess and lcpm_input_loess. IP-enrichments were calculated as the difference lcpm_ip_loess – lcpm_input_loess, which corresponds to log2(IP/input).

### scRNAseq analysis

All analyses were performed in R (v4.2.2) using Bioconductor (v3.16) packages.[101]

#### *Alignment and quantification*

Raw sequencing reads were processed using the Alevin module of Salmon (v1.2.0).[109] Reads were quantified in paired-end mode (-l ISR) using the 10x Genomics Chromium v3 protocol specification (–chromiumV3). Multiple sequencing lanes per sample were combined at the FASTQ level prior to quantification. Quantification was performed against a spliced–unspliced “gentrome” reference derived from GENCODE mouse release M24 (GRCm38), enabling simultaneous estimation of spliced and intronic counts for RNA velocity–compatible analyses. Gene-level quantification was obtained using a transcript-to-gene mapping file (–tgMap), and feature-level output (spliced/unspliced) was generated using the –dumpFeatures option. Cell barcode whitelisting and UMI deduplication were handled internally by Alevin. Quantification uncertainty was estimated using 50 bootstrap replicates (–numCellBootstraps 50). All runs were executed using 32 threads per sample. Quantification outputs were imported into R using tximeta (v1.12.4),[110] with inferential replicates discarded (dropInfReps = TRUE). Spliced and unspliced counts were separated using splitSE, and spliced counts were used as the primary assay for downstream analyses. Cell barcodes were prefixed with sample identifiers, sample metadata were appended, and samples were merged into a single SingleCellExperiment object (v1.16.0) containing 54,446 features across 43,684 cells.

#### *Quality control and normalization*

Gene annotations were added from GENCODE release M24, including gene biotype, gene symbol, Entrez ID and chromosome. Mitochondrial genes were annotated based on chromosome “chrM” and MitoCarta3.0,[111] and ribosomal protein genes were annotated using GO:0003735 with org.Mm.eg.db (v3.14.0). Genes were retained if annotated as protein-coding, immunoglobulin, T cell receptor, mitochondrial rRNA or mitochondrial tRNA genes; all other gene biotypes were removed before downstream analysis. Per-cell and per-feature quality control metrics were calculated using scater (v1.22.0).[112] Cells were retained if they contained >1,200 detected genes and <22% mitochondrial counts. Library-size normalization was performed using scran (v1.22.1).[113] Cells were first grouped into coarse clusters using quickCluster, and deconvolution size factors were estimated with computeSumFactors using min.mean = 0.5. Cells with size factors <0.1 were excluded. Log-normalized expression values were computed with logNormCounts and used for downstream analyses.

Please cite this article in press as: Schwayer et al., Multiscale integration of tissue and chromatin context converts cell heterogeneity into stable intestinal patterning, Cell (2026), https://doi.org/10.1016/j.cell.2026.06.009



### *Sketching and identification of highly variable genes*

To preserve transcriptional heterogeneity and ensure representation of rare cell populations, cells were subsampled using geometric sketching as previously applied in large-scale single-cell analyses.[28] In brief, we used sketchR (v0.1.4), an R interface to the geometric sketching strategy described by Hie et al. (2019).[114] PCA was first computed on log-normalized expression values using 100 components, and representative cells were selected with geosketch using a target sketch size corresponding to approximately 10% of cells, with a minimum of 2,000 cells and capped at the total number of cells. Highly variable genes were identified using modelGeneVar in scran with an FDR threshold of 0.05. Variable genes were identified globally and within each experimental condition, and the union of condition-wise variable genes was used for dimensionality reduction. PCA was computed using 30 components. t-SNE embeddings were generated with snifter/FIt-SNE, and UMAP embeddings were generated using uwot.

### *Cell type annotation*

Cell type identities were assigned using marker gene set scoring, graph-based clustering and manual annotation. Curated intestinal marker gene sets were scored separately within culture conditions using swissknife::normGenesetExpression, with non-variable genes used as the background set. Sketched cells were converted to a Seurat object (v4.1.0), and a shared nearest-neighbor graph was constructed in the sketch PCA space using FindNeighbors with k = 20 and 30 principal components (Hao et al., 2021). Cells were clustered using FindClusters across resolutions 0.4–4.0, and resolution 3.5 was used for annotation. Clusters were annotated based on marker gene expression, marker gene set scores and timepoint distribution. One mixed enterocyte cluster was split by timepoint, with 24–48 hour cells annotated as enterocyte reprogramming cells and 60–108 hour cells annotated as mature enterocytes. Cluster labels from sketched cells were transferred to the full dataset by 1-nearest-neighbor classification in sketch PCA space. Final annotations were collapsed into intestinal epithelial cell states, including reprogramming, regenerative, stem/progenitor, secretory and enterocyte-lineage populations.

## Analysis of Diphteria Toxin experiment

Imaging LGR5-DTR-eGFP organoids before and after diphtheria toxin treatment enabled identification of organoids containing LGR5$^+$ stem cells that underwent ablation, as well as organoids lacking LGR5$^+$ cells at 60 h, which served as negative controls. To quantify internuclear distances following ablation, the dead cell was first identified based on DAPI-positive debris extruded into the lumen. The distances between the centroids of adjacent neighboring cells were then measured, together with YAP1 mean intensity and coefficient of variation.

## Statistical analysis

Statistical analyses were performed using independent biological replicates unless otherwise specified in the figure legends. Data normality was assessed using the Shapiro–Wilk test. Comparisons between two groups were performed using two-sided Mann–Whitney U tests (Wilcoxon rank-sum tests). Comparisons among more than two groups were performed using the Kruskal–Wallis test followed by Dunn's multiple comparisons test, with P values adjusted using the Benjamini–Hochberg method, unless otherwise specified in the figure legends. Sample sizes were not predetermined using statistical methods.